

Dissertation submitted to the Combined Faculties for
the Natural Sciences and for Mathematics of the
Ruperto-Carola University of Heidelberg, Germany
for the degree of Doctor of Natural Sciences

Put forward by
Diplom-Phys Thomas Jan Pander
Born in Krappitz
Oral examination: 13.05.2015

Laboratory ice multiplication experiments in levitated microdroplets

Referees

Prof. Dr. Thomas Leisner

Prof. Dr. Klaus Pfeilsticker

Abstract

Ice in clouds is an important factor for precipitation, the radiative properties and the lifetime of clouds. From the freezing of one cloud droplet, more than one ice particle may result. To investigate these so-called ice multiplication processes, experiments with single levitated droplets freezing at atmospherically relevant temperatures were conducted. Two potential processes were found: the fragmentation of a droplet's ice shell under growing internal pressure and the emergence of bubbles on the ice surface. It has been found that solid particles in and on a freezing droplet promote ice multiplication while solubles inhibit it. A possible link to a highly effective ice multiplication mechanism, the Hallett-Mossop process, is explored. Additionally, high-speed recordings of the potential ice multiplication processes and the freezing of droplets allowed for an analysis of the propagation speed of ice in supercooled water. Furthermore, a technique for droplet size manipulation in pull-push type droplet generators is presented.

Eis spielt im Niederschlag, in den Strahlungseigenschaften und für die Lebenszeit von Wolken eine wichtige Rolle. Gefriert ein Wolkentropfen, kann dies zu mehr als einem Eispartikel führen; dem liegen sogenannte Sekundäreisprozesse zugrunde. Um diese zu untersuchen, wurden Gefrierexperimente an jeweils einzelnen levitierten Wolkentropfen unter atmosphärischen Temperaturen durchgeführt. Zwei potentielle Prozesse wurden beobachtet: einerseits das Zerbrechen der Eisschale um einen noch flüssigen Kern unter dem wachsenden Innendruck, andererseits das Auftreten von Blasen auf der gefrorenen Tropfenoberfläche. Festpartikel im Volumen und auf der Oberfläche eines gefrierenden Tropfens begünstigten Sekundäreisproduktion während lösliche Stoffe diese unterdrückten. Eine mögliche Verbindung zu einem hocheffektiven Sekundäreisprozess, dem Hallett-Mossop-Prozess, wurde untersucht. Durch Hochgeschwindigkeitsaufnahmen der Sekundäreisprozesse und des Gefrierens von Tropfen konnte darüberhinaus die Ausbreitungsgeschwindigkeit von Eis in unterkühltem Wasser gemessen werden. Im weiteren wurde eine Methode zur Tropfengrößenmanipulation bei Injektoren gefunden, welche nach dem 'pull-push'-Prinzip arbeiten.

Contents

Contents	5
1 Introduction	9
1.1 Motivation	9
1.2 Cloud origins	10
1.3 Radiative properties of clouds	11
1.4 Precipitation	12
1.5 Ice formation in clouds	14
1.5.1 Homogeneous nucleation	14
1.5.2 Heterogeneous nucleation	15
1.5.3 Secondary ice processes	16
1.6 This thesis	18
2 Theory	19
2.1 Water	19
2.1.1 Bulk properties of water	19
2.1.2 Water droplet freezing	22
2.1.3 Bubbles at an air-water interface	25
2.2 Aerosols	27
2.2.1 Particle behavior in air	27
2.2.2 Aerosol-substrate interaction	30
2.2.3 Aerosol position on a water surface	32
2.3 Electrodynamic balance	33
2.3.1 Levitation of a single water droplet	33
2.3.2 Compensation of gravity and air drag	33
2.3.3 Compensation of lateral movement	33
2.3.4 Experimental realization	35

3	Experimental setup and methods	37
3.1	Experimental setup	37
3.1.1	Electrodynamic balance and periphery	37
3.1.2	Drop-on-demand injector	39
3.2	Aerosol system	40
3.2.1	Aerosol sources	41
3.2.2	Aerosol size selection	44
3.2.3	Aerosol number	45
3.3	Temperature correction	46
3.4	Methods	48
3.4.1	General experimental procedure	48
3.4.2	Video evaluation	49
4	Results	53
4.1	Droplet size manipulation	53
4.1.1	Single pulse variation	54
4.1.2	Double pulse variation	54
4.1.3	W-shape pulse variation	55
4.1.4	Triple pulse variation	56
4.1.5	Pulse combinations in the EDB	56
4.2	Ice propagation speed in a droplet	56
4.3	Fragmentations	61
4.3.1	PSL suspension experiments	64
4.3.2	Kaolinite suspension experiments	65
4.3.3	Dilution and solution experiments	65
4.3.4	Rainwater experiments	67
4.3.5	SNOMAX suspension experiments	68
4.3.6	Aerosol experiments	69
4.3.7	Quantitative description of fragmentations	70
4.4	Bubbles	72
4.4.1	PSL suspension experiments	73
4.4.2	Kaolinite suspension experiments	74
4.4.3	Rainwater experiments	75
4.4.4	SNOMAX suspension experiments	75
4.4.5	Aerosol experiments	76

5	Discussion	77
5.1	Droplet size manipulation	77
5.1.1	Single pulse variation	77
5.1.2	Double pulse variation	78
5.1.3	W-shape pulse variation	78
5.1.4	Triple pulse variation	78
5.1.5	Pulse combinations in the EDB	79
5.2	Ice propagation speed in a droplet	79
5.2.1	Growth modi	79
5.2.2	Ice propagation speed in supercooled water in the literature	81
5.3	Fragmentations	82
5.3.1	The energy of fragments	82
5.3.2	PSL suspension experiments	83
5.3.3	Kaolinite suspension experiments	84
5.3.4	Dilution and solution experiments	85
5.3.5	SNOMAX suspension experiments	86
5.3.6	Aerosol experiments	87
5.4	Bubbles	88
5.4.1	On the phase of bubble fragments	88
5.4.2	PSL suspension experiments	90
5.4.3	Kaolinite suspension experiments	90
5.4.4	SNOMAX suspension experiments	91
5.4.5	Hematite aerosol experiments	91
5.4.6	Bubbles per bubble event	91
5.5	A possible link to the Hallett-Mossop process	92
5.6	Fragmentations and bubbles in the literature	98
6	Summary	105
7	Appendix	111
7.1	Experimental setup list	111
7.2	Fragmentation frequencies in the literature	113
	Bibliography	117

Chapter 1

Introduction

1.1 Motivation

Climate \ 'klī - mə t \

1. a region with particular weather patterns or conditions
2. the usual weather conditions in a particular place or region
3. the usual or most widespread mood or conditions in a place

Merriam-Webster 2014

Earth's climate is a highly complex system. Climate science encompasses all sciences based on physical processes (as geology, medicine, biology, chemistry and physics itself) and humanities (as sociology, political science, psychology, agricultural science and economics); the arts reflect the definition of climate in their aesthetic grasp of the world. The understanding of climate is one of the great challenges faced by all scientists of today and of tomorrow. Atmospheric research is the cornerstone of the physical description of the aspects most commonly associated with the concept of climate: the occurrence of solar radiation, wind and rain from the sky. Clouds are an integral part of this system as they are the source of rain and the main reason for sun screening. The atmospheric water circulation via clouds is of vigorous dynamic: the atmosphere contains $\approx 13 * 10^{15}$ kg of water (compared to $\approx 13,5 * 10^{21}$ kg in the oceans) which translates into an equivalent layer on the earth surface of 25 mm. The average precipitation rate on earth is ≈ 1000 mm/a, which means that the atmospheric water content is statistically exchanged forty times a year by solar radiation energy and heat energy stored in the earth [118]. Clouds

originate from water condensation in the atmosphere in processes covering several kilometers in the vertical dimension and under geophysical conditions that may span whole countries. This dynamic offers a versatile field of research, from diffusional processes to the scale length of continents, from microseconds to months, from Antarctic cold to the heat of deserts. An adequate description of clouds, of their formation, dwell time in the atmosphere and their precipitation offers at the same time an insight into the fascinating properties of the substance most important for life on earth: water.

The following introduction seeks to contextualize the experiments conducted for this thesis. The formation of clouds is briefly described, followed by the aspects of clouds in which ice plays a role - namely radiative properties and precipitation. The last section deals with the processes involved in the freezing of cloud droplets, which is the subject of this thesis, and leads to the questions that will be attempted to answer in this thesis.

1.2 Cloud origins

Clouds form when moist air is elevated to heights where, due to temperature decrease, water vapor pressure becomes sufficiently high so water condensates into droplets. The pressure $p_{droplet}$ over any droplet is described by the Köhler equation [59]. In the notation of [156], the Köhler equation describes the equilibrium water vapor pressure ratio $S_{droplet} = p_{droplet}/p_w$ ($p_{droplet}$ being the vapor pressure above the droplet surface and p_w the vapor pressure above a plane pure water surface at the same temperature) as

$$S_{droplet} = K * a_w = e^{2M_w\sigma_s/RT\rho_w r} * e^{-\phi\nu n_s/n_w}. \quad (1.1)$$

It consists of the Kelvin term K for the curvature and surface tension effect that increases pressure (see [138]) and a term a_w for soluble materials in the droplet that lowers the vapor pressure on the droplet surface. There are situations (high humidities and soluble gases) that require a “more complex” description [70], but mostly this formula is sufficient for the description of cloud droplet formation. The surface- or Kelvin-term K consists of the molecular weight M_w , the droplet’s surface tension σ_s and the density ρ_w of water, the ideal gas constant R , the temperature T and droplet radius r . The water activity a_w (or Raoult-term [116]) contains the osmotic coefficient ϕ which characterizes a solvent’s deviation from ideal behavior, the number of ions per solute molecule ν_{ion} and the number of moles of the solute n_s and of solvent water n_w . The number of moles of water n_s implicitly leads to the droplet volume, so the Köhler equation may be expanded to an approximation of the form $S_{droplet} \approx 1 + A/r - B/r^3$ with the coefficients

$A = 2M_w\sigma_s/RT\rho_w$ and $B = \phi\nu n_s/n_w$. If $S_{droplet}$ is calculated, it becomes apparent that supersaturations with respect to water of many hundred percent are necessary to sustain droplets consisting of several hundred water molecules, which would result in droplets of a nanometer size, as $A = O(10^{-9}\text{m})$ for tropospheric temperatures. Instead, cloud droplet nucleation takes place on aerosols which are in this case called ‘cloud condensation nuclei’ (CCN). Both components of the Köhler equation can take aerosol properties into account: their size reduces the curvature of a condensing droplet and they may contain soluble materials, but the effect of aerosols is so pronounced that even hydrophobic soot particles may serve as CCN with as little as 2% supersaturation (see [64]). So, under atmospheric conditions, water saturations close to unity are generally sufficient for cloud nucleation as aerosols are ubiquitous (e.g., 31800cm^{-3} on a rainy day [2]). Once cloud droplets are formed, they grow until they have reached an equilibrium with the ambient water vapor pressure; this generally leads to a droplet size of 6-14 μm as measured with satellites by [13]. For droplets in this size range, growth at water vapor pressures close to saturation becomes slow and their terminal falling velocities become important.

1.3 Radiative properties of clouds

Clouds are a central factor in the planetary albedo and thus in the global radiation budget. The cloud formation mechanism under conditions given by the Köhler equation leads to interesting consequences with regards to aerosol-cloud interaction. An increased aerosol concentration, e.g., sandstorms or anthropogenic pollution, will lead to an increase in cloud droplet concentration and a reduction in average cloud droplet size, as the water vapor is distributed to more droplets. The consequence on cloud reflectance is called the “Twomey effect”: “by increasing droplet concentration and thereby the optical thickness of a cloud, pollution acts to increase the reflectance (albedo) of clouds; by increasing the absorption coefficient it acts to decrease the reflectance” [146]. “Although the changes [by the addition of man-made cloud nuclei] are small, the long-term effect on climate can be profound” [145], and altogether “the [...] brightening effect is the dominant one for global climate” [147]. The theory has been verified in, e.g., [1]: “Twomey’s parameterization represents the trend of albedo changes with droplet concentration remarkably well” and was assessed to cause global cooling, albeit with a considerable error margin [10]. It may be tempting to counteract global warming (see [57] for evidence) by exploiting the Twomey effect; there are “legal, political and ethical questions” [32], though, regarding the repercussions of large scale weather manipulation.

For example, pumping several megatons of sulfur dioxide particles into the stratosphere every year to act as CCN, which would be one of the most cost-efficient and feasible measures, would lead to an increased planetary albedo. But it would also turn the atmosphere more opaque, reducing the blueness of the sky, to add an aesthetic dimension and cause for discussion to the consequences for vegetation and stratospheric chemistry. Another factor influencing the radiative properties of a cloud is its phase. Ice has a refractive indices different from water (see [69]), and in contrast to spherical droplets, the multitude of ice shapes “affect their density, terminal fall velocity, growth rate and radiative properties” [68].

1.4 Precipitation

The terminal velocity, at which gravitational acceleration, $F_g = m_{drop}g$, and Stokes drag force on a sphere, $F_D = 6\pi\eta vr$, in air balance out, depends on the droplet radius via $v_{terminal} = 2/9(\rho_w g)/\eta r^2$. With water density ρ_w , gravitational acceleration g , air viscosity η and droplet radius r . This terminal velocity is a few millimeters per second for the usual droplet size of a few microns (see figure 1.1).

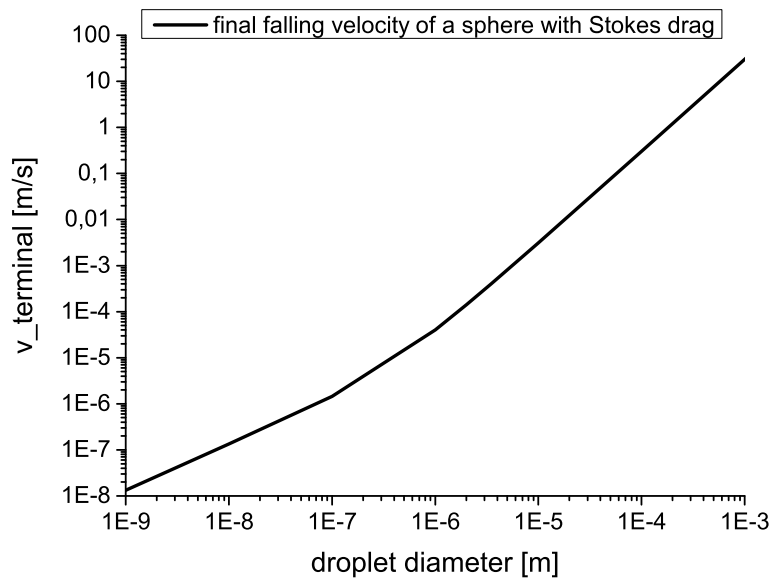


Figure 1.1: Terminal falling velocity of a droplet in air versus droplet radius under normal conditions. Calculated with equation 2.24 in chapter 2.2.1.

As soon as a falling droplet reaches an area of subsaturation with respect to water, evaporation sets in and the terminal velocity is further reduced. It is thus necessary

for droplets to grow to sizes of $\approx 100\mu\text{m}$ to reach the ground as precipitation. In areas of large insolation and sufficient water vapor, the convection may become so strong that turbulence allows for collision-coalescence growth of cloud droplets. Droplets “of a size sufficient to give good collection efficiency” [74] collect smaller ones which results in a much faster growth rate of the larger ones. This is called the warm rain process and is relevant in particular for clouds of a temperature $> 0^\circ\text{C}$. For droplets $> 1\text{mm}$, air resistance causes deformations and the disintegration of droplets into smaller ones, though (see, e.g., [151]).

In clouds where ice particles are present as well as liquid droplets, another process is important. This coexistence is possible due to supercooling, which means that water is at a metastable state below the freezing point and can remain liquid for a considerable time (see chapter 1.5). The works of [6], [33] and [154] describe a fundamental process in clouds. Ice and liquid water have different saturation vapor pressures, as can be seen in figure 1.2 .

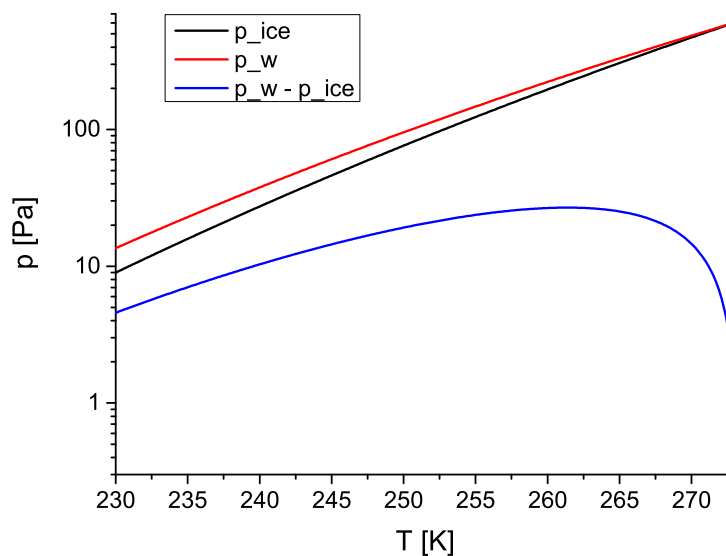


Figure 1.2: Water vapor pressures at saturation over liquid water or ice and their differential. Calculation of pressures from [94], with equations 2.6 and 2.7.

So, when water droplets and ice particles coexist in relative vicinity to each other, there will be a net flow of water vapor towards the ice particles under most conditions. This process occurs under certain limitations; for instance, the overall water vapor pressure might be below ice saturation so that all cloud constituents evaporate. A thorough analysis of this and other cases can be found in [66]. But if vapor pressure is between

the saturation pressure of water and ice for a given temperature, ice particles will grow at the expense of the liquid droplets, gain mass and may reach terminal falling speeds sufficiently high to reach the ground without complete prior evaporation, depending on the temperature and water vapor concentration below the cloud. This is usually referred to as the Bergeron-Findeisen process.

In [122] it was discovered, during experiments which employed solid carbon dioxide (“dry ice”) to introduce ice particles into a freezing unit containing supercooled water droplets, that “whithin less than 10 seconds the supercooled cloud was completely converted to one of ice crystals”. Together with Bergeron-Findeisen process, the ‘seeding’ of supercooled clouds “by dropping pellets of solid carbon dioxide into them” [132] from an aircraft has for a long time been a method to artificially induce precipitation, e.g., for the purpose of removing clouds for the opening ceremony of the Beijing 2008 Olympic games ([19]). Measurements in Israel suggest “little or no effect on total precipitation” [76], though. The Bergeron-Findeisen process does not give an explanation for the presence of ice particles in a dominantly liquid cloud.

1.5 Ice formation in clouds

Ice particle in clouds can be attributed to three origination mechanisms: homogeneous nucleation, heterogeneous nucleation and secondary ice processes.

1.5.1 Homogeneous nucleation

Statistical density fluctuations in water below 0°C lead to the formation of ice-like molecule clusters. Those clusters, also called ‘ice embryos’, may continue to grow if their size is sufficiently large; below a certain size, the heat of fusion of additional water molecules causes disaggregation of such clusters. It is possible to describe the nucleation of a spherical ice embryo in water with an nucleation energy barrier Φ that inhibits ice nucleation at temperatures $<0^\circ\text{C}$ (see [110]) :

$$\Phi = 4\pi r_{IN}^2 \sigma_{I-W} - (4\pi r_{IN}^3)/3n_I(\mu_W - \mu_I) \quad (1.2)$$

with the ice nucleus radius r_{IN} , the surface tension between water and ice σ_{I-W} , the number of water molecules in the nucleus n_I and the difference between the chemical potentials of water and ice $\mu_W - \mu_I$. To create a water-ice surface, energy is necessary, while the conversion of water to ice is energetically favourable. It should be noted that actual ice nuclei may have other shapes than spheres and that the property σ_{I-W} is

not easily measured (see [61]). Assuming knowledge of the actual height of Φ , energy and density fluctuations in supercooled water will lead to the appearance of a volume element in which this barrier is overcome and ice nucleation with subsequent freezing of the bulk volume takes place. The nucleation rate coefficient of a volume element $J_V(T)$ depends on the energy barrier and the temperature. The larger the bulk volume and the longer the observation time, the lower the probability P_u of, e.g., a droplet to remain unfrozen:

$$P_u(t) = P_u(t_0) * e^{(-J_V(T)*V*t)} \quad (1.3)$$

It has been found by [30] that for droplets with a radius $19\mu\text{m} < a < 49\mu\text{m}$, $J_V(-36, 1^\circ\text{C}) = (2, 8 \pm 0, 15) * 10^6 \text{cm}^{-3}\text{s}^{-1}$ which they project to be true for all droplets larger than $1\mu\text{m}$.

1.5.2 Heterogeneous nucleation

Above -36°C , J_V quickly decreases ($J_V(-33^\circ\text{C}) = 15\text{cm}^{-3}\text{s}^{-1}$, $J_V(-34^\circ\text{C}) = 3000\text{cm}^{-3}\text{s}^{-1}$, $J_V(-35^\circ\text{C}) = 2 * 10^5\text{cm}^{-3}\text{s}^{-1}$ in [108]), so homogeneous freezing of water droplets becomes increasingly improbable if small droplet volumes are considered; yet water can consistently be observed to freeze at 0°C . This is due to ice-active surfaces of materials different from ice itself. Several sub-mechanisms of heterogeneous freezing are distinguished:

Deposition freezing: Ice nucleation from the gas phase onto a substrate or particle

Contact freezing: An ice-active surface (trivially ice itself) comes into contact with a supercooled water volume and causes freezing during this contact

Immersion freezing: The ice-active particle or material is immersed into the water volume prior to supercooling

Condensation nucleation: Water condensates onto the substrate or particle which nucleates ice at a certain point; arguably a subset of immersion freezing

These distinctions are not an end in themselves, as it has been found that, e.g., contact nucleation is more effective than immersion nucleation of the same particles at the same temperature (e.g., [24, 77]), and it is claimed that “contact freezing [...] can initiate ice formation at the highest temperatures” [71]; deposition freezing becomes important in the water vapor pressure range between ice saturation and water saturation.

There is a broad spectrum of suitable surfaces and materials found in experiments that ranges from biogenic forest emissions [107], mineral dusts [95], pollen [113], fungal spores [112], ash from volcanic eruptions [133] to steroids [48] or alcohols arranged in

monolayers [36]. From the considerations on cloud formation it is apparent that water-soluble or hygroscopic aerosols are most suitable to serve as CCN, but the freezing point depression of salts and acids [82] does influence their suitability as ice nuclei (IN) negatively.

The most efficient ice nuclei known at the moment and of current interest are of biogenic origin, like bacterial proteins (isolated from bacterial cells by [158]), macromolecules from pollen [5], fungal spores [105] or aerosols from volatile organic carbon emissions [152]. But those biological IN are “of minor importance on the global scale” for precipitation [54] due to their low concentration in the atmosphere.

More ubiquitous, mineral dusts have received a lot of attention in experiments in cloud chambers [88], continuous flow diffusion chambers [120], electrodynamic balances [53], on cold stages [117], in aqueous suspensions [85] or environmental scanning electron microscopy [159]. E.g., feldspar particles have been claimed to “account for a large proportion of the ice nuclei in Earth’s atmosphere” [4]. Chemical aging of aerosols in the atmosphere may enhance their ice nucleation abilities (e.g., black carbon aerosols from the Eyjafjallajökull eruption 2010 [7]), and it has been speculated that precipitation over forests might lead to the release of ice-active aerosols such as fungal spores or pollen [56].

To predict the ice nucleation ability of a surface is one of the challenges of aerosol and cloud physics. “It is believed that silver iodide serves as a very effective nucleus because it very closely resembles ice in crystal structure” [153], but for many efficient ice nuclei such an easy explanation found in the unit cell dimensions of their crystals was not found. So far, “no closed theoretical description of [heterogeneous ice nucleation] and the requirements for good ice nuclei is available”, although “numerous studies have attempted to quantify the ice nucleation ability of different particles empirically in laboratory experiments.” [55].

One of the empirical quantifications in use today is the “ice-active site density” [97] which attributes the ability of ice nucleation at a given temperature to nucleating sites that have a certain probability to exist on a surface element of, for instance, an aerosol.

1.5.3 Secondary ice processes

Ice particle numbers in clouds are sometimes found to exceed ice nuclei numbers [11, 52], reportedly by a factor of up to 10^4 [93]. While particle shattering at inlets of measuring instruments mounted on research planes has been found to be a source of ice particle number overestimation [67, 150], so-called secondary ice processes “may play a role in ice formation” [106] where homogeneous and heterogeneous nucleation of ice can’t explain

the ice particle number .

‘Secondary ice’, ‘ice enhancement’ or ‘ice multiplication’ processes denote mechanisms in which pre-existing ice (from homogeneous or heterogeneous freezing) creates more ice by ice-ice or ice-water interaction. For instance, “a collision between two whiskered ice crystals or between a whiskered crystal and a water drop could fracture many of these fragile whiskers, with the consequent production of new ice nuclei.” [98], but “the generation of secondary particles by mechanical fracturing does not explain the presence of large concentrations of ice crystals in relatively warm clouds” [148].

An ice enhancement process which does not rely on many pre-existing ice particles is the fragmentation of freezing water drops. Once ice nucleation has taken place by heterogeneous nucleation, an ice shell grows around a liquid core, applies pressure to the core due to the expansion of water at the phase transition. Stresses in the shell rise and the shell may rupture once its yielding stress is exceeded. Extensive experiments have been conducted by [14, 86, 134], in which a moderate ice enhancement was observed.

The ice multiplication mechanism widely regarded to be the most effective [9, 44, 47, 50, 115] is called the ‘Hallett-Mossop’ (H-M) process which Hallett and Mossop themselves identified as “riming-splintering”, in which “ice particles growing by sweeping up supercooled drops might throw off secondary ‘splinters’ of ice” [43]. “This occurs between temperatures of -3 and -8°C , the production rate being greatest at -5°C . [...] On average, one ice splinter is thrown off for every 250 drops of diameter $>25\mu\text{m}$ accreted, at cloud temperature -5°C .” [90]. In [90], four possible explanations for the splinter production are given:

- “The formation of an ice shell round the periphery of an accreted drop. Build-up of pressure when the drop finally freezes causes the shell to burst and splinters are thrown off”. This explanation is seconded in [18], where electron scanning microscopy of gold-coated formvar replicas of accreted and frozen droplets showed “the heat loss from freezing drop was sufficiently symmetrical to permit the formation of an ice shell”.
- “Freezing of drops that make glancing contact with rime” too short to become accreted on the ice particle, but long enough for ice nucleation to take place.
- “Growth and subsequent detachment of frail ice needles” [from the vapor phase].
- “Detachment of ice by evaporation [...] of ice structures that are attached only by narrow bridges to the main rime”.

It was claimed that “thermal gradients give stresses leading to an ice crack at about -5°C .”[27]; on the other hand “the mechanism for the process is still uncertain.” [15]. Moreover, “it is very probable that key secondary ice production processes have not been identified outside of [the H-M processes] temperature range” (ibidem).

1.6 This thesis

While droplet fragmentation during freezing has been identified as an ice multiplication process for several decades, this thesis endeavors to deliver an enriching description of the process over the range of atmospherically relevant conditions. Due to the potentially significant effect at temperatures where the Hallett-Mossop effect is not efficient, the fragmentation process may be a factor in the number of ice particles in supercooled clouds.

At the division “Atmospheric Aerosol Research” of the Institute for Meteorology and Climate Research (IMK-AAF), Karlsruhe Institute for Technology (KIT), several thousand experiments were conducted for this thesis to add another tile to the mosaic of ice nucleation in clouds and climate science by answering the following questions:

- Under which conditions do fragmentations occur?
- Are there other ice multiplication processes in freezing droplets that have not been considered yet?
- Is there a link between the Hallett-Mossop process and droplet fragmentation?

This thesis will continue with the theory (chapter 2) of the properties and the behavior of water in bulk, droplets and bubbles (chapter 2.1), the behavior of aerosols (chapter 2.2) and of the experimental setup (chapter 2.3).

The theoretical considerations are followed by the description of the physical experimental setup in chapter 3 and the methods employed for this thesis in chapter 3.4.

The measurement results are presented in chapter 4. Observations on water droplet creation with a droplet generator (chapter 4.1) are followed by the results of experiments on the propagation speed of ice in supercooled water (chapter 4.2) and on ice multiplication experiments (chapters 4.3 and 4.4).

These results are discussed in chapter 5, and the thesis is summarized and given an outlook in chapter 6.

This work would not have been possible without water, so it will begin the theory chapter with a description of dihydrogenoxygen monoxide.

Chapter 2

Theory

This chapter consists of three sections: the properties of water, the behavior of aerosols and the storage of charged particles.

The water section comprises a list of the bulk properties of water, the description of freezing water droplets and an introduction to the processes occurring when a bubble bursts at an air-water boundary.

The aerosol section deals with the behavior of small particles in liquid flows and electric fields and can be applied to water droplets in air as well as to mineral dust in water. This section also deals with solid particles at an air-water boundary.

In the final section, the shape of the core element of the experiments presented in this thesis, the electrodynamic balance, is deduced from electrodynamic principles.

2.1 Water

2.1.1 Bulk properties of water

As demonstrated in the introduction, water gives rise to an abundance of effects in the atmosphere which are the subject of continuing research; it thus seems justified to take a closer look at one of the most important molecules for the life of atmospheric scientists and all other life on earth.

Water is a molecule with peculiar properties.

It consists of two hydrogen atoms that share covalent bonds with an oxygen atom. Due to the strong repulsion of the two electron pairs in the oxygen that do not contribute to the covalent bonds, the angle between the hydrogen bonds is 109° [75], and the oxygen atom has a higher electron density than the hydrogen atoms. This electronic configuration results in a permanent dipole moment in water that heavily influences its

radiative properties and is, e.g., exploited in microwave heating [34]. Its boiling point at 1 atmosphere pressure is 100°C, which is quite high compared to other molecules of similar molar mass like CH_4 (boiling point of -162°C) or similar constituents like H_2S (boiling point of -60,2°C). This phenomenon can be attributed to the relatively strong hydrogen bonds between individual water molecules in the liquid phase. A hydrogen bond is not a bond as in covalent or ionic bonds, where electrons are shared between atoms, but denotes a strong dipole-dipole attraction. It is stronger than a van der Waals interaction, which is based on induced dipoles, but weaker than an actual bond in a molecule. The effect of such hydrogen bonds may also be found, for instance, in hydrogen fluoride HF or ammonia NH_3 (boiling point at 20°C or -33,3°C, respectively, taken from [79]) where hydrogen bonds are established intermittently - intermittently means in the order of 10^{-12} s in the case of water. Without these hydrogen bonds, water would only exist as a gas under earth conditions. With these bonds, water has the second highest specific heat capacity per mass ($c_p=4,2$ J/(g*K) at standard conditions) of all heteroatomic molecules and a high heat of vaporization ($L_v=2257$ kJ/kg) and melting heat ($L_m=333,5$ kJ/kg).

Water is an extraordinary material if its density behaviour is considered. While most materials' densities show a monotonically increasing behavior with temperature, water reaches its maximal density at +4°C in its liquid state (see, e.g., in [79]). This is not easily justified and may be attributed to a "competition between the presence of open second-neighbor oxygen-oxygen structure at 4.5 Angstrom and a dense second-neighbor structure obtained from the bending of hydrogen bonds" [17]. Throughout this thesis, various properties of water will be utilized for calculations. As many of these properties can to date not be derived from theoretical considerations in accordance with measured values, empirical expressions are employed. These properties are:

Heat capacity of water

$$c_{p,w} = 74,3 + 0,044 * (T/222K - 1)^{-2,5} J/(K \text{ mol}), \quad (2.1)$$

as measured between -28,3°C and +10°C in [139].

Heat capacity of ice

$$c_{p,i} = -2,0572 + 0,14644 * T/K + 0,06163 * T * e^{-(T/125,1)^2} J/(K \text{ mol}) \quad (2.2)$$

as fitted to data of [39] in [94].

Heat conductivity of ice

$$k_{ice} = 5,20 - 11,2 * 10^{-3} * T/K \frac{W}{m K} \quad (2.3)$$

as fitted to data of [130] between 250K and 273,2K at atmospheric pressure $\pm 10\%$.

Diffusivity of water vapor in air

$$D_v = 0,211 * (T/273,15K)^{1,94} * 10^{-4} m/s^2 \quad (2.4)$$

as given in [110].

Vapor pressure over water

$$\begin{aligned} \ln(p_w/Pa) = & 54,842763 - \frac{6763,22K}{T} - 4,210 \ln(T/K) + 3,67 * 10^{-4} T/K \\ & + \tanh(0,0415(T/K - 218,8)) * \end{aligned} \quad (2.5)$$

$$(53,878 - \frac{1331,22K}{T} - 9,44523 \ln(T/K) + 0,014025 T/K) \quad (2.6)$$

for $123K < T < 332K$ as given in [94].

Vapor pressure over ice I_h (commonly found in nature)

$$p_{ice} = e^{28,9074 - 6143,7K/T} Pa \quad (2.7)$$

as given in [94].

Surface tension of water

$$\sigma_w = 235,8 * 10^{-3} \left(\frac{647,15K - T}{647,15K} \right)^{1,256} * \left(1 - 0,625 * \frac{647,15K - T}{647,15K} \right) N/m \quad (2.8)$$

as given in [149].

Density of supercooled water

$$\begin{aligned} \rho_w = & 0,99986 + 6,690 * 10^{-5} * T_* - 8,486 + 10^{-6} * T_*^2 \\ & + 1,518 * 10^{-7} * T_*^3 - 6,9484 * 10^{-9} * T_*^4 \\ & - 3,6449 * 10^{-10} T_*^5 - 7,497 * 10^{-12} * T_*^6 g/cm^3 \end{aligned} \quad (2.9)$$

with $T_* = T - 273,15K$ as given in [46].

Latent heat of fusion

$$L_m = 333500 \text{ J/kg} \quad (2.10)$$

Melting point of water

$$T_m = 273,16 - 7,38 * 10^{-8} * p/\text{Pa} - 1,55 * 10^{-16}(p/\text{Pa})^2 \quad (2.11)$$

with $T_* = T - 273,15\text{K}$. Second grade polynomial fit to the data of [49].

Viscosity of water

$$\eta_w(p) = 2,4055 * 10^{-5} \exp(p * 4,42 * 10^{-4} \text{bar}^{-1} + \frac{4753 \frac{\text{J}}{\text{mol}} - p * 9,565 * 10^{-1} \frac{\text{J}}{\text{mol bar}}}{8,314 \frac{\text{J}}{\text{mol K}} (T - 139,7\text{K} - p * 1,24 * 10^{-2} \frac{\text{K}}{\text{bar}})}) \quad (2.12)$$

as given in [81].

For all equations, $[p] = \text{Pa}$ and $[T] = \text{K}$ if not stated otherwise.

2.1.2 Water droplet freezing

The process of droplet nucleation in the atmosphere is described in chapter 1.2. The following considerations deal with the behavior of a droplet in which ice nucleation has taken place.

2.1.2.1 First freezing step

Contact-free captured pure water droplets (see chapter 2.3) in the size range of 40-100 μm can be supercooled to -36°C [30] before the metastable water phase breaks down after seconds due to statistical density fluctuations. Once this or ice nucleation by another source takes place (see chapter 1.5), ice propagates from this point. It “is supposed that only a fraction α of the total sites in the crystal surface are available for molecular attachment at a given undercooling” [51] which results in different ice shapes: a morphology diagram is presented in [125], and [126] found that there is a “temperature dependence of the fractal dimension d_f of the ice-crystal contour” in ice propagation experiments in supercooled water.

The propagation speed of ice in water is dependent on the temperature: the colder the water, the faster the foremost tip of a dendrite grows. An overview of literature propagation speeds of ice in supercooled water v_{ice} , generally of the form $v_{ice} = a\Delta T^b$

with coefficients a and b for supercoolings ΔT , is given in table 5.1. [72] presented a theory of dendritic ice crystal growth based on diffusion of water molecules onto the ice surface with the assumptions that the crystal is a paraboloid of revolution and surface kinetics is infinitely fast. They proposed “that the maximum-velocity principle conventionally used in theories of dendritic crystal growth be replaced by a stability criterion of the form $v_{ice}\rho^2 = constant$, where v_{ice} is the growth velocity and ρ is the tip radius.” A comparison between theoretical and experimental ice propagation speeds showed a good agreement for supercoolings lower than $\approx 8^\circ\text{C}$ and an overestimation for deeper temperatures for this supposedly “universal law of dendritic growth velocities” [73]. The measurements of [124] showed the same result; according to [127] the deviation in the “rate of molecular rearrangement at the interface from liquid state to solid state” is “caused by effect of surface kinetics”: the movement speed of water molecules is reduced at colder temperatures, solidification is slowed. The measurements by [87] suggest that the point at which ice growth becomes even slower with deeper temperatures is at -37°C . Depending on the observed volume, this first freezing step may be very fast; the time for the first freezing step in a droplet of diameter $2a$ may be estimated with

$$t_1 = 2a/v_{ice}, \quad (2.13)$$

with v_{ice} being up to $\approx 0,5\text{m/s}$ at -35°C (as measured in this thesis). Due to the release of latent heat, only a fraction

$$f_{ice} = \int_T^{T_m} c_{p,w}(T')/L_m dT' \approx (T_m - T)/80\text{K} \quad (2.14)$$

of a volume of supercooled water at the temperature T is turned into ice during this growth, with the melting temperature of ice $T_m = 273,15\text{K}$, the specific heat of water $c_{p,w}$ and the latent heat of fusion L_m . For the remaining water volume $V_{liq} = V_{drop} * (1 - f_{ice})$ to freeze, heat exchange with the environment has to take place.

2.1.2.2 Second freezing step

It is assumed that the subsequent heat exchange occurs via an ice-air interface which will be true after a short time after the first freezing step is finished. For the calculations, described in more detail in [110], the droplet temperature is set at 0°C ; temperature equilibrium in the droplet can be assumed because of the fast conduction of heat in water compared to air ($k_{water}/k_{air} = O(1000)$). The heat $Q_{con,ice}$ conducted through the ice shell is assumed to be equal to the heat of fusion Q_{ice} of water turned into ice in the

droplet:

$$Q_{con,ice} = 4\pi k_{ice}(T_m - T_a) \frac{ar}{a-r} = 4\pi \rho_w L_m (1 - f_{ice}) r^2 \frac{dr}{dt} = Q_{ice}, \quad (2.15)$$

with the heat conductivity of ice k_{ice} , the droplet surface temperature T_a and the radial position of the ice-water boundary r . The heat flow through the ice shell is in turn assumed to be equal to the heat loss $Q_{con,air}$ to the environment by sublimation and heat conduction:

$$Q_{con,ice} = 4\pi k_{ice}(T_m - T_a) \frac{ar}{a-r} = 4\pi a k_{air}(T_a - T_\infty) + 4\pi a L_s D_v (\rho_{v,a} - \rho_{v,\infty}) = Q_{con,air}. \quad (2.16)$$

The vapor density difference $\rho_{v,a} - \rho_{v,\infty}$ of water in air at the droplet surface and in a far-away distance ∞ can be approximated by the averaged vapor density temperature gradient at ice saturation:

$$L_s D_v (\rho_{v,a} - \rho_{v,\infty}) \rightarrow L_s D_v (T_a - T_\infty) \left(\frac{d\rho_v}{dT} \right)_{sat,i}. \quad (2.17)$$

Assuming such an environment, it follows that

$$k_{ice}(T_m - T_a) \frac{ar}{a-r} = (T_a - T_\infty) (k_{air} + L_s D_v \left(\frac{d\rho_v}{dT} \right)_{sat,i}). \quad (2.18)$$

Now T_a can be removed from the equations, and it follows

$$\begin{aligned} & \frac{\rho_w L_m (1 - f_{ice})}{T_m - T_\infty} (k_{air} + L_s D_v \left(\frac{d\rho_v}{dT} \right)_{sat,i}) \frac{r^2}{a} \frac{dr}{dt} \\ = & \left(1 - \frac{k_{air} + L_s D_v \left(\frac{d\rho_v}{dT} \right)_{sat,i}}{k_{ice}} + \frac{k_{air} + L_s D_v \left(\frac{d\rho_v}{dT} \right)_{sat,i}}{k_{ice}} \frac{a}{r} \right)^{-1}, \end{aligned} \quad (2.19)$$

with the rescalings $y = r/a$, $m = \frac{k_{air} + L_s D_v \left(\frac{d\rho_v}{dT} \right)_{sat,i}}{k_{ice}}$ and $t_2 = \frac{\rho_w L_m (1 - f_{ice}) a^2}{3(T_m - T_\infty)(k_{air} + L_s D_v \left(\frac{d\rho_v}{dT} \right)_{sat,i})}$ the equation becomes

$$3t_0 \frac{dy}{dt} = - \frac{1}{(1-m)y^2 + my}. \quad (2.20)$$

Integration to the total freezing time $t_2 \Leftrightarrow y = 1$ gives

$$t_2 = t_0(1 + m/2) \approx t_0, \quad (2.21)$$

as m is relatively small (see figure 2.1). So, the total freezing time ($t_2 \gg t_1$) is mainly dependent on the supercooling $\Delta T^{-1} = (T_m - T_\infty)^{-1}$ and the droplet surface a^2 .

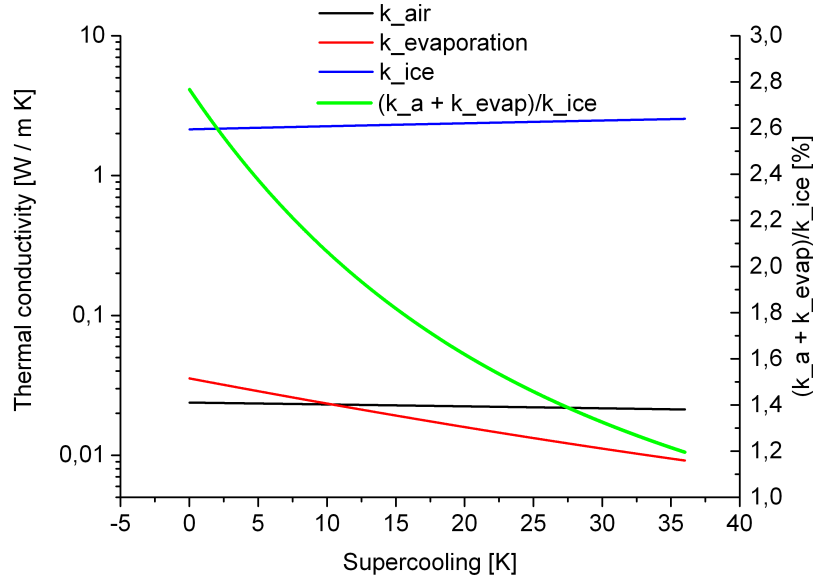


Figure 2.1: Thermal conductivities of ice (equation 2.3), air ($k_{\text{air}} = (23,08 - 0,071\Delta T) * 10^{-3} \frac{W}{mK}$), and by evaporative cooling (equation 2.18) and m (equation 2.20).

During this second freezing step, while the ice shell grows in thickness, the pressure in the core grows exponentially [60] due to the lower density of ice. Weak points in the ice structure of the shell, like grain boundaries, brine pockets or other small lattice defects, may gradually yield under the tensile stresses. This leads to deformations in freezing droplets; in [103], it has been shown that this effect also takes place in highly pure water droplets. There, the aspect ratio changed from unity to 1,1-2, with an average new aspect ratio over all temperatures of $1,12 \pm 0,04$. As discussed in chapter 2.2.1, this will lead to a slower falling speed of the droplets with consequences for the probability of collision with other ice particles or liquid droplets.

2.1.3 Bubbles at an air-water interface

Bursting bubbles at liquid-gas interfaces may generate many small droplets and consequently aerosols. Investigations into the cause and effect of bursting bubble particle generation are based on health issues with hospital pools [3], the aromatic sensation of champagne fizz [80] or the aerosol production of sea-salt particles in marine surf [99].

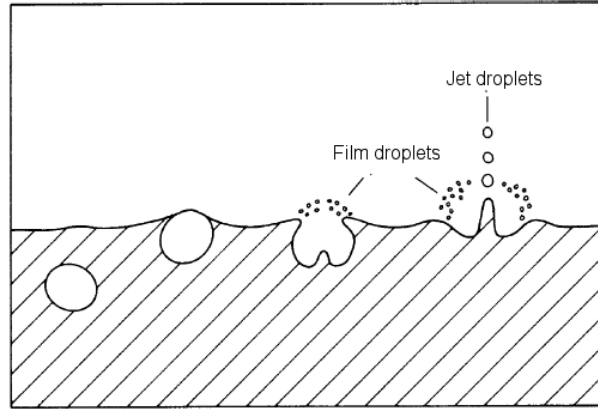


Figure 2.2: Jet droplet and film droplet generation, schematically illustrated. Slightly modified from [118].

Droplets are generated by two principal mechanisms: jet ejection and film retraction that are described in the following paragraphs and depicted in figure 2.2.

2.1.3.1 Droplet generation by jet ejection

A bubble at the liquid-gas boundary can be described as a gas-filled cavity; once the film on top of the bubble breaks down, pressure equalization of the gases occurs at the speed of sound. The film is retracted to the bulk by surface tension, and the cavity collapses due to buoyancy and surface tension. The inertia of the retracting water creates a narrow vertical jet in the middle of the cavity “which eventually breaks down into one or several droplets”; in the case of bubble radii R and “for $R_v < R < R_c$ the phenomenon is dominated by surface tension and inertia” [29] while gravity is negligible, with the viscous-capillary length $R_v = \rho_w \nu^2 / \sigma_w = 0,014 \mu\text{m}$, ν being the kinematic viscosity, and the capillary length $R_c = \sigma_w / \rho_w g = 2,7 \text{mm}$ for standard conditions. [29] calculate the jet droplet speed and size for bubble radii between $4 \mu\text{m}$ and 2cm . Their results place the jet droplet size between 2% - 13% of the bubble size and give their best fit to their speed calculations as $v_{drop} = 0,38 * \sigma / (\eta \sqrt{R * \sigma / \rho \nu^2}) = 0,38 * \sqrt{R \sigma^3 \rho} / \eta^2$ with slower droplets for droplets from bubbles of $4 \mu\text{m}$ radius or less. These results are comparable with experimental findings [38].

Droplet creation via the jet ejection mechanism, e.g., at the tip of a capillary might be feasible for supplying experiments with small droplets like in some ink jet printers [25]. However, for the experiments in this thesis, another technical solution was used.

2.1.3.2 Droplet generation by film retraction

Once a hole, reportedly of a “diameter [...] typically larger than the film thickness” h [151] has nucleated in a bubble film of density ρ by density fluctuations in the film, the film edges retract towards the bulk under the surface tension σ with the Taylor-Culick retraction speed $v_{T-C} = \sqrt{2\sigma/\rho h}$ [137]. This rim’s mass increases while it expands, resulting in a toroid shape, and its thickness varies sinusoidally along the rimline due to a Rayleigh-Plateau instability which is, e.g., responsible for the break-up of water falls. Due to their inertia, the retraction speed of those thicker stretches of the film is lower, or “surface tension is insufficient to keep bits of the rapidly advancing toroid from tearing loose” [131]: liquid ‘fingers’ form from the rim and pinch off at certain length, which is again caused by a Rayleigh-Plateau instability. These ligaments then get aerosolized with a velocity tangential to the bubble curvature. Additionally, for large bubbles (in which the rim of the hole propagates over a distance $> (\rho/\rho_a)h$), it has been observed that the film close to the rim may, “just like a flag edge flaps in the wind [be] successively accelerated on both sides perpendicularly to its plane, inducing film thickness modulations and centrifuging liquid ligaments that finally pinch off to form the observed spray”, which is based on a Kelvin-Helmholtz instability [151].

The mean drop size of film droplets from bubbles of radius R has been found to be proportional to $R^{3/8}h^{5/8}$ [78].

Another possible case has been shown by experiments and simulations by [8]. In bubbles of η with Reynolds numbers $Re = \rho v_{T-C}R/\eta > 1$, air may get entrapped between the torus and the bubble film at the base and may form secondary bubbles from which new jet droplets and film droplets can result.

2.2 Aerosols

2.2.1 Particle behavior in air

An aerosol denotes a solid or liquid particle that is located in air (*latin: aer – air, solutio – solution*). While this may mean any cohesive matter apart from the solvent gas, including large molecules like volatile organic compounds (VOCs) that may originate from plants to passenger airplanes, it generally refers to particles in the range of several nanometers to fractions of millimeters. This is rooted in the dwelling time of particles in a volume of air before deposition, i.e. the removal of the particle to a surface takes place. For small particles ($< 100\text{nm}$), especially so-called secondary aerosols that nucleate from single molecules and grow by agglomeration with other molecules (e.g., sulphur dioxide

with water), diffusion is the limiting process. For larger particles ($> 1\mu\text{m}$), generally so-called primary aerosols which existed before becoming airborne (e.g., by updrafts in dust storms or volcanic eruptions), gravitational pull to the earth's surface is the limiting process. While earth's gravitation exerts a force on all particles, their falling speed is limited by air resistance which may be calculated via the Stokes drag force which describes the force on a moving sphere in a viscous medium:

$$F_d = -3\pi\eta_{air}vd\xi/C_C \quad (2.22)$$

with η_{air} being the air viscosity, v being the spherical particle's velocity relative to the air and d its diameter. ξ is a correction factor for non-spherical particles in which case d denotes the characteristic length of the particle; while there exist aerodynamic particle shapes that reduce air resistance in comparison to a sphere, generally $\xi > 1$. ξ can be a function of time, as the tumbling motion of a falling sheet of paper or a falling plate of styrofoam show. C_C denotes the Cunningham slip correction [20], which accounts for the fact that Stokes drag assumes a no-slip condition ($v = 0$) at the particle surface. For Knudsen numbers $Kn = \lambda/d > 0,02$, with λ being the free path length of air molecules, this assumption no longer holds true. The correction factor is

$$C_C = 1 + 2\lambda/d * (A_1 + A_2 * \exp(-A_3d/\lambda)) \quad (2.23)$$

with $\lambda = 67\text{nm}$ under normal conditions and $A_1 = 1,257$, $A_2 = 0,400$ and $A_3 = 1,10$ [21]. C_C exceeds 1,05 for particles smaller than $\approx 3,5\mu\text{m}$. In the case of small Reynolds numbers $Re = vL/\nu < 1$, with L being the characteristic length of the system (here: the particle diameter), v the flow speed of the liquid and ν being its kinematic viscosity, the flow can be assumed to be laminar, which means that turbulent resistance can be neglected; with a kinematic viscosity of air $\nu = 1,48 \times 10^{-5}\text{m}^2/\text{s}$ at 1 atm and 25°C and a flow speed of $0,1\text{m/s}$, this is true for particles $< 150\mu\text{m}$. As $F_d \sim -v$, there is a critical sedimentation velocity v_{sed} at which the gravitational force $F_g = mg = \pi/6d^3 * \rho_p g$ of a spherical particle of density ρ_p and its Stokes drag force cancel out. This velocity is calculated by equalizing the gravitational force and the Stokes drag and solving for the speed:

$$v_{sed} = mgC_C/(3\pi\eta\xi d) = \rho_p g C_C d^2 / 18\eta \quad (2.24)$$

It is to be noted that $\eta = \eta(p, T)$ and $C_C(Kn) = C_c(Kn(p, T))$, which becomes relevant for atmospheric altitudes h higher than $\approx 5\text{ km}$ as the air pressure scales with $p = p_0 \exp(-h/h_0)$, with the pressure at sea level p_0 and the scale height $h_0 = 7,31\text{km}$ for

dry air at an average atmospheric temperature of 250K. This critical speed, also called sedimentation or final velocity, is less than 0,3 m/s for water particles smaller than 100 μ m under normal conditions. Considering Newton's second law which is equalized by the drag force, and solving the resulting differential equation, we arrive at

$$F_d = m dv/dt \sim -v \implies v(t) = v_0 \exp(-t * C_C m / 3\pi\eta\xi d). \quad (2.25)$$

This means that due to particle inertia, a particle in an air flow does not follow a change in the flow instantaneously, but with a characteristic reaction time

$$\tau_{Stokes} = C_C m / (3\pi\eta\xi d) \quad (2.26)$$

before the particle velocity component that has no longer been parallel to the flow becomes neglectable. This can be exploited to filter heavy particles from an air flow in an impactor, which basically consists of a sharp bend in an air duct. Most air filters for large particles work with this effect as well. τ is, for a 10 μ m water droplet, 0,3ms. For the further considerations, the particle property of mobility is useful. The mobility $B = v/F$ is defined as the ratio of the maximal velocity a particle can obtain under a force F. The aerodynamic mobility is calculated by rearranging equation 2.22:

$$B_{Stokes} = v / (3\pi\eta v d \xi / C_C) = C_C / (3\pi\eta d \xi) = \tau_{Stokes} / m \quad (2.27)$$

This mobility can then be used for calculating the terminal velocities of a particle under the influence of an arbitrary force and air drag, for instance for an aerosol with the number of n elementary charges e in a homogeneous electric field E , in which case the force on the droplet is $F_{el} = neE$. Inserted into equation 2.27, we get:

$$v_{el} = B_{Stokes} * neE. \quad (2.28)$$

For applications in electric fields, it is useful to define the electric mobility B_{el} :

$$B_{el} = v_{el} / E = ne * B_{Stokes}. \quad (2.29)$$

Also, it has also been found useful to introduce equivalent diameters for the actual particle size $d * \xi$ which may be difficult to ascertain, especially in the case of aerosols < 1 μ m where observation based on non-ionizing light reaches a resolution limit. One of those diameters is the Stokes size d_{Stokes} , which is the diameter of a sphere of particle density with the same v_{sed} . Another diameter sometimes used is the aerodynamic diameter d_{aero} ,

which describes a sphere with a density $\rho_w = 10^3 \text{kg/m}^3$ with the same v_{sed} . By inserting these diameters into equation 2.24, we get

$$v_{sed} = \frac{mgC_C(d)}{3\pi\eta\xi d} = \frac{\rho_p g C_C(d_{Stokes})d_{Stokes}^2}{18\eta} = \frac{\rho_w g C_C(d_{aero})d_{aero}^2}{18\eta} \quad (2.30)$$

or the identities

$$\frac{mC_C(d)}{\pi\xi d} = \frac{\rho_p C_C(d_{Stokes})d_{Stokes}^2}{6} = \frac{\rho_w C_C(d_{aero})d_{aero}^2}{6}. \quad (2.31)$$

2.2.2 Aerosol-substrate interaction

Apart from inertia or diffusion, an aerosol may also be attracted to another particle or a substrate via electric or phoretic forces. For charged particles, *Coulomb attraction* plays a role with the force $F_C = q_p q_s / 4\pi\epsilon_0 \epsilon r_{ds}^2$, with the particle charge q_p and substrate charge q_s , the particle-substrate distance r_{ds} and the vacuum and medium's permittivity ϵ_0 and ϵ .

If a charged substrate is present, a dipole may be induced in the aerosol, causing an attractive *dipole force*. The force depends on the polarizability ϵ_p of the particle, which is a measure of charge mobility on the particle surface, and its size d_p . The charge on the substrate first induces the dipole in the particle which is then attracted to the substrate, which leads to a higher distance dependency than the usual Coulomb attraction. The dipole force is given by

$$F_{Dip} = \frac{(\epsilon_p - 1)}{(\epsilon_p + 2)} \frac{d_p^2 q_s^2}{16\pi\epsilon_0 r_{ds}^5}.$$

Thermophoresis describes the motion of particles caused by a non-uniform heating. A temperature gradient in the air around the particle causes a net impulse delivery from molecule collisions to its 'warm' side, so the particle is driven in the direction of the heat flow. The *thermophoretic force* on a particle is, according to [12],

$$F_{th} = -\frac{12\pi\eta r(k_a + c_t k_p Kn)k_a \Delta T}{5p(1 + 3c_m Kn)(k_p + 2k_a + 2c_t k_p Kn)},$$

with the gas pressure p and spacial temperature gradient ΔT , thermal conductivity of air and particle k_a and k_p and the empirical 'isothermal slip' coefficient $c_m = 1,0$ and the 'temperature jump' coefficient $c_t = 2,5$. In analogy to gravitational or electric forces, the thermophoretic velocity v_{th} of a particle may be calculated with a via $v_{th} =$

$-((B_{th}k_a\Delta T)/p)$ with the mobility

$$B_{th} = \frac{0,4C_C(k_a + 2,5k_pKn)}{(1 + 3Kn)(k_p + 2k_a + 5k_pKn)}.$$

Finally, in a droplet-aerosol system, water vapor flow (or 'Stephan flow') from or to the droplet may cause drag in particles, the so-called diffusiophoretic force; according to [110], the *diffusional drag force* F_{Df} on a particle in the proximity of a droplet due to water vapor flow is

$$F_{Df} = -7,15\pi\eta r D_v \Delta\rho_v / C_C \rho_a$$

with the diffusivity of water vapor D_v , the water vapor density ρ_v and the air density ρ_a . The diffusional drag force is basically a modified Stokes drag force, in which the speed of the flow is dictated by the diffusional flow from the droplet.

Considering all these forces together with the Stokes drag, for a charged droplet in an aerosol flow, the trajectory x of a particle may be calculated via

$$\begin{aligned} m\ddot{x} = & \frac{q_p q_s}{4\pi\epsilon_0\epsilon r_{ds}^2} + \frac{(\epsilon_p - 1)}{(\epsilon_p + 2)} \frac{d_p^2 q_s^2}{16\pi\epsilon_0 r_{ds}^5} - \frac{12\pi\eta r (k_a + c_t k_p Kn) k_a \Delta T}{5p(1 + 3c_m Kn)(k_p + 2k_a + 2c_t k_p Kn)} \\ & + \frac{0,4C_C(k_a + 2,5k_pKn)}{(1 + 3Kn)(k_p + 2k_a + 5k_pKn)} - \frac{7,15\pi\eta r D_v \Delta\rho_v}{C_C \rho_a} - \frac{3\pi\eta v d \xi}{C_C} |\vec{v} - \dot{\vec{x}}| \end{aligned} \quad (2.32)$$

with the velocity vector \vec{v} in the direction of the air flow and the velocity vector $\dot{\vec{x}}$ in the direction of the particle movement. With this differential equation for the motion of a particle, the collection efficiency of a droplet of radius r_d in an aerosol stream may be calculated. Under the conditions of the experiments in this thesis, the phoretic forces are negligible.

The collection efficiency is defined as $\zeta = \pi r_c^2 / \pi (r_d + r_p)^2$ with the collection radius r_c . πr_c^2 denotes the cross section of the air flow in which particles of radius r_p are collected by the droplet; attractive forces between particle and droplet enlarge this cross section. For uncharged droplets and small particles, the efficiency may well be $\ll 1$. Once the collection efficiency is calculated and the particle density in the flow Γ_p and the air volume flow J_a are measured, the expected collection rate n_c of particles hitting the droplet per time can be calculated. The collection rate is given by the number of particles passing through the effective cross section via the product of droplet cross section, collection efficiency, particle density in the flow and air volume flow:

$$n_c = \pi r_d^2 \zeta J_a \Gamma_p. \quad (2.33)$$

n_c is subjected to statistical fluctuations in Γ_p , so the number of particles on a droplet is only $n_c * t$ for large t .

2.2.3 Aerosol position on a water surface

Once an aerosol particle has hit a droplet, its position may be of interest – namely if it stays on the surface or gets immersed into the droplet’s bulk volume. In general, the position of a solid particle relative to an unperturbed water surface is governed by the Young equation for the surface tensions which defines the contact angle $0 \leq \theta_c \leq \pi$:

$$\sigma_{pw} = \sigma_{pa} - \sigma_{wa} * \cos(\theta_c) \quad (2.34)$$

with the surface tensions between particle and water σ_{pw} , between particle and air σ_{pa} and between water and air σ_{wa} . For curved water interfaces like droplets, „that equilibrium contact angle is given by the Young’s equation, whereas the minimized adsorption energy is a function of curvature“ [65].

The contact angle may be observed, e.g., with an even substrate and a water droplet; θ_c is then the angle between the substrate and the curvature of the droplet at the water-air-substrate interface line. There are more sophisticated methods for measuring the contact angle, to be found, e.g., in the review on contact angles and adhesion by [40]. According to [100], the depth h to which a massless spherical particle of radius r is submersed relative to the water-air interface is given by

$$h = r * (1 - \sin(\frac{\pi}{2} - \theta_c)) \quad (2.35)$$

with a water-particle-air interface line of radius $r_0 = r * \sin(\theta_c)$. So, if only surface tensions are considered, non-soluble or not completely wettable particles ($\theta_c < \pi$) remain at the water-air boundary. This effect is used by water striders, commonly also called ‘Jesus bugs’ (fam. Gerridae), to walk on water surfaces, or by mosquito larvae dwelling in water which stick to the water surface for breathing, two phenomena observable in nature on ponds or lakes. This shows the surface tension to be a powerful effect, as has already been reported from experiments with gold foil in water by Galileo Galilei in 1612 [28]. The water surface may be deformed by gravitational pull on the particle, which leads to a variation in the particle position relative to the unperturbed water surface of $h' = F'/\pi\sigma_{wa}$ (see [100] for detailed derivation), with the force $F' = F_g - F_b$ being the difference between the gravitational force of the particle with density ρ , $F_g = -4/3\pi r^3 \rho g$,

and the buoyancy force of the immersed fraction of the particle

$$F_b = \rho_w g (\pi/6) h (3r_0^2 + h^2) = \rho_w g (\pi/6) * r^3 * (1 - \cos(\theta_c)) * (3\sin^2(\theta_c) + (1 - \cos(\theta_c))^2)$$

which is calculated by assuming a spherical cap volume $V_{cap} = (\pi/6)h(3r_0^2 + h^2)$ of the particle being submersed in water of density ρ_w ; for aerosol particles of, e.g., 300 nm diameter and clay mineral source ($\rho \approx 2,6\text{g/cm}^3$ [102]), this deformation is $h' \ll 1\text{nm}$.

2.3 Electrodynamic balance

2.3.1 Levitation of a single water droplet

For the following discussion, a mechanism for the levitation of single water droplets is discussed. While the physics apply to charged masses in general, the expression 'droplet' is used throughout these considerations. Presuming a droplet of mass m with charge q , a superposition of two electric fields can achieve levitation. The subsequent argumentation follows [103] and can be found in more detail in [119, 155].

2.3.2 Compensation of gravity and air drag

To prevent loss by gravity or the drag of an aerosol stream by the droplet, a quasi-static electric field E is well suited. The electric force $F_e = qE$ of an electric field E on the droplet should be equal to the gravitational force of earth F_g and the drag force of air of viscosity η_{air} , which is given by Stokes' drag F_d for sufficiently slow air flows with Reynolds numbers $Re = 2rv/\nu_{air} \ll 1$ (kinematic viscosity of air of density ρ_{air} : $\nu_{air} = \eta_{air}/\rho_{air}$, air velocity v) and droplets with a radius r small enough to keep spherical shape under the drag force:

$$F_e = qE = mg + 6\pi\eta_{air}rv = F_g + F_d. \quad (2.36)$$

An easy solution is given in the case of a plate capacitor, where $E = U_0/d$ for the potential U_0 and the distance d between the plates.

2.3.3 Compensation of lateral movement

A simple plate capacitor is unsuitable for the capture of moving droplets without extensive regulation mechanisms. Considerations on the desired properties of the potential lead to a more sophisticated experimental setup. To keep a droplet in a stable position

\vec{x}_0 , the resulting force on the droplet at this point has to be zero, while the potential has to have a minimum to make it an attracting point. This reasoning leads to the following differential equations:

$$\begin{aligned}\nabla\Phi(\vec{x}_0) &= 0 \\ \Delta\Phi(\vec{x}_0) &> 0\end{aligned}\tag{2.37}$$

An attractive charge at \vec{x}_0 would defeat the purpose of continued droplet storage due to charge equalization, but an electrostatic field with the desired property $\Delta\Phi(\vec{x}_0) = \rho/\epsilon_0$ with charge density ρ and vacuum permittivity ϵ_0 would violate the second condition. The solution for keeping both conditions is an electrodynamic field. For a sufficiently high oscillation frequency ω , the large inertia of the droplet will prevent movement exceeding, e.g., half a droplet diameter. The droplet is then captured in a pseudo-potential that results from averaging the oscillations over time, which satisfies $\Delta\Phi(\vec{x}_0) > 0$ on the timescale greater than an oscillation period without violating $\nabla\Phi(\vec{x}_0) = 0$ at any given point in time. In an alternating field with an amplitude $E_0(z)$ along the direction z , the movement equation of z is given by

$$m\ddot{z} = qE_0(z)\cos(\omega t).\tag{2.38}$$

$z(t)$ may be split up into a 'slow' part averaged over an oscillation period $\bar{z}(t)$ and a fast oscillation part $\zeta(t)$, so

$$z(t) = \bar{z}(t) + \zeta(t) = \frac{\omega}{2\pi} \int_t^{t+2\pi/\omega} z(t') dt' + \zeta_0 \cos(\omega t).\tag{2.39}$$

For field inhomogeneities $E(\bar{z})$ that are small on the scale of the amplitude ζ_0 , the movement equation can be series expanded into

$$m\ddot{z} = m\ddot{\bar{z}}(t) + m\ddot{\zeta}(t) = qE(\bar{z}, t) + q\zeta \frac{\partial E(\bar{z}, t)}{\partial z}\tag{2.40}$$

while neglecting higher orders.

In the case of small displacements, $\zeta(t)$ follows the alternating field at \bar{z} , so

$$m\ddot{\zeta}(t) = qE(\bar{z}, t)\tag{2.41}$$

and consequently

$$\zeta(t) = -\frac{q}{m\omega^2}E_0(\bar{z})\cos(\omega t). \quad (2.42)$$

The overall time average of force on the droplet is then, considering $\overline{\cos(\omega t)} = 0$ and $\overline{\cos^2(\omega t)} = \frac{1}{2}$,

$$\overline{m\ddot{z}} = \overline{qE_0(\bar{z})\cos(\omega t) - \frac{q^2}{m\omega^2}E_0(\bar{z})\cos^2(\omega t)\frac{\partial E(\bar{z}, t)}{\partial z}} = -\frac{1}{4}\frac{q^2}{m\omega^2}\frac{\partial}{\partial z}E_0^2(\bar{z}). \quad (2.43)$$

This force is equal to the negative gradient of the corresponding potential, and the deliberations are analogous in all space directions, so

$$\Phi(\vec{x}) = \frac{1}{4}\frac{q^2}{m\omega^2}E_0^2(\vec{x}). \quad (2.44)$$

One of the many potentials that satisfies the Laplace equation $\Delta\Phi(\vec{x}_0) = 0$ with $\vec{x}_0 = \vec{O}$ is given by the quadrupole solution

$$\Phi = \Phi_0(\alpha x^2 + \beta y^2 + \gamma z^2) \quad (2.45)$$

with

$$\alpha = \beta = -2\gamma. \quad (2.46)$$

So,

$$\Phi(x, y, z) = \alpha\Phi_0(x^2 + y^2 - 2z^2) \iff \Phi(r, z) = \alpha\Phi_0(r^2 - 2z^2). \quad (2.47)$$

This potential can be generated by electrodes in the shape of the equipotential surfaces which is how it was realized in the experiments conducted in this thesis. There are several other possibilities to realize particle levitation with electrodynamic fields that are presented in [22]. A closer look at the ramifications of this solution specifies the conditions under which stable storage is possible, e.g., what a 'sufficiently high oscillation frequency ω ' or what the size of a droplet with 'large inertia' is. Again, a more detailed description of the phase space of stabilizing conditions can be found in [119, 155].

2.3.4 Experimental realization

The infinitely large equipotential surfaces that solve equation 2.47 are realized in gold-covered brass with a diameter $\approx 5\text{cm}$, a height $z \approx 2\text{cm}$ and $\alpha = 1/(r_0^2) = 0,5\text{cm}$. The middle electrode has 8 equidistant drilling holes of 2mm diameter through the curvature closest to the center for droplet injection and observation, the top and bottom electrodes

have each one drilling hole of 3mm diameter through the curvature closest to the EDB center for aerosol streaming, ice nucleation and pressure equalization. Those drilling holes do not impede the intended electrode function. The top and bottom electrode are separated from the middle electrode by a heat-conductive but electrically resistive ring of aluminum nitride to prevent spark gap conduction.

The experimental setup is discussed in more detail in the experimental section.

Chapter 3

Experimental setup and methods

In this chapter, the experimental setup is surveyed and the principal measurement methods are described.

The section concerning the setup begins with the basic experimental setup for levitating single water droplets, as it was used in [103]. A closer look is given to the droplet generator that was used in the experiments. The experimental setup has been modified to lead an aerosol stream by a captured water droplet, so the aerosol system is described. Last in the setup section, and already on the threshold to the methods section, is a description of the temperature correction employed for the measurements.

The methods section begins with a description of the general experimental procedure which is followed by the techniques used to evaluate the recordings of freezing droplets.

3.1 Experimental setup

The basic setup of the experiments conducted in this thesis consisted of a droplet injector and an electrodynamic balance (EDB) based on the principles laid out in [104] as formulated in chapter 2.3.

A detailed description of the setup can be found in [103].

3.1.1 Electrodynamic balance and periphery

The basic setup was used for experiments in which the freezing behavior in water suspensions of different compositions was investigated.

The EDB was connected to a cooling circuit, a high-power voltage source (both AC and DC) and encased in a vacuum chamber to ensure thermal and electric insulation.

Temperature was measured through temperature sensors in contact with the EDB electrodes.

A CCD array measured the droplet position through the scattered light of a diode laser illuminating the droplet. This scatter signal was used to regulate the droplet position through variation of the voltages applied to the EDB electrodes. A CCD camera at an angle of 90° to the laser beam could be used to measure the droplet diameter via Mie scattering.

A high-powered LED light source was used to illuminate the droplet for the high-speed camera. A microscope objective was employed to enlarge the image of a captured droplet.

To ensure the option of ice nucleation in water droplets at any temperature, solid carbon dioxide (“dry ice”) was placed above a chimney through the vacuum chamber to the EDB center. The carbon dioxide sublimated, cooling laboratory air to temperatures at which ice was nucleated. Only a slight oversaturation of carbon dioxide relative to ordinary air was calculated for freezing droplets by this mode of ice nucleation. A controllable air flow was used to keep unwanted ice particles out of the EDB.

Droplets were injected from a dispenser placed close to the EDB through a channel in the vacuum chamber around the EDB.

A schematic of the setup is shown in figure 3.1, a list of details on the peripheral instruments in table 7.1 in the appendix.

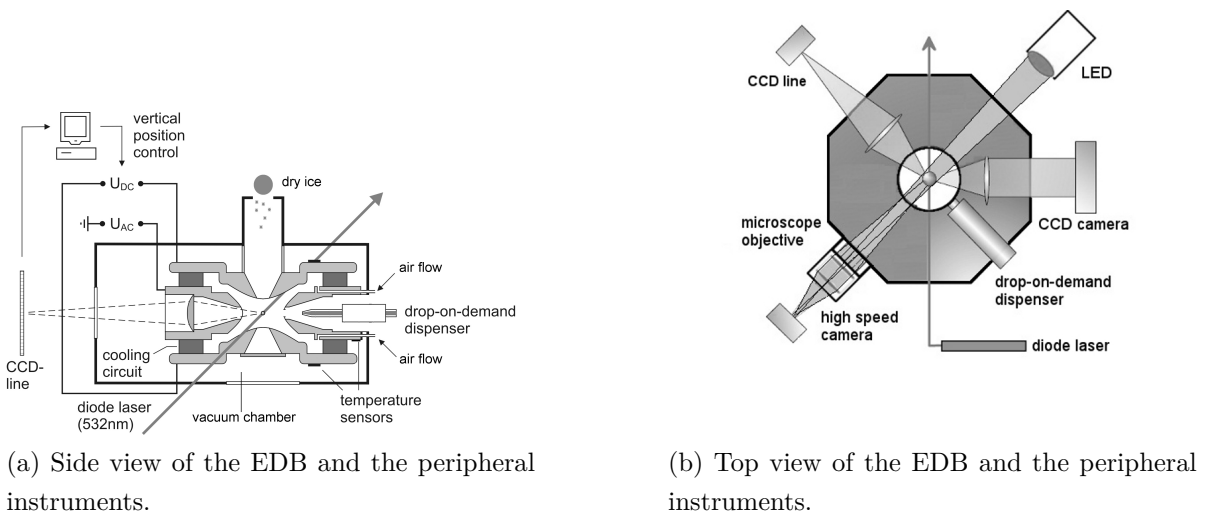


Figure 3.1: Basic setup of the experiments presented in this thesis. Components and their function described in chapter 3.1.1.

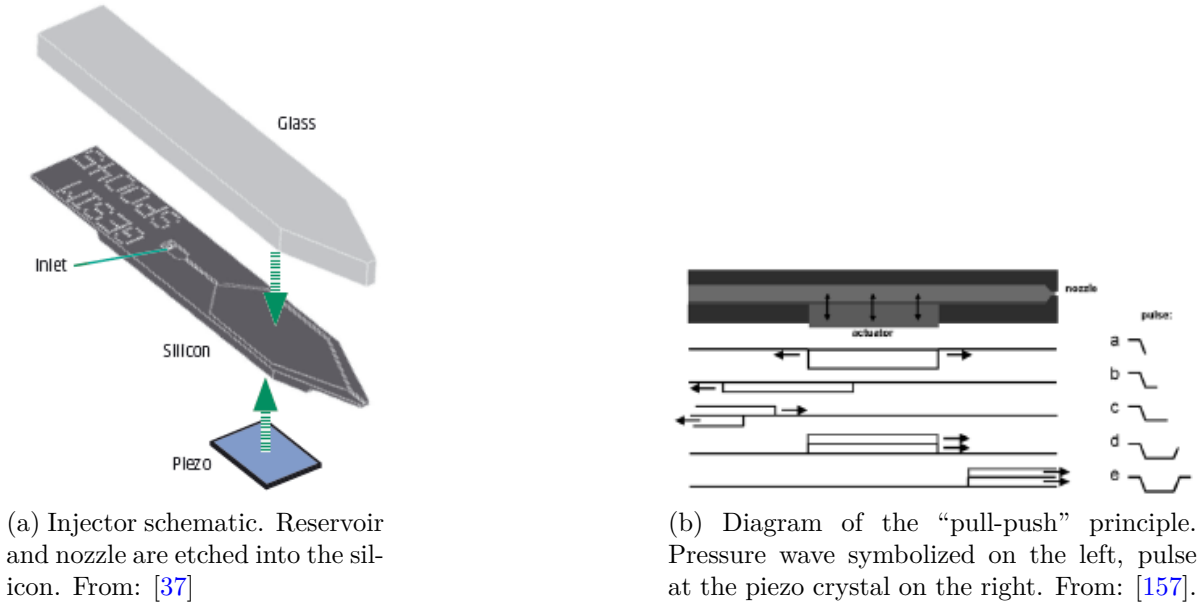


Figure 3.2: Injector schematic and working principle as described in chapter 3.1.2.

3.1.2 Drop-on-demand injector

For droplet creation in the presented experiments, a piezoelectric drop-on-demand injector (model SPIP by the company GeSim) was used that works with the so-called “fill-before-fire” or “pull-push principle” as described in detail in [157].

Such an injector essentially consists of a bigger liquid reservoir, a smaller reservoir close to a piezoelectric element and a channel that leads to a nozzle (see figure 3.2a).

A voltage pulse applied to the piezoelectric element causes it to contract during the rising edge of the pulse and generates low pressure in the smaller reservoir. This causes liquid to flow from the bigger reservoir and the channel towards the small reservoir. The liquid meniscus at the nozzle is pulled into the channel which can be described as the start of a sound wave that propagates through the channel and the small reservoir.

A pressure wave in a channel system may be reflected if the acoustic impedance Z changes; $Z = \rho c/A$, with the liquid’s density ρ , its acoustic speed c and the channel cross section A . The reflection coefficient R and the transmission coefficient T depend on Z as $R = (Z_2 - Z_1)/(Z_1 + Z_2)$ and $T = 2Z_2/(Z_1 + Z_2)$. Assuming c remains constant for the given cross-sections A_i , in which case $R = A_1 - A_2/(A_1 + A_2)$ and $T = 2A_1/(A_1 + A_2)$, the sound wave is reflected at the bigger reservoir (as $A_2 \gg A_1$, with $R \rightarrow -1$ and $T \rightarrow 0$), runs back to the channel and may push liquid through the nozzle. It should be noted that the speed of sound depends on the compliance $\beta = 1/K$, with K being the channel material’s bulk modulus: $c_{eff} = \sqrt{c_0^2/(1 + \rho c_0^2 \beta)}$; for a speed of sound of

$c_0 = 1480$ m/s (in water at 20°C), in a channel consisting of glass, the effective speed c_{eff} is only 3% lower than the speed of sound in bulk water, though. The effect may become more relevant in the case of e.g., graphite channels which have a lower bulk modulus than glass. The geometry of an injector working according to the pull-push principle is such that the pressure wave from the piezocrystal's contraction gets reflected back toward the nozzle.

If the piezoelectric element is discharged in phase with this sound wave running back, the two pressure waves interfere constructively which increases the flow through the nozzle. A diagram of the pressure waves together with the actuation signal at the piezo crystal is shown in figure 3.2b.

In dependence from voltage, which corresponds to displaced liquid volume, rising time of the voltage pulse and pulse width, a droplet may separate from the nozzle. With a well-chosen actuation signal, droplet size manipulation in a considerable range is possible without changing the injector geometry. To investigate the effect of different actuation signals, an arbitrary waveform generator was used. The injector was mounted in a vertical position and the tip was observed with a CCD camera. Details on the equipment are listed in table 7.1. Measurements with a variety of signal forms are presented in chapter 4.1 and discussed in chapter 4.1.

To be captured and stored in an EDB, the droplets from the injector needed to be charged. This was achieved by inducing charges in the water volume of the injector. The first method was placing a metal disc with a drilling hole in the middle close to the tip and applying several hundreds of volts to it, the second was putting the tip of the injector close to the EDB and choosing the right phase in the alternating high voltage for droplet ejection. Both methods were employed in the experiments of this thesis. The second method was considered more elegant, but the phase had to be chosen with a high precision to capture droplets and not have them accelerate onto one of the electrodes.

Due to the proximity of the injector to the EDB, the reservoir needed to be heated lest freezing in the water destroyed the injector. To this end, a small resistance element was fixed to the top glass cover of the injector (see figure 3.2a) with teflon tape and heated by having a small current flow run through it.

3.2 Aerosol system

To broaden the scope of ice multiplication experiments, experiments in which aerosols impinge onto droplets were conducted.

To this end, the experimental setup laid out in chapter 3.1.1 was modified. The

chimney in the top electrode (see figure 3.1a) was connected to a size-selecting aerosol source with a three-way fitting, the bottom electrode was switched to a chimney which was connected to an aerosol counter. A more detailed description of the aerosol setup may be found in [45].

The combination of an instrument capable of size-selecting from a polydisperse flow (a “classifier”) and a particle counter is called a scanning mobility particle sizer (SMPS).

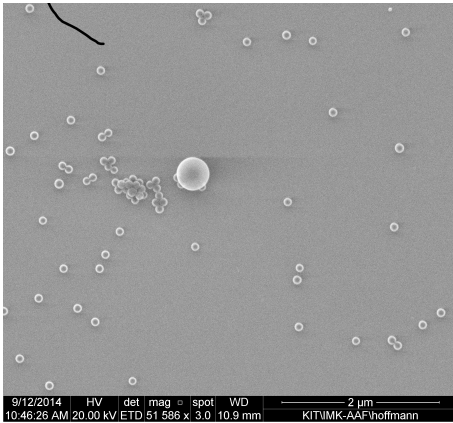
3.2.1 Aerosol sources

Three different aerosols were used to hit the droplet on the surface and to research this effect on droplet freezing (for example images, see figure 3.3).

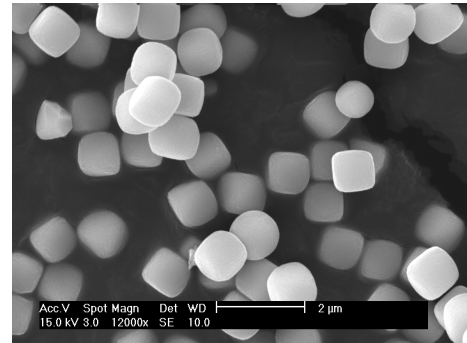
- Polystyrene latex (PSL)
 - Spheres
 - Commonly used for SMPS system calibrations
 - Narrow size distribution, commercially available in sizes from a few nm to several μm
 - Delivered as a suspension, usually with a detergent to prevent agglomeration of the particles

- Hematite
 - Fe_2O_3
 - grown by at the IMK-AAF chemical laboratory
 - Cubic shape with rounded corners
 - One broad size mode

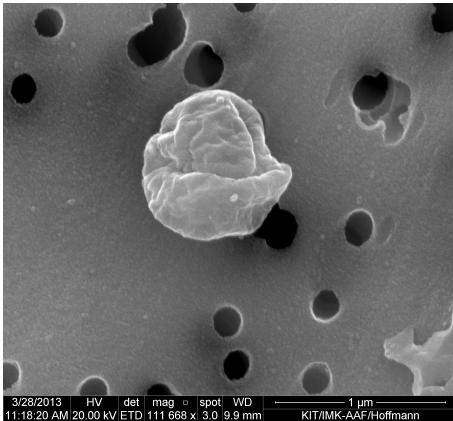
- SNOMAX particles
 - Fragments of *Pseudomonas syringae*
 - Contains highly ice-active proteins
 - Used in snow cannons to promote artificial snow production
 - Polydisperse



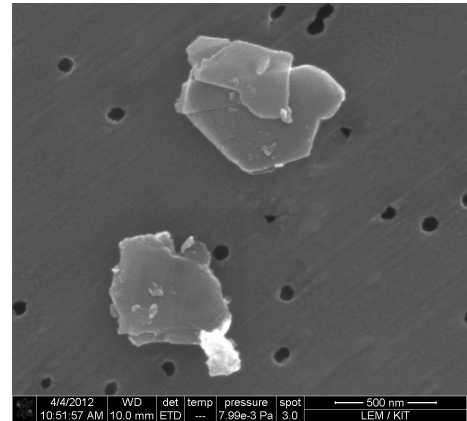
(a) Spherical polystyrene particles of different diameters on a silicon substrate



(b) Cubic hematite particles on a silicon substrate.



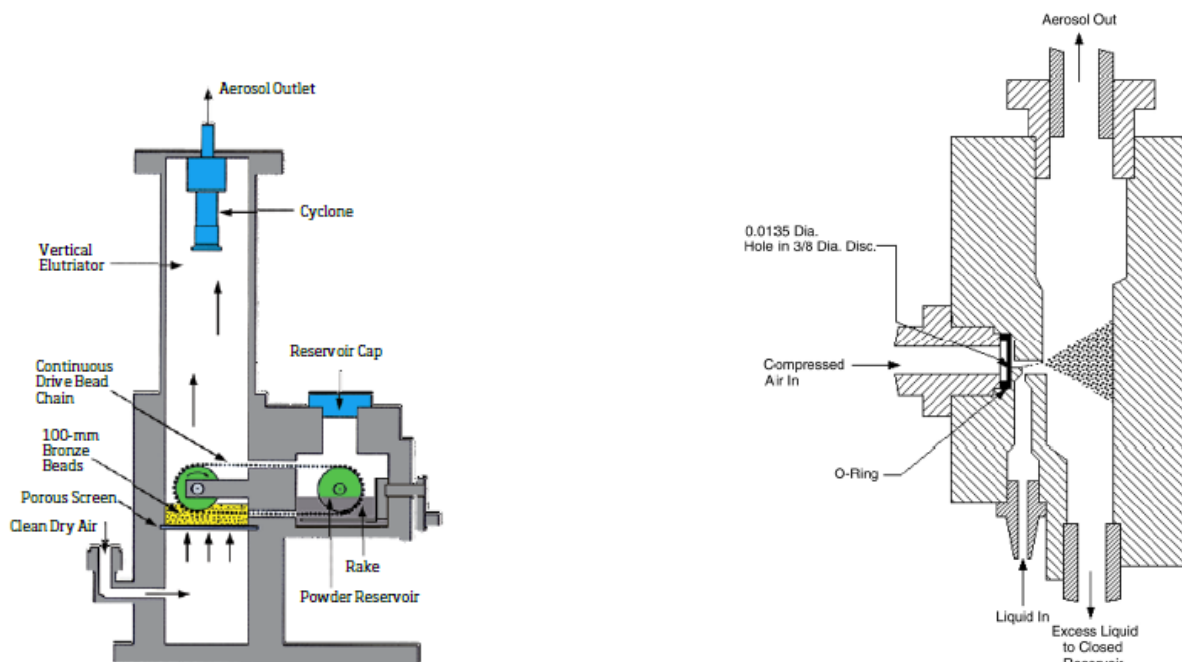
(c) SNOMAX particle (dried up bacterial cell fragments) on a filter.



(d) Kaolinite platelets on a filter.

Figure 3.3: Aerosol particles as observed with an environmental scanning electron microscope (ESEM). Pictures courtesy of Nadine Hoffmann (PSL, SNOMAX) and Alexei Kiselev (hematite, kaolinite).

Hematite powder was aerosolized with a fluidized bed generator, model 3400A by the company TSI. In this setup, the solid substance is placed on a fine mesh. Air is pumped through the mesh, the particles in the powder are brought into motion and bounce off each other. This results in the impression of a fluid to an observer, hence the name. Due to the collisions, particles separate from the bulk material and follow the flow of air; the instrument is schematized in figure 3.4a.



(a) Fluidized bed generator 3400A by TSI, used in experiments with hematite. Source: [142].

(b) Atomizer 3776 by TSI, used in experiments with PSL and SNOMAX. Source: [141].

Figure 3.4: Aerosol generators as described in chapter 3.2.1.

This flow is then lead through a diffusion drier, consisting of a fine mesh tube in a larger tube filled with silica gel, to the classifier for size selection. Experiments with a clean air flow showed no measurable particle numbers behind the drier, so particle contamination by the silica gel could be excluded. The fluidized bed setup is useful for the aerosolization of all kinds of powders and is capable of producing high particle concentrations in an air flow. This is also its downside: if there is only little material available, the fluidized bed system quickly disperses all of the substance, thus limiting experimental time.

SNOMAX and PSL are highly concentrated products, so an approach different to hematite is necessary to prevent waste. A wet dispersion mechanism, the atomizer, was chosen. A schematic is shown in figure 3.4b. A high-pressure (≈ 2 bar) stream of artificial air is pumped through a narrow tube, in which flow speed increases and pressure drops due to Bernoulli's principle. Through the reduced pressure, the substances suspended at low concentrations (< 150 mg/l) in Nanopure water are sucked into a mixing chamber. The air-water mixture then flows through a nozzle (0,0135"=0,343mm diameter) in which the high flow speed fragments large droplets due to drag force into smaller droplets

suspended in an air flow. Larger droplets are sorted out with a precipitator connected to the aerosol outlet of the atomizer. Because of the high volume flow which would exceed the capacity of both classifier and particle counter, only a part of the remaining aerosol is led through a diffusion drier consisting of silica gel which results in a polydisperse aerosol. The excess air is led into the exhaust system in the laboratory.

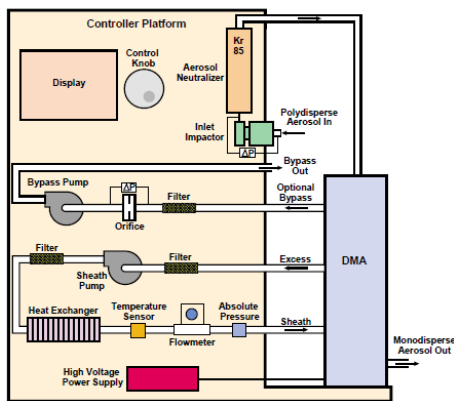
The dried particles then enter the classifier of the SMPS system after passing through an impactor, a plate at a sharp bend in the air stream, where particles impinge that are too inertial to follow the flow.

Once the first liquid volume had been completely atomized, the empty container was switched with the precipitator container and experiments could continue. Suspensions were switched daily, in the case of SNOMAX sometimes twice a day as a decomposition of the biological material was suspected due to the development of a somewhat rotten smell.

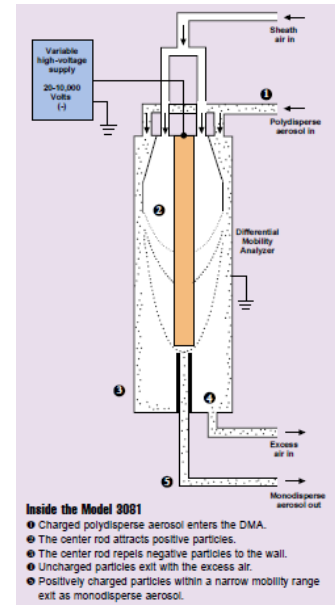
3.2.2 Aerosol size selection

A classifier or differential mobility analyzer (DMA) is a machine capable of selecting particles from an air flow based on their size, shape and density in the form of their aerodynamic mobility (as in equations 2.27 and 2.29). The Series 3080 Electrostatic Classifier by TSI employs electric forces to select a given nominal diameter of particles. To this end, the particles have to have a defined charge which is achieved with a neutralizer. This setup uses a ^{85}Kr source (see figure 3.5a) to ionize the air in a certain volume so that charges on the particles originating from collisions (fluidized bed generation) or previously dissolved ions (atomizer generation) are neutralized by charge equalization. Through statistical probability, most particles carry one or no charge [140].

The aerosol stream then enters a high-voltage capacitor consisting of a steel rod in the middle of a steel tube. A particle-free air flow sheaths the rod from the aerosol stream which is flush with the steel tube. A small gap in the bottom of the rod allows an air flow passage out of the capacitor. Only particles with the right aerodynamic diameter and the right charge will pass through the gap; larger particles will not be sufficiently accelerated by the electric field and leave the capacitor into the exhaust, particles too small will be accelerated too fast and deposit on the rod according to their electric mobility as derived in chapter 2.2.1. By variation of the voltage and the flows – both aerosol and sheath flow – particles can be selected by their mobility to pass through the classifier (see figure 3.5b).



(a) Electrostatic classifier as used in the experiments. Source: (TSI 2001).



(b) Differential mobility analyzer as used in the experiments. Source:(TSI 2001).

Figure 3.5: Classifier system by the company TSI as described in chapter 3.2.2.

3.2.3 Aerosol number

The final component of an SMPS system is a particle counter. In the presented experiments, a Model 3776 Ultrafine Condensation Particle Counter (“UCPC”) produced by TSI was employed, which is capable of detecting aerosols in the range of 20nm-1 μ m.

The light scatter by aerosol particles is generally weak due to their small size which complicates direct measurement of their number. A way to improve their scattering signal is to enlarge them; this is achieved by having a suitable agent condensate onto them. In the Model 3776, a fraction of the aerosol stream is enriched with butanol at supersaturation pressure, the particles are given time to grow and are then streamed by a laser and an optical detector. The flow through the UCPC (300ml/min) is regulated with an internal pump, so the counts of particles per time interval can be converted into the aerosol concentration by division of the particle count per time by the flow. A schematic of the taken from the spec sheet by TSI is shown in figure 3.6.

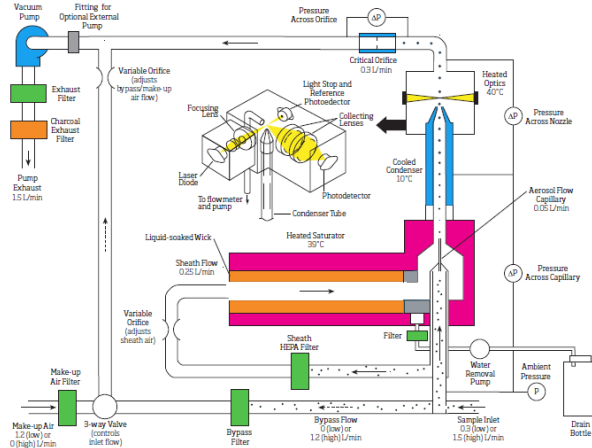


Figure 3.6: Condensation particle counter as used in the experiments. Source: [143].

EDB and SMPS The aerosol flow from the classifier was connected to the top electrode chimney and the UCPC to the bottom electrode chimney of the EDB. The volume flow through the UCPC was set at 300 ml/min and the injector inlet was not completely airtight, so to prevent particle contamination from the laboratory air at the UCPC, a slight overpressure was necessary in the EDB. This was achieved by setting the flow through the classifier to ≈ 360 ml/min and having a three way fitting which was open to one side to connect the air flow from the classifier to the EDB. This way, excess volume flow could cause no damage to the UCPC or the injector but laboratory particles were prevented from entering the EDB. As a secondary effect, ice particles could be generated at any time by placing a piece of dry ice above the open side of the three way fitting and by deactivating flow through the classifier. The underpressure caused by the pump in the UCPC would then suck air by the dry ice and entrain ice particles to cause freezing in a droplet levitated in the EDB upon impact.

3.3 Temperature correction

EDB temperature was varied between -36°C and 0°C , which was not identical to the droplet temperature.

The dry air flow used to keep ice and other particles out of the EDB in the first experiments and the aerosol stream led by the droplet in later experiments caused a difference of several $^\circ\text{C}$ by enhancing evaporative cooling in the droplet. With the equations (see [110])

$$T_d - T_\infty = \frac{L_e D_v M_w}{k_{air} R} \left(\frac{p_v(T_d)}{T_d} - \frac{p_v(T_\infty)}{T_\infty} \right) \left(\frac{f_v}{f_h} \right) \quad (3.1)$$

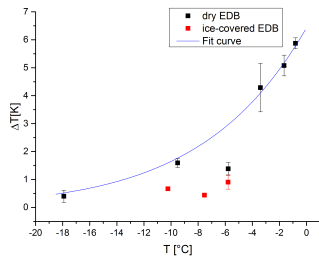
and

$$a \frac{da}{dt} = -\frac{M_w D_v}{\rho_w R} \left(\frac{p_v(T_d)}{T_d} - \frac{p_v(T_\infty)}{T_\infty} \right) f_v \quad (3.2)$$

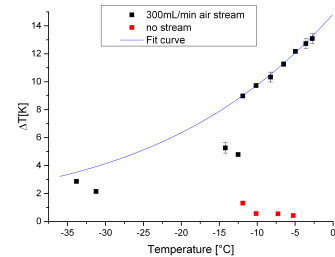
for the difference in temperature between droplet and ambient temperature: $T_d - T_\infty$ and the evaporation or growth rate of a droplet of radius r : $r \frac{dr}{dt}$, with the evaporation heat L_e , diffusivity of water vapor in air D_v , the molar mass of water M_w , the heat conductivity of air k_a , the gas constant R , the saturation vapor pressures over water p_v , the water density ρ_w , the ventilation coefficient f_v and the heat ventilation coefficient $f_h \approx 1$ for the observed droplet sizes and flow speeds. As it was easily possible to measure the decrease of droplet diameter over time with the experimental setup, the temperature difference could be calculated with

$$\Delta T = \frac{L_e \rho_w}{2k_{air}} \frac{da^2}{dt} \quad (3.3)$$

the results of which are presented in figure 3.7 for different stream conditions through the EDB .



(a) Temperature difference between EDB and droplet at 120ml/min air flow. The EDB was deemed “dry” when no visible ice was coating its insides.



(b) Temperature difference between EDB and droplet at 300ml/min air flow and at no flow.

Figure 3.7: Temperature difference between droplet and EDB, calculated from the rate of evaporation. The fit curves are of the shape $\Delta T = \Delta T_0 + A_1 * \exp((T - T_0)/T^*)$.

The fit curves obtained in figure 3.7 were used for temperature corrections in all subsequent figures where air and aerosol flows were applied.

3.4 Methods

3.4.1 General experimental procedure

The general procedure in the freezing experiments consisted of the following steps:

- Droplet injection
- Droplet capture in the EDB
- Short waiting time (several seconds) until droplet has reached temperature equilibrium with the ambient atmosphere
- Ice nucleation
 - Contact nucleation via ice
 - * basic setup: the air flow through the EDB is briefly switched off so a small number of ice crystals can enter the EDB center; the ice crystals were nucleated by a piece of sublimating ice above a chimney in the top electrode of the EDB
 - * aerosol setup: the air flow from the classifier is briefly switched off so ice crystals are sucked into the EDB center by the internal pump of the particle counter; same source of ice particles as in the basic setup
 - Immersion nucleation via kaolinite or SNOMAX particles in injected droplets. The top chimney is closed in immersion experiments to prevent particle contamination from laboratory air
- Emptying, rinsing and refilling of the injector after half an hour of experimenting. It had been noticed in PSL suspension experiments that the fragmentation rate dropped after ≈ 45 minutes which suggested particle depletion in the injector's reservoir by sedimentation or Brownian motion to the injector walls
- Visual recognition of freezing in video recording
- Manual backwards triggering of video recording
- Examination of video
 - Saving of video (several minutes)

In chapter 2.1.2, it was discussed that the freezing of a supercooled droplet consists of two steps on substantially different time scales.

The propagation speed of ice in supercooled water is in the range of several cm/s to m/s, so a droplet of 100 μ m is expected to freeze in the course of less than 10ms (e.g., in 0,14ms at -10°C). For a detailed observation of this process, a time resolution of 100 μ s per time step ($\hat{=}$ 10000fps) or better is advisable.

The second freezing step happens on a time scale of 100ms to seconds for a droplet of 100 μ m (e.g., 513ms at -10°C). As it will be found in the results, the separation speed of droplet parts during a fragmentation is in the range of $O(1\text{m/s})$; the field of vision was generally 300 μ m across, so the observation time for a fragmentation is in the order of 0,3ms.

This situation posed a dilemma: while a high time resolution lead to better measurements in the first freezing step and the fragmentation, it also lead to many recorded frames in between where little occurs from frame to frame and consequently leads to large video files ($O(\text{GByte})$). An upper limit was also given by the available buffer space in the camera: for videos exceeding 150.000 frames per second, maximal recording time is less than 2 seconds for videos with a field of vision reliably covering the whole droplet. Much higher time resolutions are thus limited by the reaction time of the operator. Low time resolution, on the other hand, caused less data volume and thus faster video generation, but information was inevitably lost. The more precise information from fewer videos was deemed to be the sensible choice.

3.4.2 Video evaluation

3.4.2.1 Freezing steps

The propagation of ice is detected by the change of scattered light intensity at water-ice boundaries. On an individual image frame this corresponds to the brightness variation of the pixel representing the specific area of the droplet. To quantify this brightness variation, a discrete Laplace filter is applied to the brightly illuminated circular area in the centered on the droplet image (see figure 3.8 c) for an example).

A Laplacian, being applied to a grey-level picture, intensifies areas of rapid grey intensity change while it produces zero values in areas of constant brightness. After applying the filter, the absolute values computed for each pixel are averaged over the analysis area. Thus, a non-dimensional numerical value can be assigned to the apparent density of water-ice boundaries in the analysis area of every droplet image. This value, called “roughness” R , allows for a simplified analysis of the freezing progress. The

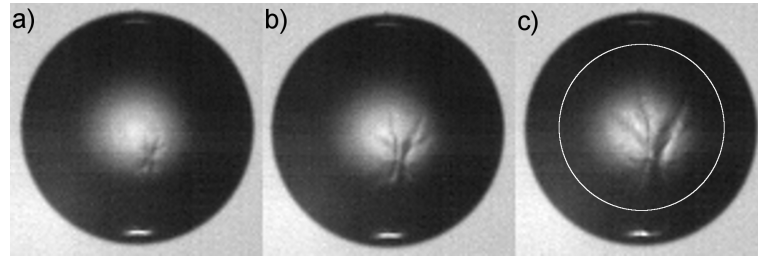


Figure 3.8: Ice propagation in a supercooled droplet ($d=105\mu\text{m}$) of initial temperature $-10,3^\circ\text{C}$. a) $t= 0,0427$ s, shortly after the freezing start; b) $t= 0,04289$ s, roughly in the middle of the first rising slope; c) $t = 0,0431$ s, at the local maximum of R . The white circle in c) surrounds the area in which roughness was analyzed to avoid systematic error from the glare at the bottom of the droplet.

evaluation program for R and other droplet properties was custom-build by professor Thomas Leisner at the IMK-AAF.

During the first freezing, R changes notably in few microseconds (see figure 3.9b).

As ice growth slows down during the second freezing stage by a factor of >100 , the end of the first freezing stage can be recognized as a local leveling of the roughness curve. The final reduction of R (see figure 3.9a) can be attributed to the end of the second stage of freezing.

All these steps can be found in figure 3.10, where the complete freezing of a droplet is depicted.

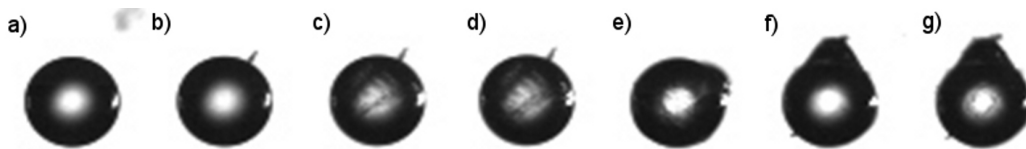
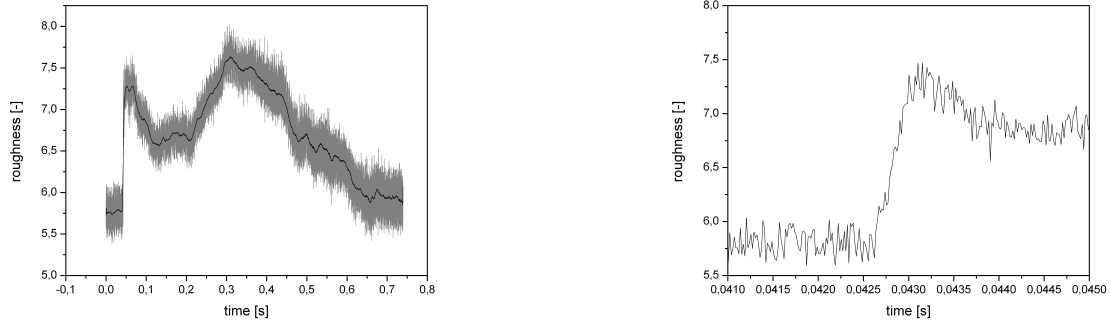


Figure 3.10: Steps in the freezing process in a droplet of $96\mu\text{m}$ diameter at $-9,8^\circ\text{C}$ initial temperature. a) $t = 0$ ms: ice particle approaching droplet; b) $t = 0,57$ ms: particle has hit the droplet, initiation of the first freezing stage; c) $t = 1,5$ ms: propagation of ice through droplet; d) $t = 1,8$ ms: end of first freezing stage; e) $t = 561$ ms: droplet deformation due to internal pressure build up; f) $t = 637$ ms: roughness reaches local minimum; g) $t = 652$ ms: final state of the droplet.

With this approach, two methods for measuring the propagation speed of ice in supercooled water are available: the frame-by-frame analysis of the position of the leading tip of an ice crystal as it is possible in figure 3.8 and the estimation via dividing the droplet diameter by the first freezing step time taken from the roughness curve as it is possible in figure 3.9b.



(a) Complete roughness curve over time. First freezing is visible as a steep rise of R at the beginning.

(b) Detail from complete roughness curve. The fast increase of the roughness curve is corresponding to the first freezing step.

Figure 3.9: Typical roughness curve. Variation during second freezing step ($t = 0,05\text{s} - 0,35\text{s}$) due to rotation of the droplet. Local minimum and slight rise at the end signify end of freezing. The grey area shows the random variation of the roughness value R , the black solid line shows R averaged over 300 frames. The droplet evaluated is the same as in figure 3.8.

The aim was to analyze every frame of every recording, extract the information (like droplet size, aspect ratio, roughness) and save it to a data sheet. In this way, the information on the freezing process was kept even if the video was cut to reduce its size for saving memory space. This was primarily done for being able to cut the second freezing step, which was relatively long and uninteresting in comparison to the first freezing step at the beginning of the freezing and possible secondary ice mechanisms at the end.

3.4.2.2 Fragmentations

The time resolution of the camera allows for an analysis of the fragmentation process kinetics. Once the freezing droplet has broken up completely into two parts, the center of mass of each fragment is appraised and noted. From the difference in speeds and initial droplet size, it is also possible to estimate the relative masses of the fragments and thus their kinetic energies. An example of such a fragmentation with estimated centers of mass is shown in figure 3.11.

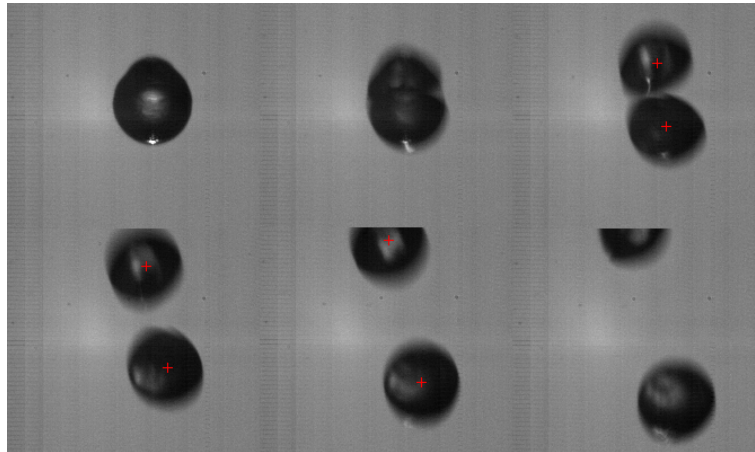


Figure 3.11: Evaluation method of the kinetics of a fragmentation in a droplet of $88\mu\text{m}$ size and a temperature prior to freezing of $-18,62^\circ\text{C}$. Red crosses mark the estimated position of each fragment's center of mass used to measure their individual speed. Time step between each frame: $16,7\mu\text{s}$.

Chapter 4

Results

This chapter presents the results of the measurements conducted for this thesis. It consists of four sections: droplet size manipulation, ice propagation speed in supercooled water, fragmentations and bubbles.

It had been found in literature that the size of droplets can be varied without changing the geometry of the droplet generator. Data on the size variation, based on alternative actuation to the standard mode, is produced.

Ice propagates in supercooled water with a speed dependent on temperature. Measurements on this speed and observations on the appearance of the propagating ice are shown.

The process of fragmentation had been identified as a mechanism in which more than one ice particle emerges from the freezing of water droplets. The occurrence of fragmentations in dependence of solid and soluble matter in and on droplets is evaluated.

Bubbles growing on freezing droplets were found to be a possible mechanism of ice splinter production. The frequency of bubbles in dependence of solid and soluble matter in and on droplets is presented.

4.1 Droplet size manipulation

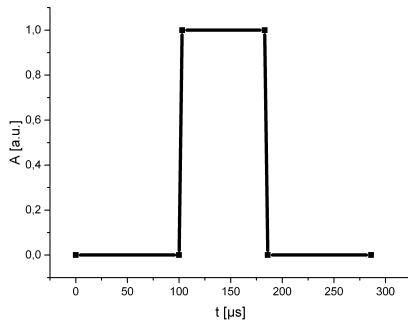
In the presented results on droplet size manipulations with different actuation signals, the time scale of the rising or falling edge of an individual square pulse is $\approx 3\mu\text{s}$. Combinations of square pulses were chosen because the power source used in all freezing experiments employed square pulses with a comparable rising time.

4.1.1 Single pulse variation

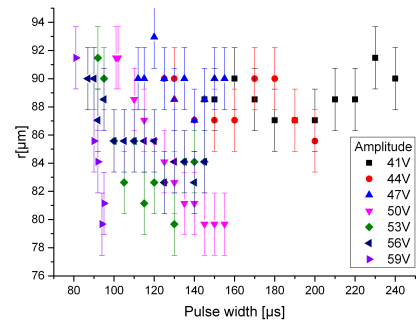
It was demonstrated by [35] that by variation of the dwell time between rising and falling edge of the pulse in a pull-push droplet generator (see chapter 3.1.2), droplet volume could be varied to about 25%, with a maximum at a certain resonance time. Similar results were found in experiments with the injector used in this thesis. With a length of $\approx 2\text{cm}$ of the smaller reservoir and a speed of sound in water of 1500m/s , the optimal interference time should be around $133\mu\text{s}$ which was used as the default pulse length for the following experiments. Voltage and pulse width were varied so that droplet generation took place with a single droplet separating from the nozzle.

If pulse width or voltage was too low, droplet generation did not take place; for pulse widths and amplitudes over a certain limit, satellite droplets were generated. The measurements in which satellite droplets occurred are not presented.

The pulse shape and droplet size in dependence from pulse width and actuation amplitude are depicted in figure 4.1.



(a) Single pulse shape schematic

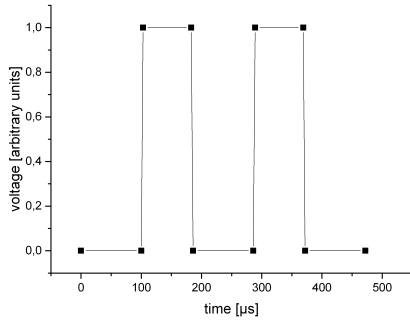


(b) Droplet size in dependence of actuation pulse width and amplitude

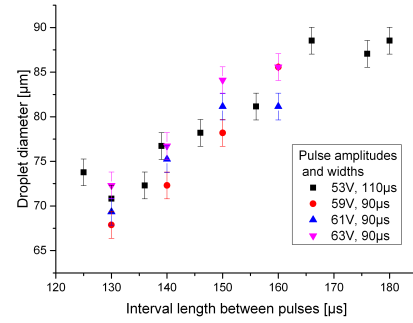
Figure 4.1: Single pulse variation experiments

4.1.2 Double pulse variation

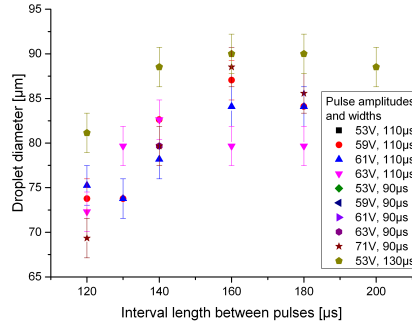
A double pulse or “M-shape” [35] signal (see figure 4.2a) can help to “promote the separation of liquid from the nozzle orifice” [26] and “droplet formation [can be] precisely controlled” [129] in comparison to a single pulse signal. By varying pulse heights, lengths and relative distances smaller droplets could be generated, as the experimental results depicted in figure 4.2 show.



(a) Double pulse shape schematic



(b) Droplet size in dependence of actuation pulse widths, amplitudes and interval length between pulses. Pulse widths and amplitudes were chosen to be equal.



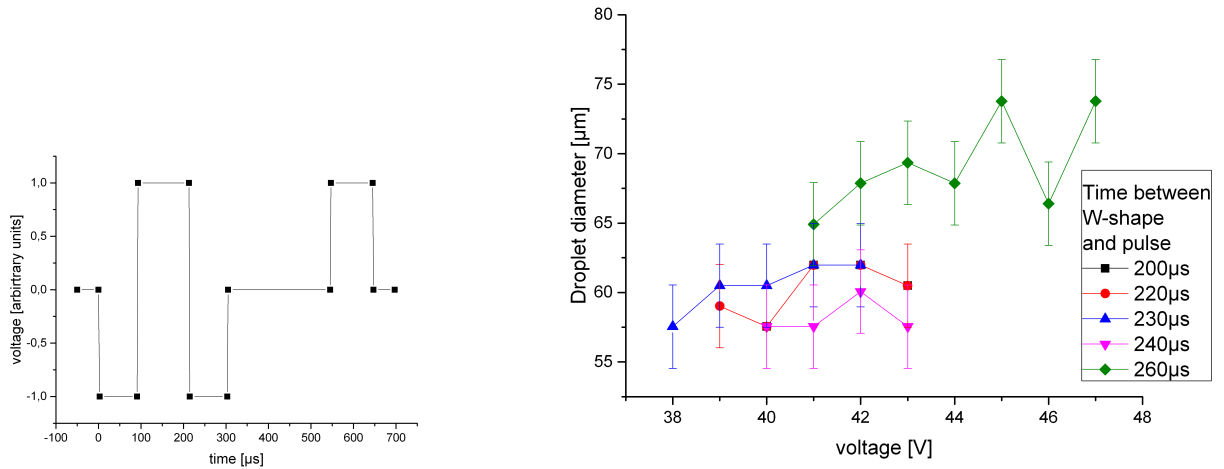
(c) Droplet size in dependence of actuation pulse widths, amplitudes and interval length between pulses. Pulse widths were chosen to be equal, the second amplitude was 75% of the first one.

Figure 4.2: Double pulse variation experiments

4.1.3 W-shape pulse variation

In [16], a more sophisticated waveform resembling a W-shape (see figure 4.3a) is proposed. Experiments with variations on this idea regarding pulse heights and lengths did not generate droplets; the addition of a single pulse after a certain interval lead to an appreciable size reduction (see figure 4.3b).

In the W-shape signal, polarity changes for two pulses. By applying an offset voltage of a pulse amplitude at least 1200 μ s before the actual signal, polarity change could be avoided.



(a) W-pulse shape schematic

(b) Droplet size in dependence of actuation pulse amplitudes and time interval between W-shape and single afterpulse. Negative pulse widths at maximal amplitude of 88 μs, positive pulse width at maximal amplitude in W-shape of 120 μs, single pulse width of 98 μs.

Figure 4.3: W-shape pulse variation experiments

4.1.4 Triple pulse variation

There was no justification for triple pulse actuation from literature, the experiments presented in figure 4.4 were conducted out of curiosity.

4.1.5 Pulse combinations in the EDB

To complete the experiment series, actuation signals that allowed for size variation were applied to an injector at an EDB at a temperature of -18°C . Five signals were chosen to measure their effect under actual experimental conditions: a single pulse signal, three triple pulse signals for both smaller and larger droplets and a W-shape signal as detailed in table 4.1 and shown in figure 4.5a. Amplitudes were varied so droplet capture was possible. The results of the measurements are depicted in figure 4.5.

4.2 Ice propagation speed in a droplet

The high-speed recordings of freezing droplets had a sufficient time resolution to measure the propagation speed of ice in supercooled water. For a description of the evaluation

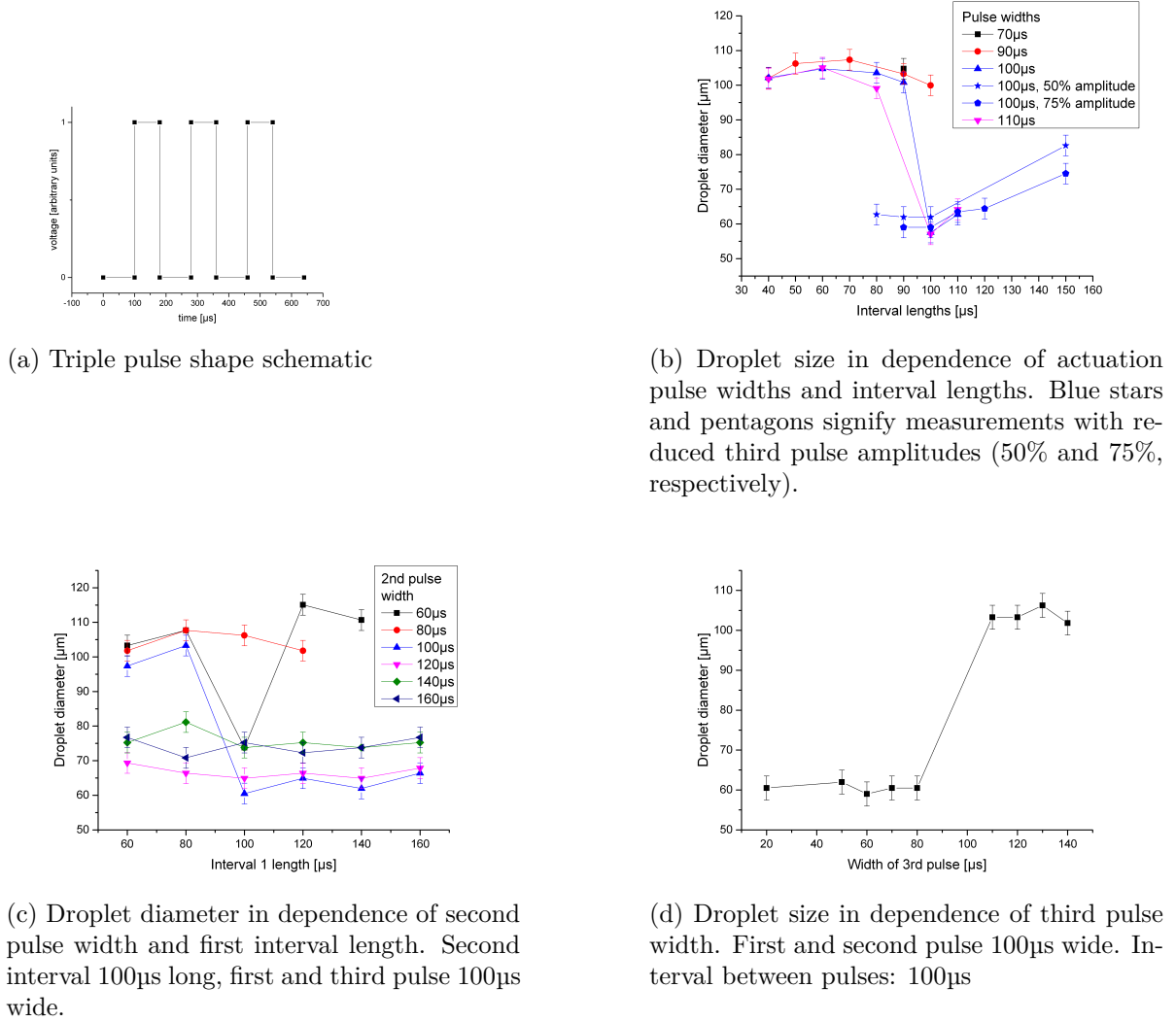
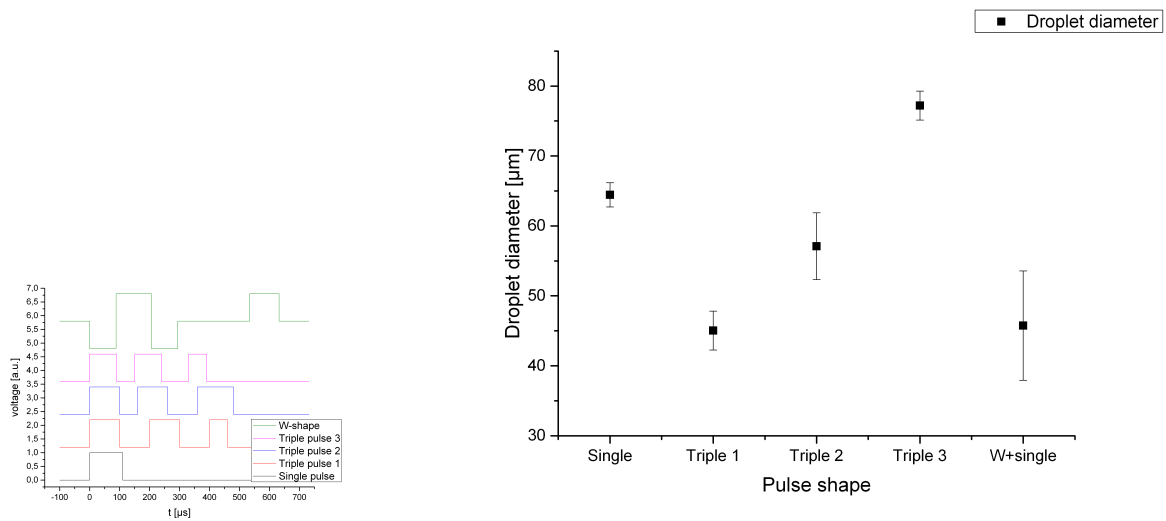


Figure 4.4: Triple pulse variation experiments

Pulse	$t_{p,1}$ [μ s]	$t_{i,1}$ [μ s]	$t_{p,2}$ [μ s]	$t_{i,2}$ [μ s]	$t_{p,3}$ [μ s]	$t_{i,3}$ [μ s]	$t_{p,4}$ [μ s]
Single	110						
Triple 1	100	100	100	100	60		
Triple 2	100	60	100	100	120		
Triple 3	90	50	90	90	60		
W	-88	0	118	0	-88	230	98

Table 4.1: Pulse parameters as used in the experiments presented in figure 4.5. t_p stands for pulse width, t_i for interval length. A negative time denotes a pulse of negative polarity.



(a) Schematic of pulses used in experiments in the EDB

(b) Droplet size in dependence of actuation pulse widths and amplitudes

Figure 4.5: Pulse variation experiments in the EDB

method, see chapter 3.4.2.1.

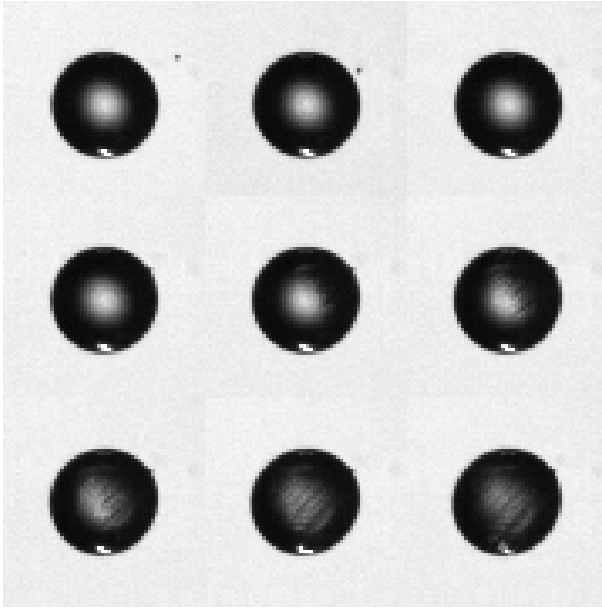
After ice nucleation had taken place, be it in contact mode with ice crystals or SNO-MAX particles or in immersion mode nucleation with SNOMAX, ice grew throughout the supercooled volume originating from the ice nucleus. Two general shapes of growth could be distinguished by their optical appearance:

Dendritic growth A main branch with a tapered tip propagated through the droplet, generally through the center of the droplet, which broadened once the tip had moved on. Behind the tip, side arms of lesser width branched off at an angle of $\approx 60^\circ$ in which a similar behavior was observed; individual tertiary branches could in most cases not be resolved with the camera, but a change in light intensity to the sides of secondary branches suggested their occurrence. Needles like in figure 4.8 were also grouped with dendritic growth, unless the growth happened in a “zig-zag” shape.

Frontal growth A parallel front of ice propagated through the droplet, generally through the center (see figure 4.6 for example).

The frequencies of occurrence of each growth mode in nanopure water droplets is displayed in figure 4.7a.

Two other growth modes are included in this graph: ‘Zigzags’ denotes dendritic growth in droplets in which the dendrite apparently changes propagation direction upon



t[μ s]		
0	127	153
300	433	480
533	600	673

Figure 4.6: Frontal growth in a droplet at $-22,3^{\circ}\text{C}$, droplet diameter $90\mu\text{m}$. The nucleating particle is seen to hit the droplet from the top right side. Position of time value in table corresponds to picture at the same position.

reaching the droplet perimeter, 'unidentified' denotes freezing droplets in which no clear attribution of a growth mode was possible. In figure 4.8, a zigzag freezing event is presented.

Having established the close connection of visual roughness and the freezing process in chapter 3.4.2.1, a first freezing step speed could be calculated by dividing the droplet diameter by the time step length obtained from roughness measurements. In figure 4.7b, these first freezing speeds across temperatures are resolved by the growth modi. While this 'speed' certainly has the dimension of m/s, it is conceivable that local heating might impede the propagation of ice towards the end of the first freezing step. To preclude heating effects, a more differential approach to the ice propagation measurement was applied as well. The position of the tip of the main branch or a point in the ice front was measured by a frame-by-frame analysis so a propagation speed could be calculated (see figure 4.9).

The influence of PSL particles on the differential propagation speed of ice in supercooled water was also investigated, the results of these measurements are displayed in figure 4.10.

The ice propagation speed and the droplet diameter are compared in figure 4.11, the



(a) Relative occurrence of the major growth modi over temperature.

(b) Droplet diameter divided by first freezing step time as measured with roughness evaluation over temperature. Error bars represent standard deviations.

Figure 4.7: Growth modi occurrence and respective diameters divided by the first freezing time over temperature prior to freezing as observed in 688 freezing experiments of nanopure water droplets in which freezing was nucleated with ice crystals.

fit functions to the measurement points is given in table 4.2.

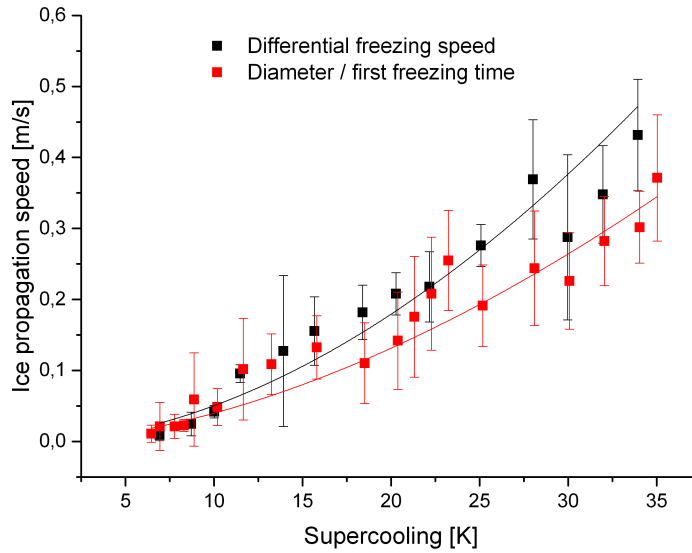


Figure 4.11: Differential first freezing speed and droplet diameter divided by first freezing step time over droplet temperature prior to freezing. Error bars represent standard deviations. The fit curves are of the shape $v = a * \Delta T^b$, with supercooling $\Delta T = (T_m - T)/K$. Coefficients and exponents are presented in table 4.2.

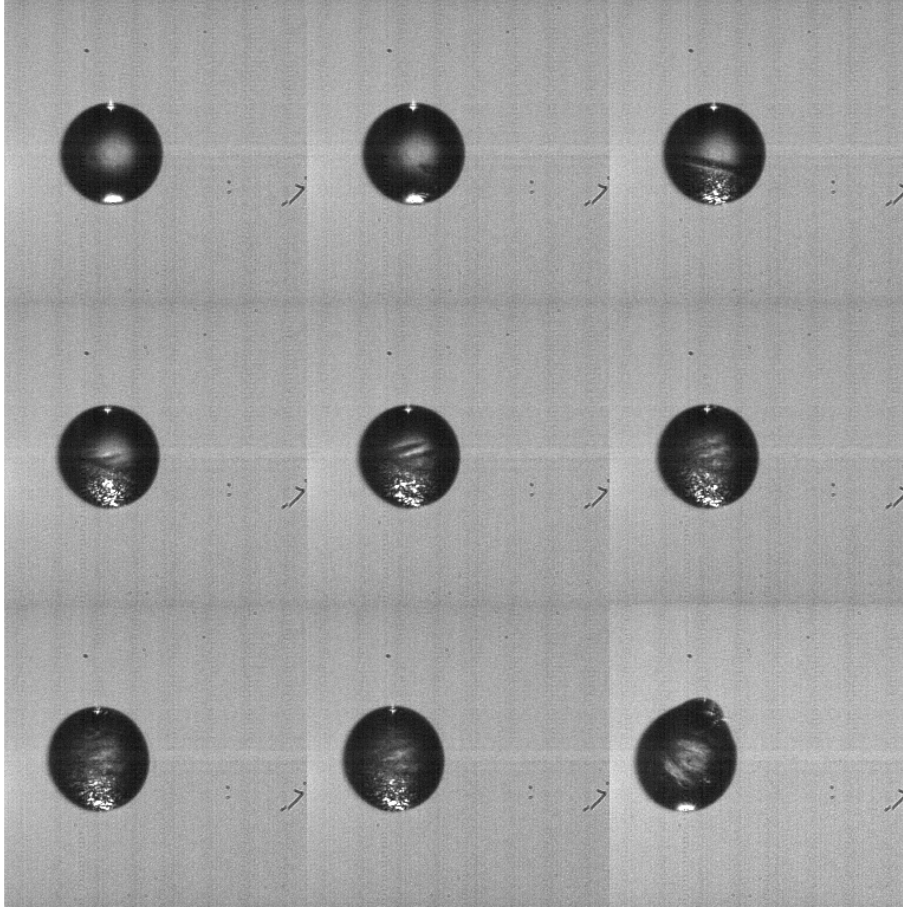


Figure 4.8: “Zigzag” freezing event. From top left to bottom right. $t=0\text{ms}$: Droplet appearance at ice nucleation (extrapolated from propagation speed of ice dendrite); $t=0,14\text{ms}$; $t=0,26\text{ms}$; $t=0,42\text{ms}$; $t=0,56\text{ms}$; $t=0,72\text{ms}$; $t=0,94\text{ms}$; $t=1,3\text{ms}$: final droplet appearance after first freezing; $t=179\text{ms}$: final view on droplet, $20\mu\text{s}$ before a fragmentation takes place.

Measurement principle	Fit function	a [m/s]	b
<i>Differential</i>	$v = a * \Delta T^b$	$(0,75 \pm 0,33) * 10^{-3}$	$1,83 \pm 0,14$
$\frac{\text{Droplet diameter}}{\text{First freezing step time}}$	$v = a * \Delta T^b$	$(0,76 \pm 0,25) * 10^{-3}$	$1,72 \pm 0,10$

Table 4.2: Fit curves to the differential first freezing speed and to the droplet diameter divided by first freezing step time.

4.3 Fragmentations

Previous experiments [103] have shown the frequency of fragmentations to be virtually nonexistent in pure water droplets and markedly higher for droplets containing partic-

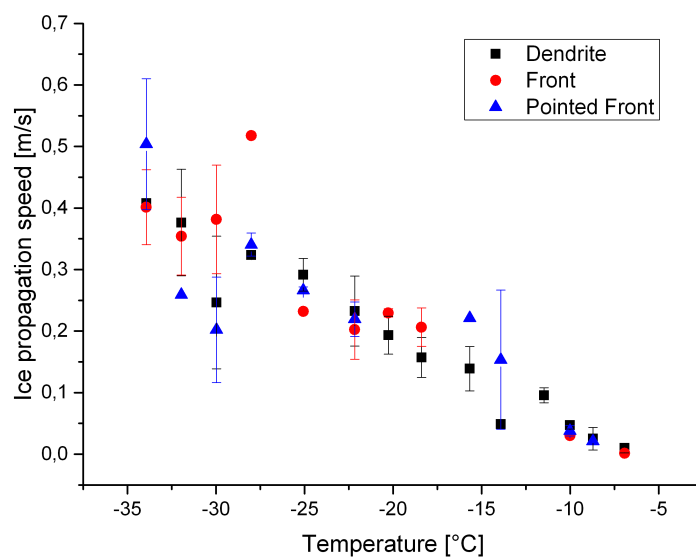


Figure 4.9: Differentially measured ice propagation speed in supercooled droplets as measured by a frame-by-frame analysis of ice growing through the brightly illuminated droplet center, resolved by growth modi, over temperature. 'Pointed front' denotes a growth which showed characteristics of both dendritic and frontal growth; no main branch was clearly visible, yet the front progressed in a shape resembling a dendrite with an opening angle of $\approx 120^\circ$. 'Temperature' denotes the droplet temperature prior to freezing.

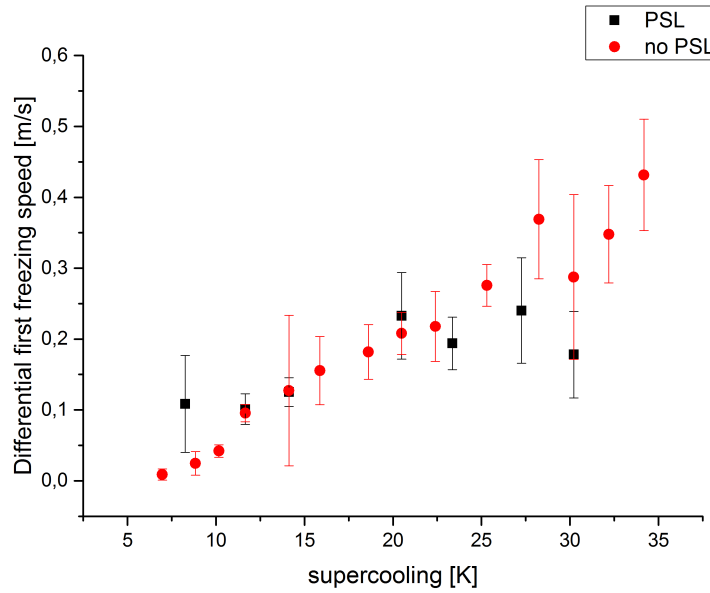


Figure 4.10: The effect of PSL particles ($d=400\text{nm}$) in the droplet on ice propagation speed. 'Temperature' denotes the droplet temperature prior to freezing.

ulate matter. In the temperature range between those two limits, quantitative measurements were necessary. The factors deemed influential on fragmentation frequency were

Temperature For temperatures close to 0°C , it would be expected that only few fragmentations take place, as the second freezing time becomes long (see paragraph 2.1.2.2 and equation 2.21), so relaxation of the stresses in the ice shell should be possible. For very low temperatures, the fraction turned into ice in the first freezing step might become so large (see equation 2.14) that the liquid volume in the core would not contain sufficient internal energy to cause failure in the ice shell .

Particle size There has to be a lower limit, at least in the range of gas molecules, below which lattice defects caused by particles become negligible for material strength under the conditions in a freezing droplet. An upper limit for size is given by the droplet size, when the concept of particle suspension fails.

Particle concentration More particles may mean more frequent fragmentations.

To ascertain the influence of these parameters, several thousand freezing experiments were conducted across the range of -36°C to -8°C . Fragmentations, as well as the bubbles investigated in chapter 4.4, took place at $0,6t_2 - 0,9t_2$, with t_2 being the total freezing time as derived in chapter 2.1.2.2.

4.3.1 PSL suspension experiments

In the experiments with PSL suspensions, particle size was taken to be 28nm and 400nm, which are common sizes for atmospheric aerosols, and particle concentration was varied between nominally 3,6 and 1800 particles per droplet by suitable dilution of PSL suspensions. The results can be seen in figure 4.12.

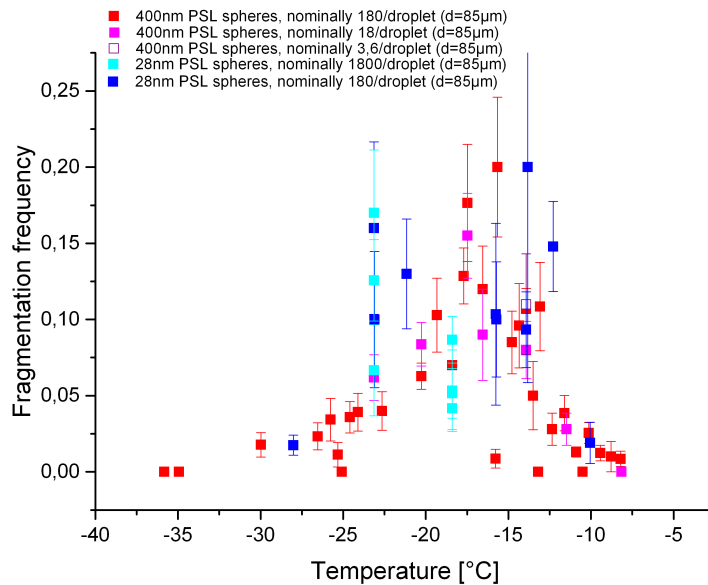


Figure 4.12: Frequency of droplet fragmentation in dependency of temperature and particles in the droplet. Red hued squares represent experiments with droplets containing polystyrene spheres of 400nm diameter, blue hued circles for 28nm diameter. Error bars represent standard deviations. This data was also presented in [96].

Particle diameter affected droplet break-up occurrence. While both 28nm and 400nm polystyrene spheres enabled ice multiplication to take place, the smaller particles showed higher frequencies over a broader temperature range. The peak value in frequency was higher for 400nm particles, though.

The nominal concentration particle concentration could be varied between 3,6 to 180 and 180 to 1800 particles per droplet ($d=85\mu\text{m}$) for 400nm and 28nm spheres, respectively, without an effect on break-up frequency outside of the errors of each measurement series at a given temperature (there are at least 50 freezing experiments behind each measurement point).

4.3.2 Kaolinite suspension experiments

As a proxy for atmospherically relevant particles, the clay mineral kaolinite (see figure 3.3d) was chosen and injected into the EDB as a suspension of 0,01g/l, with particle diameters $< 10\mu\text{m}$ with the temperatures and number of experiments specified in table 4.3.

T [°C]	Frozen droplets	Fragmentations	Fragmentation frequency [%]
-20,3	127	3	$2,4\pm 1,4$
-22,63	202	0	0
-23,12	86	0	0
-24,02	179	1	$0,6\pm 0,6$
-26,94	32	4	$12,5\pm 6,25$

Table 4.3: Results of experiments with droplets containing 0,01g/l kaolinite with regard to fragmentations.

The upper limit in temperature was set by the low ice nucleation capabilities of kaolinite at temperatures above -20°C .

4.3.3 Dilution and solution experiments

To investigate into the influence of solvents, a 400nm PSL suspension ($O(10^3)$ particles/droplet) was filtered through a NALGENE 0,2 μm cellulose acetate membrane filter and compared with an unfiltered sample. It was injected into the EDB at -14°C which had led to a considerable fraction of fragmenting droplets (see figure 4.12). The results are depicted in figure 4.13. It should be noted that between experiments with filtered and unfiltered suspension the injector was flushed and 50 experiments with nanopure water were conducted in which no fragmentations were observed.

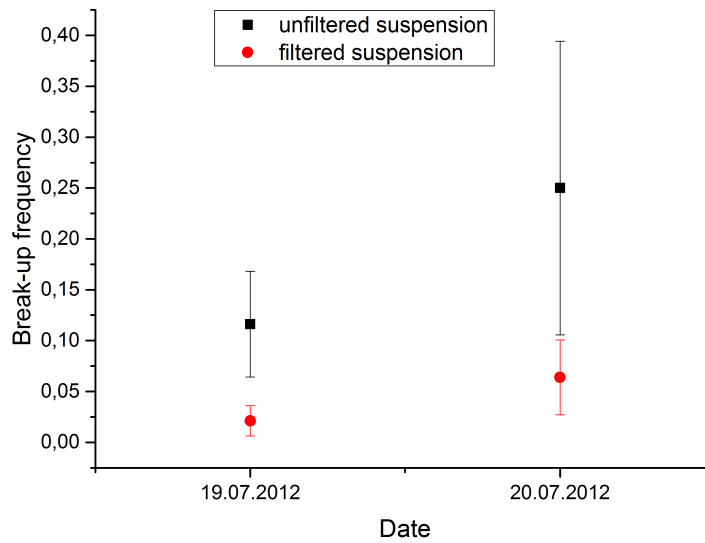


Figure 4.13: Fragmentation frequencies of filtered and unfiltered 400nm PSL suspensions at -14°C .

A second experiment with a solvent consisted of injecting droplets of sodium chloride solution (12,98 g/l) droplets into the EDB. Measurement results are listed in table 4.4. The droplets containing sodium chloride froze to more opaque ice, sometimes with visible pockets of brine in the droplet volume.

T [$^{\circ}\text{C}$]	Frozen droplets	Number of fragmentations
-26,05	50	0
-23,14	50	0
-20,27	51	0
-17,47	50	0
-14,78	50	0
-12,27	50	0
-10,00	50	1
-8,15	50	0
-6,87	23	0

Table 4.4: Fragmentation occurrence in experiments with sodium chlorite solution (12,98 g/l) droplets. The only fragmentation occurred at -10°C which results in a fragmentation frequency of 2% \pm 2%.

Next, the effect of low particle concentrations was investigated. A suspension of 180

particles/droplet of 28nm polystyrene spheres was further diluted until only a fraction of droplets was expected to contain any particles. For the dilutions, a sample (0,1 to 1,0ml) was taken from a higher concentrated suspension of 10ml volume. This sample was then filled up with nanopure water to 10ml. Each step was conducted with a fresh pipette tip to prevent particle contamination. Between experiments with dilutions the injector was rinsed and filled with nanopure water. Each time nanopure water was tested for break-ups (50 freezing experiments), none occurred. The measured break-up frequencies at -23°C are depicted in figure 4.14.

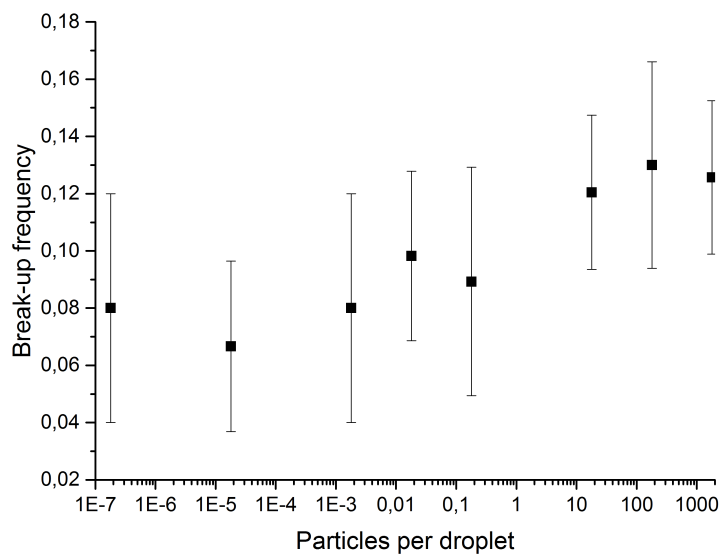


Figure 4.14: Break-up frequency in dependence from nominal PSL particle number ($d=28\text{nm}$) per droplet ($d=85\mu\text{m}$) at -23°C . Error bars represent standard deviations.

4.3.4 Rainwater experiments

The experiments with PSL suspensions could be understood as model experiments of ice nucleation in cloud droplets in the contact mode. To investigate fragmentations in immersion freezing, an IN was needed that would nucleate ice in the temperature range of -28°C to -8°C where most of the break-ups had taken place during the PSL experiments. A quantitative experiment with rainwater collected in a petri dish in one afternoon in June 2011 (and experimented with on the same afternoon) showed rainwater to be inappropriate to this end. It nucleated ice only weakly above -30°C , most droplets did not freeze within 30 seconds in the EDB. The results of these immersion freezing experiments are presented in table 4.5.

T [°C]	Frozen droplets	Unfrozen droplets	Fragmentations
-23,13	0	20	0
-28,01	1	10	0
-29,98	3	23	0
-31,96	24	0	0

Table 4.5: Results of immersion freezing experiments with rainwater droplets in the EDB with regards to fragmentations.

4.3.5 SNOMAX suspension experiments

As the contents of rainwater were not suitable IN above -28°C , another particle to be suspended was necessary for higher temperatures. Bioaerosols are among the best known IN (see chapter 1.5.2). One specific bacterium, *Pseudomonas syringae*, is commonly used as an ice nucleus in freezing experiments. Due to highly ice-active proteins on its outside, cell fragments of *P.syringae* are employed as a freezing agent in snow cannons at ski pistes. Those cell fragments are commercially available under the name SNOMAX (see www.snomax.ch). Droplets containing 150mg/l of SNOMAX (the producer recommends 0,5g SNOMAX per 1000 l of water for use in snow lances) were injected into the EDB and their freezing behavior was observed. This high concentration was chosen to ensure ice nucleation within 30 seconds in the EDB and caused visible turbidity with a yellow-greenish tint. The results are listed in table 4.6.

T [°C]	Number of freezing experiments	Fragmentations
-12,11	50	0
-12,83	50	0
-16,13	50	0
-17,62	50	0
-20,09	15	0
-20,93	12	0

Table 4.6: Results of immersion freezing experiments with 150 mg/l SNOMAX particles with regard to fragmentations. Temperature as measured at the EDB, as no air flows were activated during the experiments.

During all these experiments, no fragmentations occurred. It was reasoned that the SNOMAX particles might be compressible or fragile under the pressures in the expanding ice shell of the droplet and thus be unsuited to induce fragmentations. To verify this

theory, experiments with a suspension of both PSL ($d=400\text{nm}$) and SNOMAX particles were conducted. The results are listed in table 4.7.

T [°C]	Number of freezing experiments	Fragmentations
-11,03	56	0
-17,46	100	0
-21,18	100	0
-25,28	108	0

Table 4.7: Results of immersion freezing experiments with 150 mg/l SNOMAX and 1000 PSL particles per droplet ($d=85\mu\text{m}$). Droplet temperature as measured at the EDB, as no air flows were activated during the experiments.

Again, no fragmentations occurred. For the following experiments, a new approach was chosen: an aerosol system was added to the experimental setup.

4.3.6 Aerosol experiments

An aerosol system (see chapter 3.2) was installed on the EDB to lead an aerosol stream of defined particle size distribution and number concentration by a nanopure droplet. The goal was to investigate the effect of aerosol particles on the droplet surface on fragmentation frequency.

Three measurement series were conducted with the particles detailed in table 4.8. Once the droplets had collected particles for 30 seconds, the aerosol stream was switched to a stream of ice particles to nucleate freezing in the droplet.

Aerosol	Diameter [nm]	Calculated particle number per droplet
SNOMAX	322	3 ± 3
PSL	100	140 ± 100
Hematite	300	5 ± 5

Table 4.8: Aerosol contact experiment particles.

The results of the aerosol experiments with regards to the fragmentation frequency are depicted in figure 4.15.

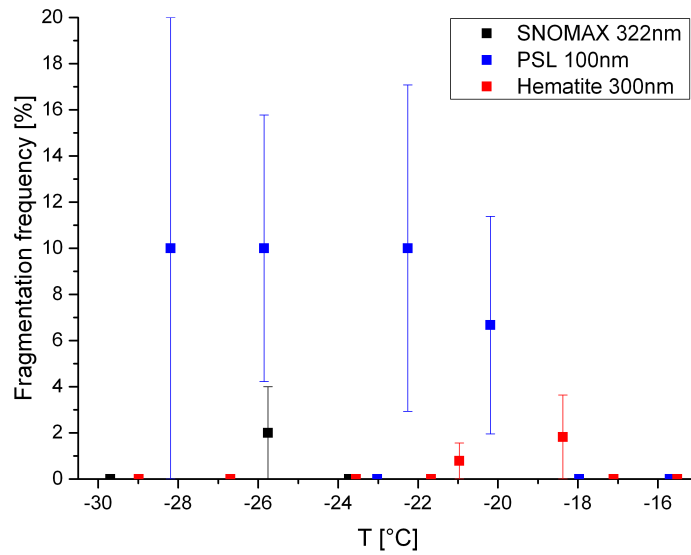


Figure 4.15: Fragmentation frequencies of freezing droplets having collected particles (see table 4.8 for details). Error bars represent standard deviations.

4.3.7 Quantitative description of fragmentations

A fragmentation can be quantified apart from the basic occurrence:

Separation speed of fragments This speed may give information about the energy of the process and thus about the possible causes.

Completeness of the fragmentation It may occur that a freezing droplet breaks up only partially or that the fragments remain in contact after their original connection is separated.

4.3.7.1 Separation speed of fragments

The high time resolution of the camera allowed for an analysis of the kinetics of fragmentations as laid out in chapter 3.4.2.2. The measured speeds and energies are depicted in figure 4.16.

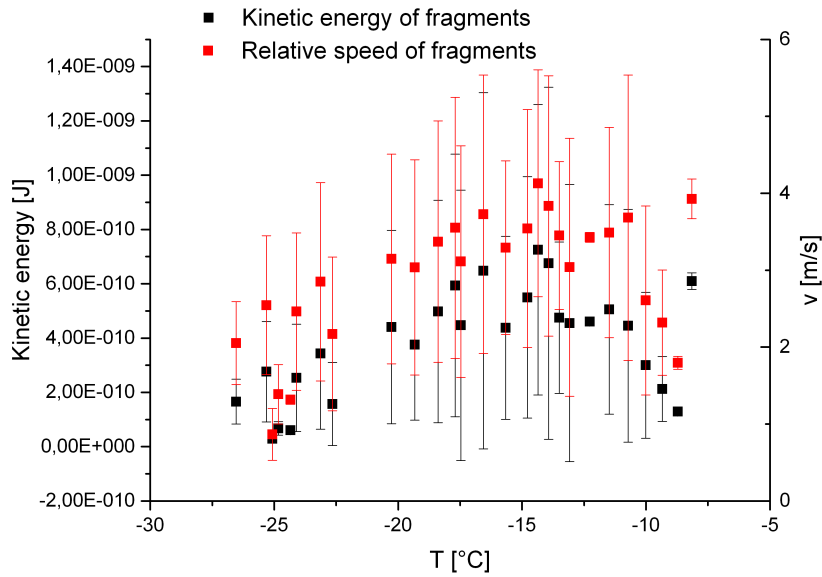
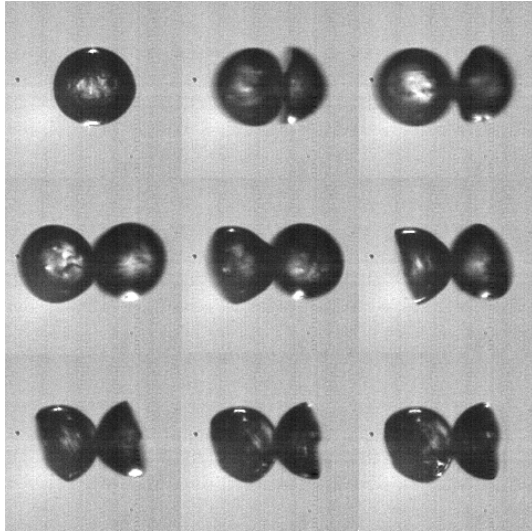


Figure 4.16: Kinetic energies and relative speeds of fragments, after break-up, over temperature. Error bars represent standard deviations, except in the data points at $-25,1^{\circ}\text{C}$, $-24,3^{\circ}\text{C}$, $-8,7^{\circ}\text{C}$ and $-8,2^{\circ}\text{C}$ where the error has been estimated from measurement uncertainties. Values calculated from data also evaluated in [96].

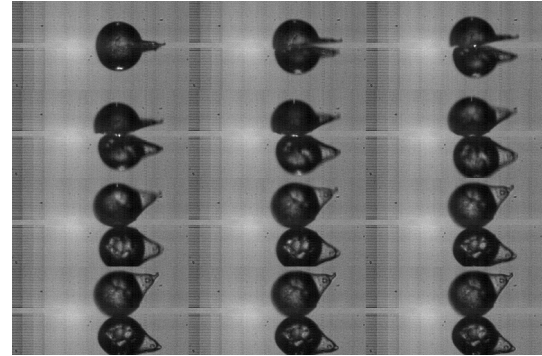
In a few cases, high rotational frequencies were noticed in the fragments. The four fastest frequencies observed were in the range of 2000Hz-9000Hz, which translated to rotational energies of $0,37 \cdot 10^{-10}\text{J}$ - $1,84 \cdot 10^{-10}\text{J}$.

4.3.7.2 Completeness of fragmentation

Incomplete fragmentations may not immediately result in ice multiplication but can still give information about the properties of water and ice close to 0°C . As the thermal conduction between the ice and the liquid fraction of a fragment is much better than to the ambient atmosphere, the temperature of two fragments sliding or rolling on each other is close to 0°C . As such, the rolling or sliding resistance of ice on ice at the freezing point might be calculated by evaluation of incomplete fragmentations as in figure 4.17, but the occurrence of suitable recordings is too rare (only four in several thousands of experiments) for statistically reliable evaluation. Incomplete fragmentations were disregarded for the measurements of break-up frequencies, as no visible ice multiplication had taken place.



(a) Droplet ($d \approx 85 \mu\text{m}$) containing ≈ 1800 PSL particles ($d = 28 \text{nm}$), ambient temperature of -23°C . Time steps from top left to bottom right: first to second frame $40 \mu\text{s}$, $20 \mu\text{s}$ in all other cases.



(b) Droplet ($d \approx 85 \mu\text{m}$) containing ≈ 1800 PSL particles ($d = 28 \text{nm}$), ambient temperature of -18°C . From top left to bottom right: $t = 0 \mu\text{s}$; $14 \mu\text{s}$; $29 \mu\text{s}$; $43 \mu\text{s}$; $57 \mu\text{s}$; $71 \mu\text{s}$; $86 \mu\text{s}$; $100 \mu\text{s}$; $114 \mu\text{s}$; $157 \mu\text{s}$; $186 \mu\text{s}$; $229 \mu\text{s}$.

Figure 4.17: Incomplete fragmentations with subsequent rolling of two ice hemispheres on each other.

4.4 Bubbles

Caused by the pressure from the core, a small crack may open in the shell through which water and dissolved gases may be pushed.

The water may form into spicules of ice; water on the rim of the crack freezes into a ring, while the water in the center of the ring remains liquid. The following water again freezes into the shape of a ring, so an ice needle ('spicule') with liquid water in the center grows from the droplet. Given sufficient pressure, the water in the ice needle remains liquid and this growth can lead to long protrusion from the droplet.

Dissolved gases from the core may cause bubbles to grow on the surface or on the tip of a spicule.

The occurrence of a bursting bubble was recognized as a potential ice multiplication process in experiments that were conducted in the search for fragmentations. Some of these bursting bubbles resulted in a strong recoil of the complete droplet. A closer inspection of such a recording suggested the separation (henceforth called 'shot') of the whole bubble from the droplet surface. If the bubble has been frozen at this point in time, an ice multiplication process took place. An example of a bubble that may lead

to ice multiplication is presented in figure 4.18.

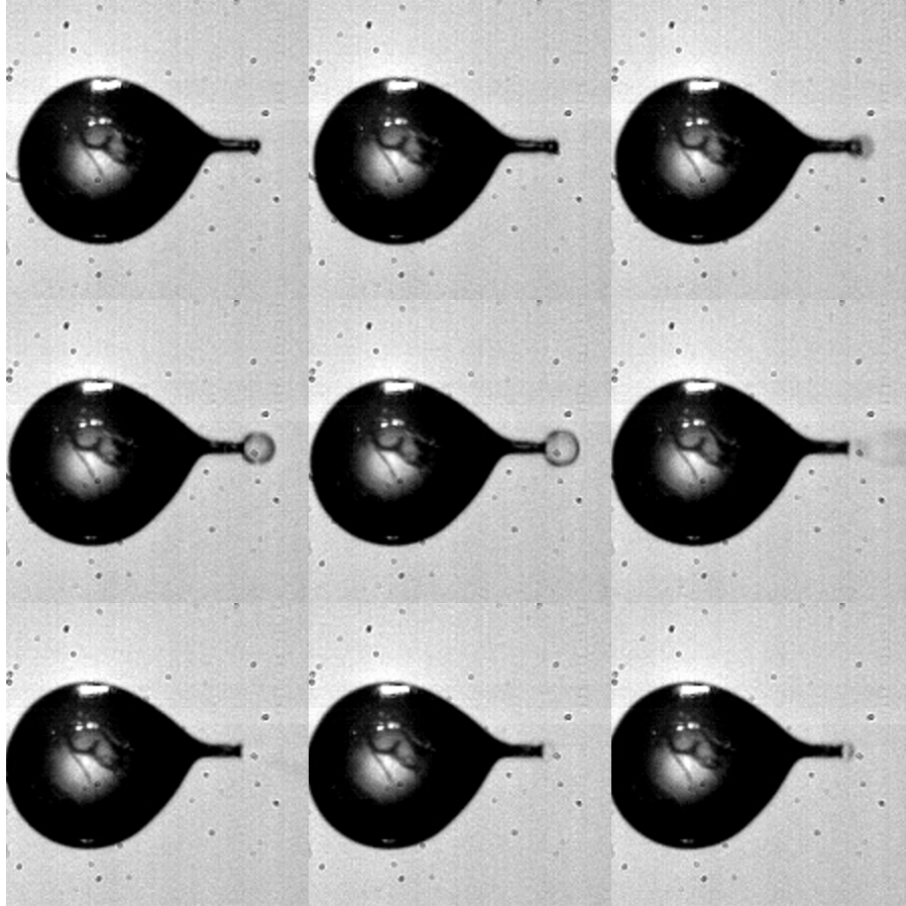


Figure 4.18: Droplet of $85\mu\text{m}$ diameter, containing nominally 180 PSL particles ($d=400\text{nm}$). $T=-11,6^\circ\text{C}$. Time between frames: $20\mu\text{s}$, except for first to second frame: $120\mu\text{s}$. In the last frame, a new bubble grows on the spicule.

For the following experiments, the argumentation is the same as for the fragmentation experiments with regard to the reasoning behind the experiments.

4.4.1 PSL suspension experiments

During the measurement series with PSL suspensions, bubbles and shots could be observed. The frequencies for experiments with 400nm particles are shown in figure 4.19.

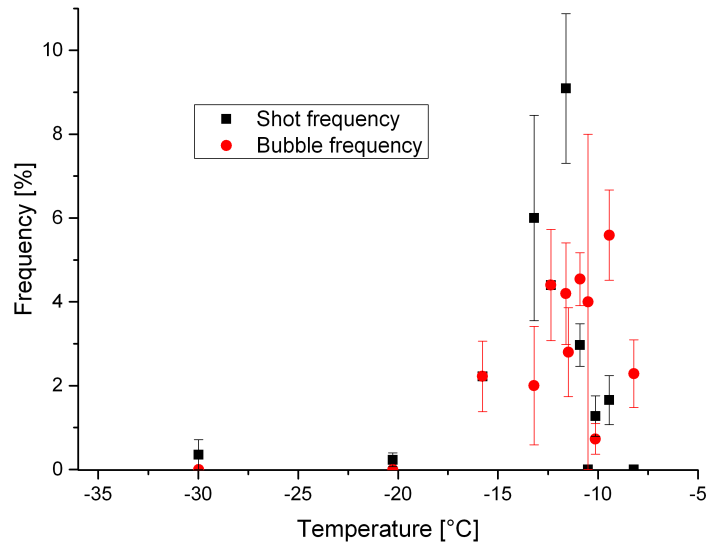


Figure 4.19: Frequency of bubbles and shots for PSL suspension ($d=400\text{nm}$) experiments, nominal number of 180-1800 particles per droplet. Experiments were conducted for all temperatures

For droplets containing PSL particles with 28nm diameter, much fewer bubbles and shots were observed during experimentation; the results of measurements on the bubble frequency by (Handmann 2014) are shown in table 5.3.

4.4.2 Kaolinite suspension experiments

Droplets of a kaolinite suspension (0,1g/l) of particle diameters $<10\mu\text{m}$ were injected into the EDB. The result with regards to the frequency of bubbles and shots is shown in table 4.9.

T [°C]	Frozen droplets	Bubbles	Bubble frequency
-20,3	127	1	$0,8\pm 0,8$
-22,63	202	0	0
-23,12	86	0	0
-24,02	179	1	$0,56\pm 0,56$
-26,94	32	0	0

Table 4.9: Results of experiments with droplets containing 0,01g/l kaolinite with regards to bubbles and shots. Errors denote standard deviations.

4.4.3 Rainwater experiments

Rainwater (collected in June 2011 and experimented with on the same day) was injected into the EDB and its freezing behavior was observed. The results with regards to bubbles are shown in table 4.10.

T [°C]	Frozen droplets	Unfrozen droplets	Bubbles
-23,13	0	20	0
-28,01	1	10	0
-29,98	3	23	0
-31,96	24	0	1

Table 4.10: Results of immersion freezing experiments with rainwater droplets in the EDB with regards to bubbles.

4.4.4 SNOMAX suspension experiments

The frequency of bubbles and shots was measured in droplets containing 150mg/l SNO-MAX particles and is presented in table 4.11.

T [°C]	Number of freezing experiments	Bubbles and Shots
-12,11	50	0
-12,83	50	0
-16,13	50	0
-17,62	50	0
-20,09	15	0
-20,93	12	0

Table 4.11: Results of immersion freezing experiments with 150 mg/l SNOMAX particles with regard to bubbles and shots. Temperature as measured at the EDB, as no air flows were activated during the experiments.

During the second series, SNOMAX as well as PSL particles ($d=400\text{nm}$) were suspended in droplets injected into the EDB. The results are listed in table .

T [°C]	Number of freezing experiments	Bubbles	Bubble frequency [%]
-11,03	56	1	1,8±1,8
-17,46	100	0	0
-21,18	100	17	17±4
-25,28	108	4	3,7±1,9

Table 4.12: Results of immersion freezing experiments with 150 mg/l SNOMAX and 1000 PSL particles per droplet ($d=85\mu\text{m}$). Temperature as measured at the EDB, as no air flows were activated during the experiments. Errors denote standard deviations.

4.4.5 Aerosol experiments

During aerosol experiments with hematite particles the occurrence of bubbles was observed. The measurement results are presented in figure 4.20.

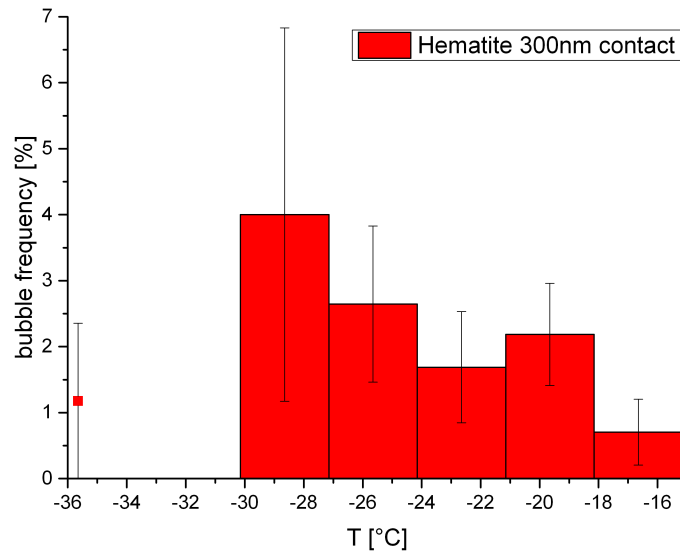


Figure 4.20: Bubble occurrence frequencies of freezing droplets having collected hematite particles (see table 4.8 for details). Due to the low numbers of bubble occurrences at individual temperatures, the data has been combined into bins of 3K size, except for the data point at $-35,65^{\circ}\text{C}$. Error bars represent standard deviations.

Chapter 5

Discussion

In this chapter, the results presented in the previous chapter are discussed.

The observations on droplet size manipulation are critically evaluated for their applicability under experimental conditions.

Consecutively, the results of fragmentation and bubble experiments are discussed with attention to the materials different from water that were present in or on the droplets during the experiments.

A possible link of fragmentations and bubbles to another ice multiplication mechanism, the Hallett-Mossop process, is explored.

The chapter ends with a critical review of the measurement results in comparison to the literature.

5.1 Droplet size manipulation

5.1.1 Single pulse variation

Over a certain voltage (in these experiments, it was 50V), smaller droplets could be generated with longer pulse widths (see figure 4.1b). The voltage may vary from injector to injector, especially since new injectors tend to be operative at lower voltages than old ones. A reduction to $80\mu\text{m}/90\mu\text{m} \approx 89\%$ in diameter was achieved, with a reference diameter d_{ref} of $90\mu\text{m}$ for this and the following experiments.

Single droplet pulse is not recommended for droplet size variation as it relies too heavily on employing higher amplitudes which generally means faster droplets. This may impede droplet capture in the EDB.

5.1.2 Double pulse variation

For a double pulse actuation signal (figure 4.2a), a droplet size reduction to $75\mu\text{m}/90\mu\text{m} \approx 83\%$ could be achieved (see figure 4.2). A further reduction by setting the second pulse height to 75% of the first one was not observed.

In both experiment series, the droplet size showed a linear behavior with interval length t_i between the minimal interval length $t_{i,min}$, below which reliable droplet generation was not possible, and a maximal interval length $t_{i,max}$ beyond which the reference diameter was produced. This means that for $t_i \in [t_{i,min}; t_{i,max}]$, the droplet diameter should be continuously variable between the minimal droplet size fraction δ to 100% droplet size via

$$d(t_i) = \delta * d_{ref} + \frac{(1-\delta)d_{ref}}{t_{i,max}-t_{i,min}} t_i = 70\mu\text{m} + t_i * 0,57 \frac{\mu\text{m}}{\mu\text{s}}$$

for the presented results.

Therefore double pulse variation offers a reliable way of limited droplet size variation.

5.1.3 W-shape pulse variation

A droplet size reduction to $57,5\mu\text{m}/90\mu\text{m} \approx 64\%$ was measured with a suitable W-shape pulse signal (figure 4.3a) actuation. For the longest interval ($t_i = 260\mu\text{s}$) between the W-shape and the single afterpulse, the droplet was $\approx 9\mu\text{m}$ larger than for shorter interval times. For interval lengths between $200\mu\text{s}$ - $240\mu\text{s}$, the droplet sizes were the same in the range of errors.

The W-shape signal has the disadvantage of polarity change which can not be easily realized in the power source employed in this experiment. The result may be interesting in the field of injector research in general but is of limited use for further experiments at the experimental setup described in this thesis.

5.1.4 Triple pulse variation

The measurements with triple pulse actuation (figure 4.4) showed the most versatile droplet size variation. Both droplet enlargement to $105\mu\text{m}/90\mu\text{m} \approx 117\%$ (figure 4.4b) reference size and reduction to $60\mu\text{m}/90\mu\text{m} \approx 67\%$ (figure 4.4d) reference size were achieved.

In contrast to the results of double pulse actuation (discussed in chapter 5.1.2), the size could not be varied continuously across the whole range. Instead, there were two droplet size modes separated by a size gap: a mode of smaller droplets ($60\mu\text{m}$ - $80\mu\text{m}$) and a mode of larger droplet around $105\mu\text{m}$.

The data for large droplets are too closely grouped to see a trend with pulse widths. For the smaller mode, a trend for smaller droplets with shorter second pulse lengths is visible, but only for longer first interval lengths ($t_{i,1} \geq 100\mu\text{s}$).

Generally speaking, the following effects of pulse variations on droplet size were found: shorter first and second pulses (figures 4.4b, and 4.4c), longer third pulses (figure 4.4d) and shorter intervals (figure 4.4b) lead to larger droplets, while the opposite is true for smaller droplets.

5.1.5 Pulse combinations in the EDB

The measurement series on droplet was completed by measurements under working conditions at the EDB, which meant that it was cooled down to a typical experimental temperature (-18°C). The results in figure 4.5b show the effect of several pulse shapes on droplet size; droplets in the range of $d=(61 \pm 16)\mu\text{m} = 61\mu\text{m} \pm 26\%$ with a reference size of $64\mu\text{m}$ for single pulse actuation could be generated.

For the experiments at the EDB, no temperature control was included in the heating mechanism of the injector's reservoir, so the size difference of droplets to the previous experiments is most likely caused by rapid droplet evaporation before capture. This leads to the conclusion that temperature control of the reservoir might offer an easy alternative to pulse shape variation. ¹The limits lie in the temperature durability of the injector and the liquid that is injected into the EDB.

Triple pulse signals were found to be just as suitable for droplet size reduction as a W-shape signal was, but with the advantage of consisting only of pulses of the same polarity and the possibility of creating larger droplets as well.

At the IMK-AAF, Jens Nadolny modified the droplet capture and storage program of the EDB experiments to include the possibility for multiple pulse actuation with variable interval lengths and pulse widths.

5.2 Ice propagation speed in a droplet

5.2.1 Growth modi

The distinction between dendritic growth, frontal growth and "zigzag" growth was justified by their optical appearance in the droplet.

¹Jens Nadolny at the IMK-AAF has since written a program with which the temperature of the heating element can be controlled.

It may be argued that the distinction between planar and dendritic growth is only based on the orientation of the ice crystal growing in the droplet: a number of closely spaced side branches of a dendrite might be conceived as planar growth if they all propagate with the same speed through supercooled water, or a front of ice may appear as a needle if its orientation happened to be perpendicular to the plane of observation.

A previous investigation into the morphology of ice in supercooled water by [125] showed that, depending on temperature, different growth types are prevalent. They claimed that at 12-21K supercooling, the fastest growth occurs in the shape of platelets with a growth rate of the ice grain tip of $v = 0,18 * 10^{-3} \Delta T^2 m/s$, and that branched, dendritic or needle- like structures from 0,1-16 K supercooling propagate with $v = 0,5 * 10^{-3} \Delta T^{1,2}$. This has not been found in the experiments of this thesis: in the range of their errors, the propagation speeds of dendritically and frontally growing ice crystals are the same (see figures 4.7b and 4.9).

It is noteworthy that the experiments of [125] were conducted on a much larger lengthscale of at least several mm, as have most other experiments that observed ice propagation in supercooled water. It has been documented by [128] that the size of a crystal may influence the further growth stability with regards to shape, so a comparison to other studies about the shape of the crystals may be difficult.

For “zigzag” growth, a tendency for roughly two times longer first freezing steps in comparison to dendritic growth and planar growth (figure 4.7b) was measured. It seems unlikely that this ice propagation occurred on the surface and not through the bulk of the droplet because this would require a curvature in the growing crystal, although it would account for a longer freezing step time: the path around a droplet is by a factor of π longer than through a droplet. The explanation is more likely rooted in the shape of growing ice in general. For a given ice crystal in supercooled water, two of three spatial directions relative to the crystal orientation exhibit faster growth than the third one (see [84]). It may be assumed that the needle-like ice growth in figure 4.8 is actually an ice crystal growing in a plane perpendicular to the plane of observation; so, once this crystal meets the water-air boundary, further growth can temporarily only occur in the slower direction. As soon as ice has propagated in the slow growth direction slightly above or below this plane of ice, fast propagation can take over again with a tilt relative to the first plane because of the stronger temperature gradient at a certain distance to the previously frozen water.

5.2.2 Ice propagation speed in supercooled water in the literature

As depicted in figure 4.10, there may be a slight effect of particulate matter on ice propagation speed in supercooled water, at least for the measurements at -30°C ; for warmer temperatures, the differential first freezing speeds in nanopure water droplets coincide with the differential first freezing speeds in water droplets containing PSL particles. For this reason, only pure water droplets were evaluated for ice propagation speed.

The comparison of differential first freezing speeds and the ratio of droplet diameter to the first freezing time in figure 4.11 yields an interesting result: for temperatures below $\approx -15^{\circ}\text{C}$, the two measurement series coincide very well in the range of their errors, and only for stronger supercoolings of the droplets differences appear, with the differential speeds being higher. Still, for comparison with ice propagation speed values found in literature (see table 5.1), the differential speed parameterization is being employed. In [87], no fit of the shape $v = a * \Delta T^b$ is given, but their measurements increased the range of supercoolings at which the propagation speed of ice in supercooled water was measured.

Investigator	Supercooling range ΔT [K]	b	Comment
This thesis	8-36	$1,83 \pm 0,14$	
[51]	0,1-1	1,69	
[42]	0,1-20	1,9	
[84]	2,5-7,5	3,7	
[111]	0,1-9	2,22	
	12-18	1	
[58]	0,1-1	2,17	
[101]	0,5-8,5	2	
[83]	5-24	2,05	
[125]	0,1-16	1,2	Needle shaped ice growth
	12-21	2	Plate shaped ice growth
[87]	28 - 38		0,245 - 0,47 m/s

Table 5.1: Comparison of ice propagation speed from the presented experiments with literature values for the exponent b in $v = a * \Delta T^b$.

Their measurements are, in the range of errors, consistent with the fit to the data in this thesis. The measured exponent in $v = a * \Delta T^b$ is slightly lower than most previous measurements (see table 5.1). This may be linked to the fact that the supercoolings of this thesis' measurements exceeded the previous experiments by a several degrees on the one hand and to the upper temperature limit on the other: due to evaporative cooling, no measurements were made above -5°C . For a complete formula for the propagation speed of ice in supercooled water, these measurements would be necessary, especially if the fact is considered that the highest exponents in literature were fitted to measurements that covered higher temperatures. Observations at warm droplet temperatures close to 0°C could be realized by adding water vapor to the air and aerosol stream, but that would mean that ice would grow in the EDB which would limit the experimentation time before the EDB would have to be defrosted.

It actually has been observed that the air flow that passes through the flow controller decreases over time, especially at cold temperatures, which is caused by ice in the air ducts through the EDB electrodes (see figure 3.1a). This situation would be exacerbated by adding even more water vapor to the flow, but at warm temperatures, the experimentation time might be sufficient for first freezing speed measurements.

For the aerosol flow, adding water vapor might lead to droplet nucleation. If the point of aerosol experiments is to investigate aerosols in contact with the droplet surface, the amount of water would have to be well-controlled to prevent droplet nucleation; but it might be useful to have a calculable number of droplets, each containing one aerosol particle, to impinge on a droplet. With ice-active aerosols, the position of particles immersed in a droplet might be learned from observing the point of ice nucleation. Having droplets containing particles hit a larger droplet might also lead to immersion freezing measurements with a lower level of uncertainty of particle surface. But climate chamber experiments like the AIDA [89] or the upcoming AIDA-2 at the IMK-AAF are better suited for immersion freezing experiments due to the large number of droplets that can be observed at the same time for statistically reliable statements.

5.3 Fragmentations

5.3.1 The energy of fragments

One of the experimental boundary conditions is the electric charge that allows for droplet levitation and is generally not found in cloud droplets or ice particles outside of severe lightning storms. It is thus necessary to compare the potential energy E_{el} that derives

from charge repulsion to the kinetic and rotational energies of a fragmenting freezing droplet to estimate the atmospheric relevance of break-ups. A simple approximation is given by two charges of half the droplet's total charge q in a distance of half a droplet diameter d , which is given by $E_{el} = \frac{1}{8\pi\epsilon\epsilon_0} \frac{(q/2)^2}{d}$ with the vacuum permittivity ϵ_0 and the assumption of a permittivity $\epsilon = 1$ for air. For a typical charge of $q = 15Me^- = 2,4 * 10^{-12}C$ and $d = 80\mu m$, the potential electric energy amounts to $E_{el} = 7,6 * 10^{-11}J$. The typical kinetic energy of a fragmenting droplet was in the order of $E_{kin} = 4 * 10^{-10}J$ (see 4.16), the largest rotational energies measured were in the order of $E_{rot} = 1,84 * 10^{-10}J$ at fragment rotations of up to 9000Hz. This discrepancy in energies leads to the conclusion that the influence of the electric charge on the droplet is of minor, if any, importance to the fragmentation process.

5.3.2 PSL suspension experiments

The largest number of experiments was conducted with droplets containing PSL particles of two diameters (28nm and 400nm) at nominal particle concentrations per droplet (calculated for a diameter of 85 μm) ranging from 3,6 to 1800. Freezing was caused by ice crystals impinging onto the droplet surface, so contact nucleation took place. It may be argued that the mode of nucleation is of no consequence to the occurrence of fragmentations; the process that is identified to be the cause, that is, the pressure build up in a liquid core surrounded by an ice shell, is independent of the way ice is nucleated in the first freezing step. Once an ice shell has grown around the spongy ice-water mixture in the core, pressure rises and the ice in the core is melted (see equation 2.11). So, any structural differences that might have existed between ice nucleated by contact freezing or immersion freezing are expected to have vanished at the point in the freezing process when fragmentations take place, at least if the bulk volume of the droplet is considered.

In figure 4.12, it is noticeable that the particle numbers per droplet seem to be of no effect on the fragmentation frequency in the range of the standard deviations of the measurements for each particle size. The conclusion is that there is a saturation number of particles in a droplet beyond which the frequency of fragmentations stays constant. In this sense, the measured values represent the upper limit of ice multiplication by fragmentation for the given droplet size and particles in the droplet.

It is reasonable to assume that fragmentations occur with comparable frequencies for particle sizes between 28nm and 400nm. The theory brought forward in this thesis is that the particles function as lattice defects in the ice at which cracks can nucleate once the pressure from the core is high enough, and neither is a particle diameter of 28nm

the lower limit nor is a particle diameter of 400nm the upper limit.

A close look at figure 4.12 reveals several data points (e.g., at -15°C) which show a much lower fragmentation frequency than data points in adjacent temperature intervals. The reason for this probably lies in an experimental boundary condition: in long experiment series exceeding 45 minutes with the same injector, fragmentation frequency reduced over time until no more fragmentations could be observed, no matter the frequency at the beginning of a measurement series. This can be attributed to a time-dependent depletion of particles caused by sedimentation and Brownian motion in the injector. In experiments after the effect of reduced fragmentation over time was recognized, the experimental time was reduced to a maximum of 30 minutes.

5.3.3 Kaolinite suspension experiments

In experiments with suspensions of the clay mineral kaolinite at sizes smaller than $10\mu\text{m}$ fragmentations were observed. The measured fragmentation frequencies were lower than in PSL experiments at the same temperatures except for the measurements at $-26,94^{\circ}\text{C}$. The small number of experiments (4 fragmentations in 32 freezing experiments) leads to an error of 50% on the frequency, though. Notably, there were no fragmentations at $-22,63^{\circ}\text{C}$ and $-23,12^{\circ}\text{C}$, but at temperatures both higher and lower. Assuming the same effects at work as in the experiments with PSL particles, one would not expect a complete suppression of fragmentation between two temperatures at which break-ups occurred. The lack of ice multiplication at these two temperatures may be explained with sedimentation in the liquid reservoir of the injector or in the injector itself; the specific weight of kaolinite is 2,63 times higher than of water, so it has a considerable terminal falling velocity which leads to a depletion of kaolinite in the injector and consequently the droplets. Assuming a reservoir thickness of $500\mu\text{m}$, kaolinite spheres larger than $1\mu\text{m}$ sediment out in less than 6 minutes; platelets of $100\mu\text{m}$ would need more than nine and a half hours for the whole distance, though, so it may be assumed that aggregation of smaller particles to clusters or onto larger particles has taken place. This is quite common for clay minerals and can be seen under an environmental scanning electron microscope (figure 3.3d).

While it is interesting to see fragmentations in droplets containing atmospherically relevant particles, the rough classification of size distribution and consequently particle number per droplet allows for little more than the qualitative confirmation of the fragmentations.

5.3.4 Dilution and solution experiments

The effects of solutes on the occurrence of fragmentations has been investigated.

In the first experiment, a PSL solution of 400nm particles has been filtered through a cellulose acetat filter with a filter size of nominally 200nm, so all particles were expected to be removed after the solution has passed the filter. The measurements show a reduction in fragmentation frequency by a factor of ≈ 5 (see figure 4.13). If dissolved materials in the suspension aside from PSL were the sole cause of fragmentations, no reduction in break-up occurrence would have been found. If, on the other hand, only the presence of particles in a droplet are expected to promote fragmentation, there should be no fragmentations whatsoever in suspensions filtered for particles. It may thus be possible that the combination of particles and solutes is the answer to the question what causes fragmentations. It seems more likely, though, that the filter used is not completely effective at removing particles of double the nominal filtering size. This conclusion will have to be considered in future experiments with filtered suspensions.

A second experiment for the influence of solutes was conducted with a sodium chloride solution of 12,98g/l, which is roughly comparable with sea water (which contains ≈ 30 g/l). During several hundred experiments across temperatures at which fragmentations had been observed in PSL solutions (see table 4.4), only one droplet break-up at -8°C was observed. For the number of conducted experiments, this would lead to a fragmentation frequency of 2% +/- 2%. As in all experiments in the EDB, a particle contamination in the droplet could not be excluded with certainty, so the fragmentation might be influenced by a random particle. But even if only water and sodium chloride were present in the droplet at the moment of fragmentation, the frequency is still much lower than with particles present during experiments with PSL suspensions. The observed higher opacity and brine pockets in the frozen droplet point to a more porous structure which should reduce the probability of a fragmentation because of the reduced stability of the ice shell. The process of fragmentation is based on a stable ice shell up to the point when a failure at one point in the material leads to crack propagation on the scale of the whole droplet; if material failure occurs locally before the tensile stresses are sufficient for fracture in adjacent volume elements, or a pocket of brine is reached, crack propagation stops and fragmentation does not occur. The gradual failure of such weak spots are likely to prevent pressure build-up to a level at which the whole shell breaks.

These deliberations are supported by [91], in which the “addition of ammonia is thought to weaken the ice structure, thus allowing pressure to be relieved by deformation or cracking without ejection of splinters”. [14, 86] found similar results with sodium chloride solutions (see chapter 5.6).

The measurements of fragmentation frequencies in droplets containing polystyrene spheres suggested that the number of particles in the droplet has no influence beyond a certain point. To appraise this thesis, a dilution experiment was conducted up to a point at which nominally one in a million droplets would be expected to contain a particle. The results (see figure 4.14) showed a slight trend of reduction of fragmentation frequency the thinner solutions became, but the ranges of errors would also allow for all measurements to yield a constant break-up frequency of $\approx 10\%$. An explanation may be found in an effect which reduces the efficiency of the dilution process, meaning more particles are carried over during a dilution than expected from the ration of the sample and the bulk mixing volume. One of these effects may lie in the behavior of PSL particles at a water-air boundary. As laid out in chapter 2.2.3, particles smaller than $5\mu\text{m}$ have a tendency to remain at the boundary, even if they are wettable and have specific weights considerably higher than those of water. At the moment a pipette passes through the water surface in a container of solution, a fraction of this surface and consequently of the particles is entrained into the pipette, so the actual concentration of particles after a dilution may be higher than calculated from the ratios of sample volume and new bulk mixing volume. A second possibility lies in the shelf life of polystyrene particles: they may deteriorate in time and break down into smaller particles, and the surfactants in the suspension used to keep the polystyrene spheres from coagulating may aggregate on those fragments or form new particles by themselves. This interpretation leads to the question of how small particles in a droplet can be before fragmentation no longer occurs; the particles were only 28nm of diameter to begin with which is only about two orders of magnitude larger than a water molecule.

So, the problem of the critical number of particles in a droplet to cause fragmentation is unsolved, especially with regards to the question if a single particle might be sufficient for a break-up.

5.3.5 SNOMAX suspension experiments

While the experiments with rainwater in the EDB (table 4.5) did not show fragmentations, the measurements illustrated the scarcity of ice nuclei in atmospheric aerosols. Only at $-31,96^\circ\text{C}$, all droplets ($d=80\mu\text{m}$) froze through nucleation by immersed particles, which includes particles collected during the precipitation from the lower troposphere.

The experiment series with SNOMAX suspensions led to a surprising result. With 150 mg/l , heterogeneous ice nucleation in each droplet occurred within 30 seconds, but no fragmentations were observed (see table 4.6). The same was true for immersion

freezing experiments with droplets containing both 150 mg/l SNOMAX and ≈ 1000 PSL ($d=400$ nm) particles.

These results may be linked to the considerations concerning sodium chloride freezing experiments. The high concentration of SNOMAX was chosen to ensure heterogeneous ice nucleation in all droplets within 30 seconds; for e.g., 75 mg/l SNOMAX, this was not the case. While the high concentration allowed for reliable freezing nucleation, there was the downside of solubles in the droplet that may have had a weakening effect on the ice shell, so fragmentation was suppressed. The same argumentation can be applied to droplets that also contained PSL particles.

5.3.6 Aerosol experiments

After expanding the experimental setup with an SMPS system (see chapter 3.2), particles (see projected particle number per droplet in table 4.8) were collected on the droplet for 30 seconds before freezing was nucleated with ice particles. The results are presented in figure 4.15 for the three aerosols involved. The first noticeable fact is the occurrence of fragmentations. Following the theoretical considerations in chapter 2.2.3, particles collected by the droplet should remain on its surface. This is reflected in the submersion depths of aerosols given in table 5.2.

Aerosol	diameter [nm]	θ_c [°]	submersion depth [nm]	source for θ_c
PSL	145	86	67	[144]
Hematite	300	47	48	[123]

Table 5.2: Contact angles θ_c and submersion depths of the aerosols employed in this thesis, calculated with equation 2.35.

This means that the minimal lattice defect caused by the particle fraction that is submersed is sufficient to facilitate crack nucleation during freezing and promote fragmentation.

Within their error bars, the fragmentation frequencies for aerosoluted PSL particles coincide with the measurements of immersed PSL particles (see figure 4.12), but there were also measurement points at $-22,7^\circ\text{C}$, $-18,4^\circ\text{C}$ and $-16,6^\circ\text{C}$ where no fragmentations were observed. The most likely explanation lies in the number of particles collected. The deviations in particles collected per droplet from the expectancy value are 71%, so it is well possible that too few experiments were conducted at those temperatures as to observe fragmentations with a good probability. Still, in the range of errors, it seems

that 40-140 PSL particles on a droplet surface may cause fragmentation of the droplet during freezing.

Only few fragmentations were observed which led to low fragmentation frequencies in experiments with SNOMAX (one fragmentation at $-25,76^{\circ}\text{C}$, with an expected number of SNOMAX particles of 3 ± 3 on the droplet) and hematite particles (one fragmentation each at -21°C and at $-18,38^{\circ}\text{C}$, with an expected number of hematite particles of 5 ± 5 on the droplet). SNOMAX is used as an ice nucleus for snow cannons on ski pistes, but the aerosol did not nucleate ice in most experiments. The reason is that only $\approx 10\%$ of all particles of 300nm carry a protein group capable of ice nucleation at warm temperatures ($> 12^{\circ}\text{C}$).

It has been established that pure water droplets exhibit virtually no fragmentations in [103] across the temperature range investigated in this thesis, a fact that repeatedly has been used to examine the injector for residual particles between experiments with different suspensions. And while the statistical basis is small, the consequence of these aerosol measurements is that 1-6 particles (for SNOMAX) and 1-10 particles (for hematite) respectively on a droplet surface may be sufficient to cause fragmentation during freezing. This is of relevance for atmospheric conditions, as drizzle drops levitated in updrafts may collect entrained aerosols and small droplets, which each contain at least one aerosol particle unless they have nucleated onto pure salt particles.

5.4 Bubbles

5.4.1 On the phase of bubble fragments

Bursting bubbles are a phenomenon of global importance as sea spray aerosols contribute to the aerosol concentration in marine areas (for a review of the aerosol fluxes, see [23]). This contribution results from residuals of dried film and jet droplets.

In this thesis, bubbles growing on freezing water droplets were observed and their frequency was measured in dependence of temperature and particulate matter on and in the droplet. A detailed look into the properties these bubbles is to be found in [45] who worked at the same experimental setup.

As the focus of the experiments lay on ice multiplication processes, the question arises whether bursting bubbles produce ice or not.

5.4.1.1 The phase of shots

In the case of shots, meaning visible fragments of the bubble separating from the freezing droplet at high speeds, it seems clear that ice multiplication has taken place.

Previous measurements and theoretical calculations in the literature (laid out in chapter 2.1.3) give an insight into the mechanisms involved in droplet generation by bursting bubbles and the properties of these droplets.

Firstly, the retraction of the liquid bubble film after a hole has nucleated needs to occur; this has not been observed in the events called shots.

Secondly, the size of the fragment seems to be identical to the bubble itself, although the fast motion of the fragments blurred their image. Film droplets and jet droplets are much smaller than the bubble itself.

In addition to the insights from literature on bubbles, there is the observation that the bubble seems to keep its shape points after separation from the bubble. As an estimate for the time a free bubble would need to contract to a droplet, the bubble radius R can be divided by the Taylor-Culick speed $v_{T-C} = \sqrt{2\sigma/\rho h}$ for retracting films which leads to a time scale for the bubble contraction. Even for bubbles of 10 μm diameter and 3 μm thickness, which is well in excess of any bubbles observed for this thesis, this contraction time would be 2 μs which is much shorter than the time between two frames in the investigated recordings.

These arguments lead to the conclusion that shots consist of ice.

It is argued that a liquid bubble, inflated by dissolved gases pushed through a channel in the shell, freezes by contact with the ice shell on which it grew. Once enough dissolved gases get pushed through the channel, the ice breaks at its weakest point, which just at the foot of the bubble (established in [78]), and the ice bubble is propelled away by both gas pressure and electrostatic repulsion. The force on the frozen bubble caused by the gases from the core is by several orders of magnitude larger than the Coulomb repulsion, so this process is not limited to charged droplets.

5.4.1.2 The phase of bursting bubble fragments

If a bubble bursts before ice nucleation has taken place, only liquid, if any, droplets are ejected.

For small bubbles, it may be possible that shots take place without visible ejection of fragments or a recoil in the droplet. But as the recoil of a confirmed shot on the droplet has generally been noticeable, it seems doubtful if most bursting bubbles created secondary ice.

5.4.2 PSL suspension experiments

In the PSL suspension experiments with 400nm particles, both bubbles and shots were observed (see figure 4.19). The rate of shots is higher than the fragmentation frequency between -13°C and -8°C but is less at deeper temperatures. The frequency of bubbles is, in the range of their error bars, comparable to the frequency of shots. While it is dubious that ice multiplication takes place in bubbles, every shot represents a secondary ice particle if the argumentation in 5.4.1.1 is followed.

Handmann [45], having worked with the same experimental setup, reported the combined frequencies for droplets containing 28nm PSL particles as shown in table 5.3.

T[$^{\circ}\text{C}$]	Frozen droplets	Bubbles+shots	Bubble and shot frequency [%]
-9,9	105	0	0
-12,3	169	0	0
-13,7	160	1	$0,6\pm 0,6$
-15,6	99	1	1 ± 1
-18,3	273	1	$0,4\pm 0,4$
-20,9	100	0	0
-23	837	7	$0,8\pm 0,3$
-28,3	400	0	0

Table 5.3: Bubble and shot frequencies for droplets containing 28nm PSL particles as reported by [45]; errors represent standard deviations.

The combined frequencies of bubbles and shots in experiments with 28nm PSL particle suspension are much lower than for experiments with 400nm PSL particles. There is no obvious reason for this, as the fragmentation frequencies for the two particle diameters were comparable (see figure 4.12).

5.4.3 Kaolinite suspension experiments

Droplets containing 0,1 g/l kaolinite of diameters $<10\mu\text{m}$ exhibited few bubble events during the experiments specified conducted for this thesis and presented in table 4.9. It is noticeable that the only two observed cases of bubbles (at $-24,02^{\circ}\text{C}$ and $-20,3^{\circ}\text{C}$) were observed at temperatures at which fragmentations also took place (table 4.3), and the experiment series at the other temperature at which fragmentations were observed (4 fragmentations out of 32 freezing events) was rather small. But while it is tempting to look for a correlation between fragmentation and bubble frequencies, the number of

counted fragmentations and bubbles is too small to make reliable statements on this subject from the kaolinite suspension experiment series.

5.4.4 SNOMAX suspension experiments

For droplets containing 150mg/l SNOMAX particles, neither bubbles nor shots were observed in the temperature range from -12°C to -21°C (table 4.11). This might be attributed to a weakening effect of solubles on the ice shell, so no cracks form that reach from the liquid core to the atmosphere; pressure is relieved through internal cracks or deformations.

For droplets containing both 150mg/l SNOMAX particles and ≈ 1000 PSL ($d=400\text{nm}$) particles, this argument fails, as bubbles were observed with a frequency maximum of $17\pm 4\%$ at -21°C (table 4.12). Apparently, the weakening effect on the ice caused by solubles in the SNOMAX suspension can not prevent the occurrence of cracks from the core to the shell promoted by the presumed lattice defects caused by the PSL particles.

In comparison to the results regarding fragmentations discussed in chapter 5.3.5 there is a clear difference; while fragmentations were apparently suppressed by the SNOMAX suspension under the experimental conditions, bubbles were not. Following this argumentation, this means that bubbles require a less pronounced pressure build-up in the freezing water core.

5.4.5 Hematite aerosol experiments

Freezing droplets that had collected few ($\approx 1-10$) hematite particles from an aerosol stream exhibited bubbles (see figure 4.20). This result is just as remarkable as the occurrence of fragmentations discussed in chapter 5.3.6, as the particles are only submersed for a fraction of their diameter (table 5.2) - yet their presence promotes cracks in the droplet's ice shell. While there were no shots observed, and the occurrence of bubbles does not necessarily mean ice multiplication, this is certainly interesting from the point of material science. Again, this may mean that larger ($\approx 300\mu\text{m}$) droplets in updrafts may cause ice enhancement once they freeze.

5.4.6 Bubbles per bubble event

Handmann [45] reported that during each event in which bubbles or shots were observed, 2 - 6 bubbles or shots were counted. This means that "shot" events have the potential to be an effective ice multiplication mechanism and might mean ice multiplication if

bubbles produce ice. The probability of this happening in the atmosphere might be low, though, as the air pressure and consequently the gas concentration in freezing droplets decreases with height. Less gas in the droplet would probably also mean less bubbles and shots. For droplets below 3km altitude, though, the gas content is larger than 2/3 of the gas content at 1 atmosphere, so multiple shots and bubbles might still be possible.

5.5 A possible link to the Hallett-Mossop process

The observations in the droplet evaporation speeds showed a shift in the temperature measured at the EDB and the temperature in the droplet (see figure 3.7). All other measurements had to be calibrated for this effect, which led to a measurement gap for experiments with dry ice nucleations between -8°C and 0°C (figure 3.7a) for experiments with a low flow through the EDB (PSL suspensions nucleated with dry ice). For high flow experiments (PSL suspensions nucleated with SNOMAX particles size-selected with a classifier), this gap lay between -16°C and 0°C (figure 3.7b). In experiments where no flow was applied (SNOMAX, illite suspension immersion freezing experiments), the temperature shift was small (figure 3.7b).

While the temperature range in which fragmentations took place most frequently, that is between -22°C and -12°C , was generally covered experimentally, the lack of measurements at warmer temperatures is regrettable insofar as the Hallett-Mossop process, generally regarded to be the most effective ice multiplication process, is claimed to occur in the range of -8°C to -3°C (see figure 5.1).

In following experiments, it was found that “on average, one secondary ice crystal is produced for every 250 drops $\geq 24\mu\text{m}$ diameter accreted at a temperature $-5 \pm 0, 5^{\circ}\text{C}$.” [90]. “Later it was found that the cloud should also contain small drops $\lesssim 12\mu\text{m}$ diameter.” [92]. The Hallett-Mossop process does not take place in single droplets but is dependent on a small droplet impinging onto a larger ice particle, the so-called rimer. Heat conduction from the small droplet is

1. not symmetric
2. much faster for a given temperature

It can be argued that the heat conduction to the ice does not dominate the second freezing step completely but that an appreciable fraction of heat is conducted through the droplet surface in contact with air, so that there still is a surrounding ice shell growing into a liquid core with a faster growth component from the direction of the area in contact with the rimer.

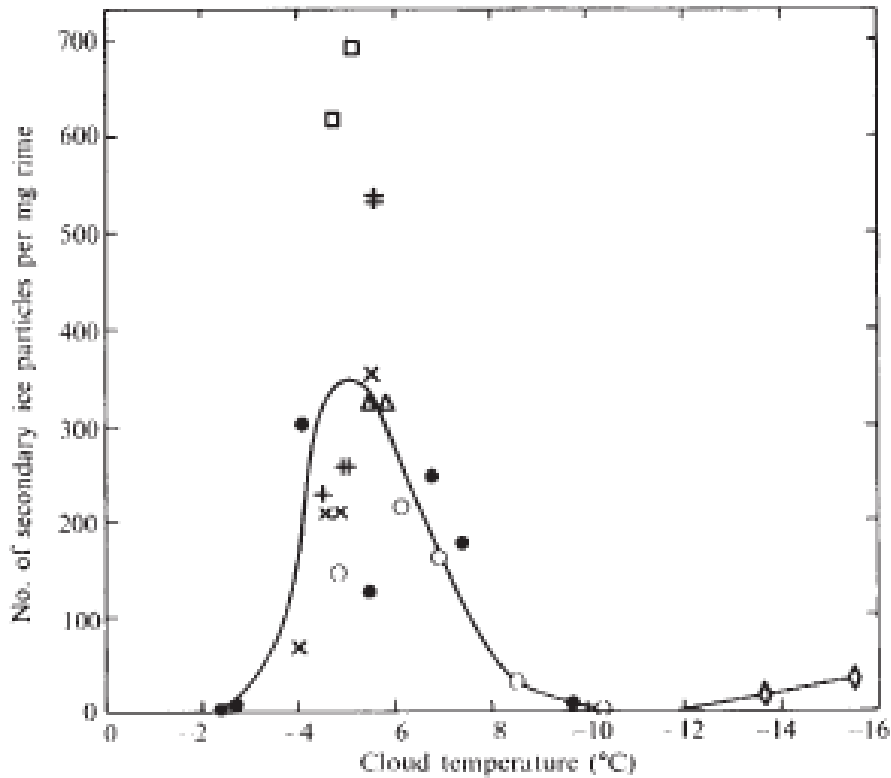


FIG. 2 Production of secondary ice particles by riming as a function of temperature at a target velocity of 2.7 m s^{-1} . Different symbols indicate different days. The curve was drawn by averaging the points over narrow temperature intervals.

Figure 5.1: Ice particles per mg of rime accreting on a riming rod, moving at 2.7 m/s (which is roughly the sedimentation velocity of a water droplet of $100\mu\text{m}$ at normal conditions). The caption reads: “Production of secondary ice particles by riming as a function of temperature at a target velocity of 2.7 m s^{-1} . Different symbols indicate different days. The curve was drawn by averaging the points over narrow temperature intervals.” From: [43].

A small droplet collected by a large ice particle basically keeps its spherical shape, and only a fraction of the droplet surface is connected to the ice substrate via a bridge. For calculating the conduction of heat, the cross-section of this bridge, $A_{droplet,connected-to-substrate}$, needs to be known as well as its ratio to the total droplet surface $A_{droplet,total}$. Assuming $\frac{A_{droplet,connected-to-substrate}}{A_{droplet,total}} = \frac{\pi r_{bridge}^2}{4\pi r_{droplet}^2}$, the heat conduction of a droplet may be separated into an air fraction and an ice fraction via

$$k_{air} + k_{evaporation} \rightarrow (k_{air} + k_{evaporation})\left(1 - \frac{\pi r_{bridge}^2}{4\pi r_{droplet}^2}\right) + k_{ice} * \frac{\pi r_{bridge}^2}{4\pi r_{droplet}^2},$$

with the heat conductivity through air, evaporation and ice k_{air} , $k_{evaporation}$ and k_{ice} , respectively. The second freezing step time $t_{2,H-M}$ of such a droplet can thus be estimated as

$$t_{2,H-M} = \frac{t_2}{\left(1 - \frac{\pi r_{bridge}^2}{4\pi r_{droplet}^2}\right) + \frac{k_{ice}}{k_{air}+k_{evaporation}} * \frac{\pi r_{bridge}^2}{4\pi r_{droplet}^2}} =: \frac{t_2}{s_{H-M}}, \quad (5.1)$$

with the shift factor s_{H-M} and t_2 as in equation 2.21 for a given temperature. The effect of bridge size on the second freezing time is presented in figure 5.2.

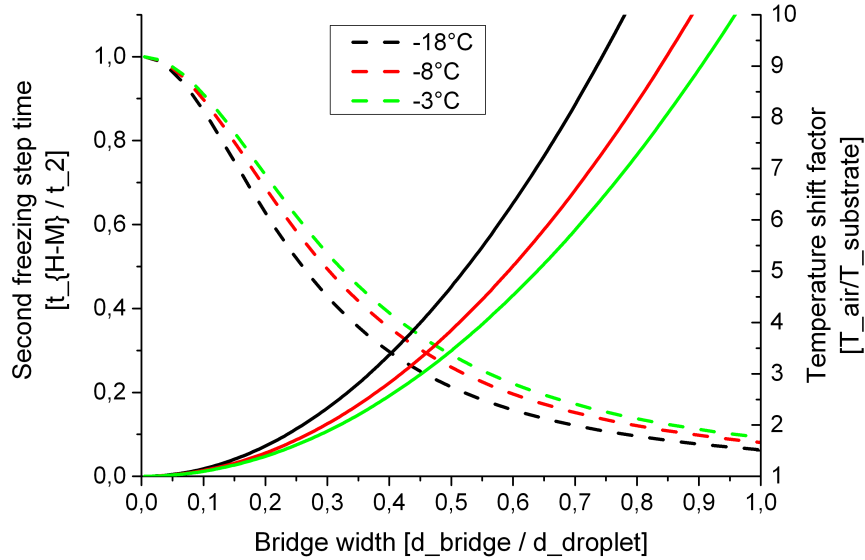


Figure 5.2: Second freezing step time and temperature shift factor for a droplet on an ice substrate in dependence of the bridge width connecting droplet and substrate for -3°C (green lines), -5°C (red lines) and -18°C (black lines). Temperature shift factor s_{H-M} and freezing time calculated according to equation 5.1. Dashed lines: relative second freezing step time reduction, compact lines: temperature shift factor.

Now, if a free-floating droplet in air is assumed with the same freezing time as a droplet on the ice substrate,

$$t_2(T_2) = t_{2,H-M}(T_1) \quad (5.2)$$

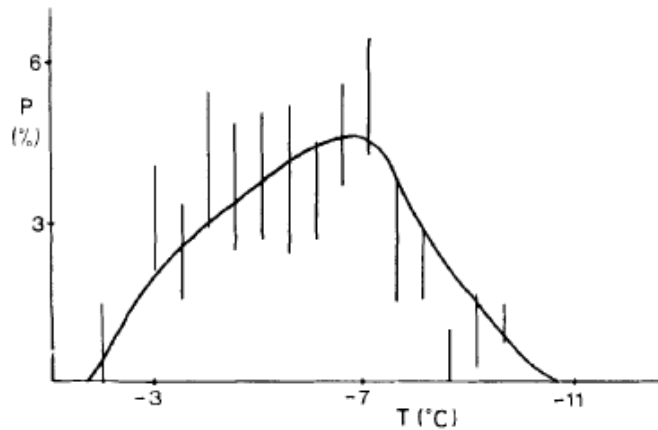
and considering $t_2 \sim 1/\Delta T$, it may be argued that a droplet on an ice substrate experiences a temperature shift of

$$\Delta T_2 / \Delta T_1 = s_{H-M} \quad (5.3)$$

relative to the ambient temperature. For a rimer and ambient temperature of -5°C , this means that a shift to -22°C to -12°C , the temperature range in which fragmentations were predominantly observed (see figure 4.12), is attained for bridge widths of 36% – 57%. This also means that a good fraction of heat is still conducted through the droplet surface in contact with air and that an ice shell may grow around a liquid core.

In [41], experiments observing riming droplets on a rimer of approximate ambient temperature were made. Their focus lay on looking for protuberances on the freezing droplets; those would suggest sufficient pressure build-up for ice particle production

by shattering and consequently secondary ice. Following the idea of linking droplet fragmentation to the Hallett-Mossop process brought forward by [18], they conducted experiments using small droplets (average radius of $5\mu\text{m}$), larger droplets (average radius of $20\mu\text{m}$) and observations could be made on the freezing process of large droplets (radii between $50\mu\text{m}$ and $250\mu\text{m}$). In small droplets, protuberances were found in the Hallett-Mossop temperature region, as is depicted in figure 5.3.



Percentage P of drops exhibiting protuberances during riming in air against air temperature T .

Figure 5.3: Protuberances in small drops (average radius $5\mu\text{m}$). Error bars calculated using the expression $(N \pm \sqrt{N})/A$, with the number of protuberances N and the total number A of drops examined at the respective temperature. From: [41].

They argued that for larger droplets on an even rimer above -7°C , the droplets' spreading on the surface would be detrimental to the build-up of an ice shell and subsequent protuberance growth.

This agrees with the findings of [27] (“Under conditions favourable for secondary ice production, the accreting droplets spread out on the ice surface”, so “Splinter formation by pressure build-up inside individual frozen droplets is therefore unlikely to be responsible for shatter”) and the temperature shift factor deliberations visualized in figure 5.2: the shift factor for a droplet spreading over a width of its diameter exceeds 10 for the temperature range relevant for the Hallett-Mossop process, e.g., shifting the temperature for a droplet on a rimer of -3°C to -32°C where the fragmentation frequency of PSL-containing droplets in the measurements of this thesis became very low (see figure 4.12).

A surface rimed with small droplets, though, does reduce the contact area between liquid droplet and ice, as [41] observed with microscopic photography, and there led to protuberances; this may be reflected in the necessity for both smaller (diameter $< 12\mu\text{m}$)

and larger (diameter $>25\mu\text{m}$) droplets in a cloud for Hallett-Mossop ice multiplication to be effective [92].

Altogether, “Observation of rime [...] revealed the same pattern of protuberance production as with the large drops, i.e. confined to the temperature range -2°C to -9°C with a maximum production rate at -6°C ” [41].

Handmann [45] investigated the position of bubbles and shots on the freezing droplets’ surfaces and found a dependence on the existence of deformations in the droplet. These measurements are shown in table 5.4.

Particle	Particle size [nm]	Experiment type	Fraction of bubbles/shots from protuberances [%]
PSL	28	suspension	83,3
PSL	400	suspension	94,3
PSL	145	aerosol	89,7
Hematite	300	aerosol	87,9

Table 5.4: Fraction of bubbles and shots that originated on protuberances on droplets in experiments with PSL and hematite as particle suspensions and aerosols. The remaining fractions of bubbles originated on an apparently undeformed spot on the surface. Data taken from [45].

From these results, it is apparent that bubbles and shots preferably originate on protuberances. This hints at a weaker ice structure in these parts of the ice shell that allows for little cracks through which water and gases from the core can be pushed. It is reasonable to assume that the increased number of protuberances in riming experiments may lead to bubbles and shots and consequently to ice multiplication. If the assumption of bubbles requiring a less pronounced pressure build-up in the core (discussed in chapter 5.4.4) is true, then bubbles may well occur on riming droplets in spite of the assymmetric heat flow.

A small droplet hitting an already frozen droplet has been recorded (see figure 5.5), but no riming-splintering events were observed in the experiments of this thesis. Still, it seems possible that there is a link between droplet fragmentation or bubbles and shots and the Hallett-Mossop process, given that a rimer’s surface is covered with frozen droplets small enough to reduce the contact area between a larger supercooled droplet and the ice substrate.

In spite of the doubts of the phase of particles generated by bubbles, bubbles and shots seem to be more likely, as fragmentation lead to distinct deformations that would most certainly have been reported if they were observed.

5.6 Fragmentations and bubbles in the literature

The data of [14, 86, 134, 136] discussed in the following section can be found in the appendix.

All their experiments employed a droplet generator, using water. [136] gave a closer specification: “Once distilled and deionized water drops (which were confirmed to supercool down to $-25\sim-30^{\circ}\text{C}$)”. From the freezing temperature, it is apparent that there still must have been particulate matter in the droplets, meaning potential lattice defects that promote fragmentations according to the insights of this thesis. So, whenever those authors speak of “water”, it may be assumed that there was an unknown amount of small particles in the droplets. Like in the experiments for this thesis, freezing was nucleated with ice particles by all authors.

In [86], the fragmentation frequencies of droplets in dependence of droplet size, nucleation temperature and air temperature were measured. On the subject of fragmentations, they state that “this explosive rupture of the frozen drop almost always produced large numbers of splinters.” Their fragmentation frequencies are generally larger than the ones reported in this thesis. This may have to do with the nucleation temperature of the droplets in their experiment which was close to 0°C in the cases when they measured the highest ice particle production per droplet. In the experiments conducted for this thesis, droplet temperature was at ambient temperature or lower when ice nucleation occurred, which means that a higher fraction of the droplet is turned to ice in the first freezing step. Regarding the higher fragmentation frequencies in the measurements of [86], this seems to be an important factor for the occurrence of fragmentation and would explain the decrease of fragmentations towards low ($\sim-36^{\circ}\text{C}$) temperatures.

They also reported to have generally observed more splinters in droplets exhibiting spike-like protuberances. Together with the findings of [45] (see table 5.4 in chapter 5.5), this means that there is a correlation between bubbles and shots and ice splinter production via droplet deformations. It is possible that shots occurred during these experiments or that bubbles do lead to ice particles and ice multiplication.

In [86], it is furthermore reported that “while no discernible changes were produced when distilled water was replaced with tap water or by 10^{-3} [molar concentration] salt solutions, drops of a $0,2$ [molar concentration] solution of sodium chloride showed no

distortion, produced no spikes and only an occasional splinter when nucleated at either -12°C or 0°C .”

This observation is consistent with the measurements of fragmentation frequencies in dependence of solubles discussed in chapters 5.3.4 and 5.3.5, but not with the occurrence of bubbles on droplets containing SNOMAX and PSL particles discussed in chapter 5.4.4. Smaller cracks reaching from the droplet core to the outside apparently still can nucleate if sufficiently large lattice defects in the form of solid particles are present in the shell.

Unfortunately, no observations were made on the occurrence of bubbles on droplets containing sodium chloride in this thesis.

The high fragmentation frequencies of the measurements of [86] have been attributed to a contamination of the droplets with carbon dioxide or by the thermal inequilibrium by [31], who found no fragmentations but found one in ten freezing droplets of 1mm diameter ejecting an ice splinter in experiments “at equilibrium in ordinary air at atmospheric pressure at temperatures from 0 to -17°C [. Those droplets] often cracked during freezing and formed spikes and protrusions, but [they] were never observed to shatter”.

A high concentration of carbon dioxide would indeed lead to an increase of the number of bubbles from a drop and probably to more shots once there is a crack in the shell that reaches from the core to the atmosphere. The fact remains that splinter production was observed in the absence of shattering, even if the number of splinters is far higher than it would be under atmospheric conditions.

The measurements of [14] are summed up with: “roughly 10 per cent of droplets between 50 and 120 μ radius shatter when nucleated with ice crystals at temperatures between -5°C and -15°C and allowed to freeze in free fall.” (that is, between 6%-9% for droplet in the diameter range of 100 μm -180 μm), which is comparable to the maximal fragmentation rates of this thesis at these temperatures (see figure 4.12). They also investigated the influence of sodium chloride on fragmentation frequency and found a decrease in frequency with concentration: “at -10°C , using droplets in the larger size range (90-120 μ radius) [...] the [droplet] percentage shattering was 7 per cent for the 10^{-4} M solution and 1 per cent for the 10^{-3} M solution” compared to 18 percent for water without added sodium chloride. This, again, is consistent with the reasoning in chapter 5.3.4.

In the measurements of [136], droplet temperature was close to air temperature and droplet sizes between 75 μm -175 μm , both of which is comparable for the experiments in this thesis ($d=85\mu\text{m}$). The fragmentation in these conditions are shown in table 5.5.

Temperature [°C]	Fragmentation frequency [%]
-6	17
-15,9	37
-24,4	2

Table 5.5: Measurement results for droplets in the size range of 75 μ m-175 μ m with nucleation temperature \approx air temperature. Data taken from [136].

The fragmentation frequencies they report are both slightly lower (at -24,4) and by a factor of ≈ 2 higher (warmer temperatures) than the frequencies of PSL suspensions measured for this thesis. In later experiments, [134] conducted experiments in which freezing was nucleated in droplets not in thermal equilibrium with the surrounding air. In general, higher fragmentation frequencies were observed than in [136] where the same experimental apparatus was employed. This fact, as in the discussion in [86], hints at the importance of the fraction turned into ice during the first freezing step, which is governed by the droplet temperature at the time of nucleation, for fragmentation. A high temperature difference between the droplet and the ambient air is highly unlikely under non-laboratory conditions, though, so the relevance of these measurements for atmospheric clouds seems limited.

In [63], the investigations centered on hailstone embryos, i.e., the ice particle of the core of a hailstone. The core of a hailstone is necessarily a frozen drop.

It might be argued that the reason for this droplet's freezing is either an ice-active aerosol or an ice particle, but the mechanism of hailstone growth requires an ice particle large enough to collect large liquid water droplets that form layers of liquid around the ice and freeze subsequently. This is reflected in the structure of a hailstone, which is revealed if the cross-section is examined (figure 5.4). They found, of 452 frozen drop embryos, 13% were broken pieces: "usually hemisphere, sometimes other portions". They found few cases of fragments called 'incomplete fragmentations' in this thesis (chapter 4.3.7.2): "While cracking and discrete breaking are common, both spike formation and cracking with displacement of the pieces but without complete separation are extremely rare." Unfortunately, they did not report the weather conditions under which the hailstones were collected, but a fragmentation frequency of $\sim 13\%$ has been observed for a variety of conditions (figures 4.12, 4.3, 4.14) in this thesis.

One of the latest laboratory experiments was conducted by [109]. They found that "depending on the drop surface temperature, up to 42% of the drops frozen by contact nucleation with a clay aerosol transformed into ice particles with surface breaks that

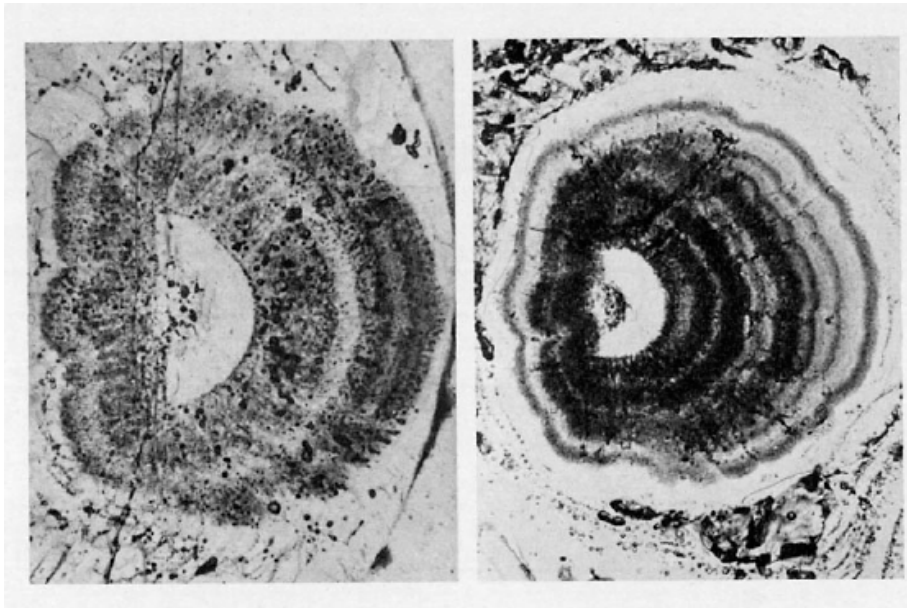


FIG. 1. Embryo portions of two stones with broken-drop centers. Top: collected North of Stoneham, Colo., on 15 July 1971, length of the flat side of the hemisphere 2.9 mm; bottom: collected at Sickles, Okla., 18 June 1973, length of the flat side of the hemisphere 4.1 mm. In both of these cases, further accretion appears to be dry growth, and is clearly much faster on the rounded side of the hemisphere than on the flat side, indicating that these hemispheres tend to fall with the rounded side down. This is most commonly the case.

Figure 5.4: Hailstone cores consisting of fragmented droplets. Source: [63].

resulted from ejection of 1 splinter, whereas only up to 8.5% of the frozen drops shattered and split into 2–3 fragments, and only up to 6.3% of the frozen drops totally ruptured into a large (>3) but undetermined number of very small ice fragments.” These frequencies are comparable with the ones presented in this thesis regarding shots and fragmentations.

It has been reported that the crystal structure of freezing droplets influences their shattering probability [135] and the growth of protrusions [62], but experiments with crossed polarization filters to investigate into the crystal structure of freezing droplets did not prove successful during the experiments for this thesis.

Newer measurements by [114] in shallow maritime clouds showed a “modest, though not insignificant role for the fragmentation of freezing drops on total ice particle concentrations when larger supercooled drops are present”. “In those limited regions where ice appeared to be newly formed, ice fragments with rounded portions accounted for about 5% of the total ice particle concentrations”, which was attributed to droplet fragmentation during freezing.

The results of this thesis regarding the occurrence of fragmentations are in good agreement with values found in literature, except for the reports of very high fragmentation frequency numbers ([86, 134]), where the droplets were by several degrees warmer than the ambient air which was never the case in the experiments presented here. The subject of bubbles on freezing droplets has, apparently, so far not been a phenomenon addressed in publications, so no comparison could be made. Protrusions in freezing droplets, on the other hand, have been. Generally, a correlation between

droplet deformations and ice splinter number was reported; together with the correlation between protuberances and bubbles found by [45], a correlation between bubbles and splinter production is possible. But before the nature of particles from bursting bubbles on freezing droplets is determined, this has to remain a speculation.

Most of the experiments on ice multiplication based on single freezing droplets that are reported were conducted in the 1960s and '70s. The research of conditions under which the Hallett-Mossop process operates was never quite discontinued (e.g., [121]), but no description of the actual process responsible for “riming-splintering” has been found in the research for this thesis.

It is the author’s opinion, based on the considerations laid out in chapters 5.5 and 5.6, there is a connection between the Hallett-Mossop process and the ice multiplication processes in single freezing droplets described in this thesis.

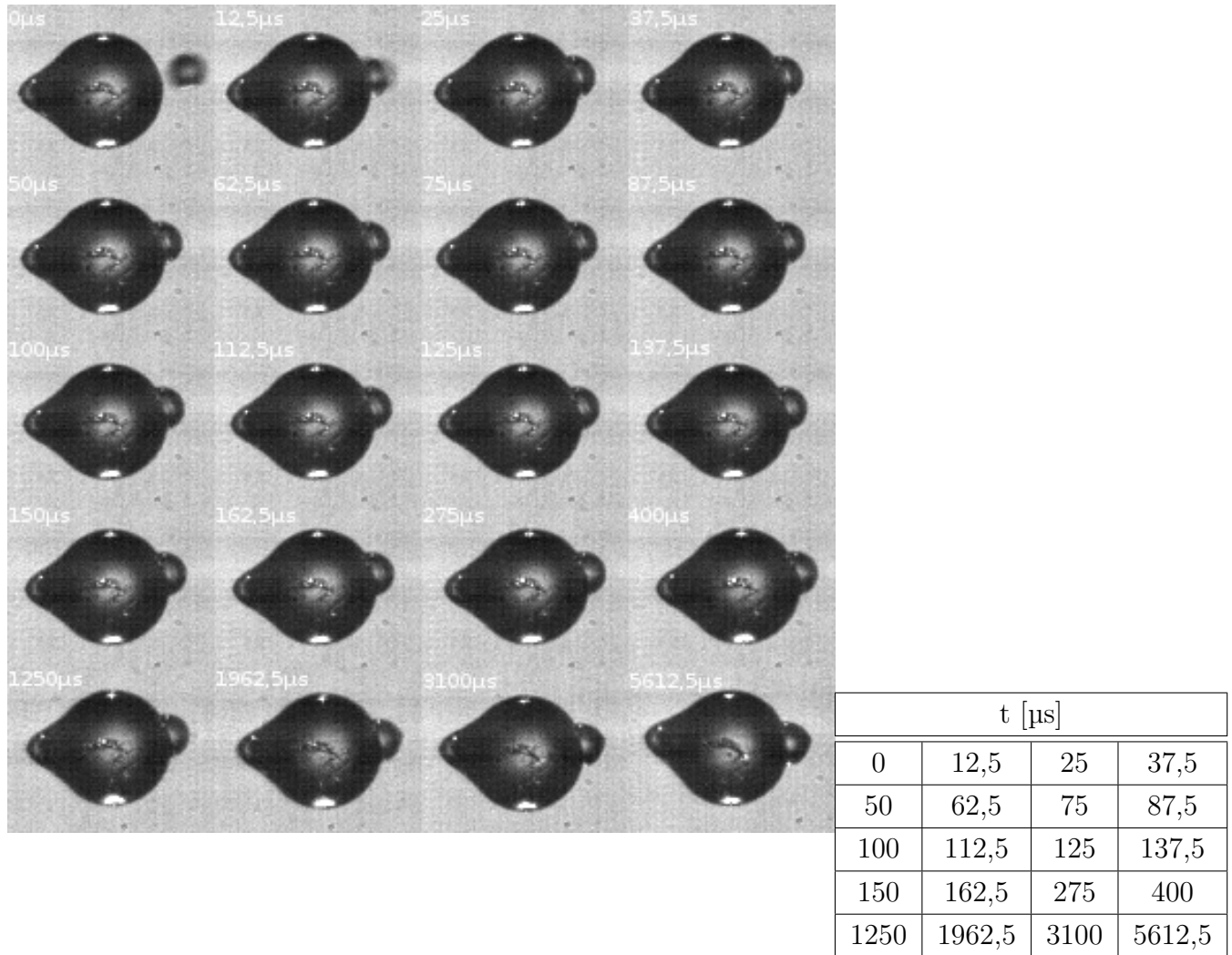


Figure 5.5: Riming event at $-15,66^{\circ}\text{C}$ droplet temperature. A larger, frozen droplet is hit by a small droplet which becomes slightly deformed towards the end of its freezing. Large droplet diameter is $68\mu\text{m}$ (short axis), small droplet diameter before contact is $20\mu\text{m}$. Position of time value in table corresponds to picture at the same position.

Chapter 6

Summary

For this thesis, experiments have been conducted at the division 'Atmospheric Aerosol Research' of the Institute for Meteorology and Climate Research (IMK-AAF), Karlsruhe Institute of Technology (KIT). The aim of these experiments has been to find the conditions under which ice multiplication takes place, which in this case means the shedding of ice particles in single freezing water droplets. To this end, water droplets of (78 ± 22) μm were levitated in an electrodynamic balance which was cooled to temperatures from 0°C to -36°C .

It had been found before that such pure water droplets show virtually no ice multiplication during freezing [103], so the experiment focused on droplets containing solid particles. It was reasoned that particles would serve as lattice defects in the growing ice shell of a droplet and might promote the nucleation of cracks under the pressure growing in the liquid core due to the lower density of ice.

Indeed, cracks in the shell were observed to lead to two ice multiplication processes:

Fragmentation Under high pressure in the core, and consequently high stresses in the ice surrounding the core, the ice shell breaks on the scale of the droplet diameter. The fragments separate at relative speeds of up to 4m/s (figure 4.16) which cannot be explained by electrostatic repulsion of the fragments. During a fragmentation, small ice splinters might have been ejected as well, but have not been observed due to limits of the camera resolution.

Bubbles A smaller crack reaching from the liquid core to the shell boundary with air may form. Through this channel, water and gases dissolved in the droplet are pushed to the outside where bubbles form. In a subset of such events, 'shots' of bubble fragments were observed that consisted of ice, while for most bubbles the existence or phase of ejected particles remained unknown (rationale for this given

in chapter 5.4.1).

Two strategies were followed to introduce particles in- or onto droplets: suspension experiments and aerosol experiments.

For the suspension experiments, polystyrene spheres ('PSL'), the clay mineral kaolinite, bacterial cell fragments ('SNOMAX') or sodium chloride were mixed with pure water. The polystyrene spheres were chosen because of their defined size and because of the assumption that the particle number per droplet would be well-defined. Kaolinite was chosen as a proxy for mineral dusts in the atmosphere. Sodium chloride was used to investigate the influence of solubles, rainwater was used as a proxy for cloud droplets. SNOMAX was employed because it is a material capable of ice nucleation at temperatures warmer than -20°C , in contrast to kaolinite which did not nucleate ice above -28°C ; in all other experiments, ice was nucleated with small ice particles impinging onto the droplets.

In the aerosol experiments, particles were collected on pure water droplets. The particles collected were either polystyrene spheres, hematite particles or SNOMAX particles.

The effect of the individual particles and solubles are presented in table 6.1 for the occurrence of fragmentations and in table 6.2 for bubbles.

In experiments with solubles (rain water, sodium chloride and SNOMAX), the fragmentation frequency was reduced to almost zero. The bubble frequency was higher, especially in the measurements with SNOMAX and PSL particles in droplets. It has been discussed in this thesis (chapter 5.3.4) that solubles reduce the strength of ice and thus prevent larger cracks from occurring; the shell yields gradually in smaller increments which prevents higher pressure build-up. In the case of bubbles, smaller cracks reaching from the droplet core to the outside apparently still can nucleate if sufficiently large lattice defects in the form of solid particles are present in the shell.

Together with the findings of [45], who observed 2-6 individual bubbles during each bubble event, bubbles may lead to more ice splinters than fragmentations. Results regarding ice multiplication in single freezing droplets found in literature and discussed in chapter 5.6 point to splinter production in the absence of fragmentation, which may mean that bubbles do create ice.

In this thesis, a link between fragmentations and bubbles to the Hallett-Mossop process (see [43]), a highly effective ice multiplication process between -8°C and -3°C , has been explored. The Hallett-Mossop process, also called 'riming-splintering', takes place on an large ice particle covered in fine rime on which droplets of diameters larger than

Experiment type	Particle type	Particle diameter [nm]	Temperature range [°C]	Fragmentation frequency [%]	Data
Suspension	Polystyrene spheres	28	-28 to -10	2 - 15	Figure 4.12
		400	-36 to -8	1 - 18	
	Kaolinite	<10000	-27 to -20	0 - 13	Table 4.3
	Sodium chloride	31000	-26 to -7	0 - 2	Table 4.4
	Rainwater		-32 to -28	0	Table 4.5
	SNOMAX		-21 to -12	0	Table 4.6
	SNOMAX + Polystyrene spheres	400	-25 to -11	0	Table 4.7
Aerosol	Polystyrene spheres	100	-28 to -16	0 - 10	Figure 4.15
	Hematite	300	-34 to -16	0 - 2	
	SNOMAX	322	-30 to -24	0 - 2	

Table 6.1: Fragmentation occurrence in dependence of particles and solubles. For sodium chloride, a particle size equivalent to the content in a drop was calculated, for the SNOMAX suspension and rainwater the particle diameters were not known.

Experiment type	Particle type	Particle diameter [nm]	Temperature range [°C]	Bubble frequency [%]	Data
Suspension	Polystyrene spheres	400	-36 to -8	Bubbles: 0 - 6	Figure 4.19
				Shots 0- 9	
	Rainwater		-32 to -28	0 - 5	Table 4.10
	Kaolinite	<10000	-27 to -20	0 - 1	Table 4.9
	SNOMAX		-21 to -12	0	Table 4.11
SNOMAX + Polystyrene spheres	400	-25 to -11	0 - 17	Table 4.12	
Aerosol	Hematite	300	-34 to -16	1 - 4	Figure 4.20

Table 6.2: Bubble occurrence in dependence of particles and solubles. In the measurements of polystyrene spheres, shots could be clearly observed. For the SNOMAX suspension and rainwater the particle diameters were not known.

the rime impinge (a description of the physics involved in this process has not been found, though). In calculations in chapter 5.5, it has been shown that the heat flow of a droplet connected to a larger rimer via a connection smaller than the droplet diameter causes a decrease in the freezing time of the droplet. This time decrease was interpreted as being equivalent to a temperature decrease, relative to the rimer's temperature, in a droplet in air. This decrease can shift the temperature range of the Hallett-Mossop process into the temperature range in which fragmentations and bubbles were most frequent in the experiments in this thesis, depending on the connecting area between droplet and rimer. In [41], the occurrence of protuberances on frozen droplets on a rimed surface in the Hallett-Mossop temperature range is reported, and [45] found a correlation between protuberances and bubbles across temperatures from -36°C to -8°C (table 5.4) in freezing droplets. These three insights together lead to the conclusion that the ice multiplication effect of the Hallett-Mossop process may be caused by bubbles or shots from riming larger droplets on a finely rimed ice surface.

Generally, the complete freezing process from ice nucleation to the end was recorded, unless the droplet was removed from the field of vision by fragmentation. This allowed for the analysis of the first freezing step time and the propagation speed of ice in supercooled water in dependence of droplet temperature T and melting temperature of water T_m . In this thesis, the propagation speed v_{ice} between -34°C and -7°C has been measured to be $v_{ice} = (0,75 \pm 0,33) * 10^{-3} (\frac{T_m - T}{\text{K}})^{1,83 \pm 0,14} \text{m/s}$ which is in good agreement with literature measurements and spans the widest range of temperature with the same experimental setup.

A series of experiments on droplet actuation lead to the discovery of actuation signals with which the droplet size of the piezoelectric droplet injector could be varied from the standard diameter of $90\mu\text{m}$ to the range of $60\mu\text{m}$ - $105\mu\text{m}$ without changing the injector's geometry. Instead of the usual single pulse signal, a combined signal of three successive pulses allowed for these size manipulation (see chapter 5.1.4). In experiments in the cooled environment of the electrodynamic balance it turned out that the heating applied to the injector to prevent ice damage caused evaporation in the droplet before capture. The droplet size was reduced from a reference size of $90\mu\text{m}$ to $64\mu\text{m}$, and the range of diameters generated with suitable triple pulse signals became $45\mu\text{m}$ - $77\mu\text{m}$. This prompts the conclusion that injector heating control might offer a much easier way of producing smaller water droplets. Pulse variation might be relevant for experiments with heat-sensitive fluids and suspensions or for expanding the limits of droplet variation by temperature control.

Three questions were asked at the beginning of this thesis. Answers have been found:

- Under which conditions do fragmentations occur?
 - Fragmentations were observed in droplets with diameters of $\approx 85\mu\text{m}$ containing solid particles, but not high concentration of solubles. While fragmentations occurred over the temperature range of -30°C to -8°C , fragmentation frequencies $>5\%$ took place in the range of -23°C to -13°C in experiments with polystyrene spheres ($d=28\text{nm}$ and 400nm) suspended in the observed droplets. In experiments with potentially larger particles (kaolinite), a fragmentation frequency of 13% could be observed at -27°C droplet temperature. Fragmentations may also occur if the particles are at the water-air boundary of the droplet before freezing.
- Are there other ice multiplication processes in freezing droplets that have not been considered yet?
 - Water and gases of a freezing droplet's core may be pushed through a crack in the shell to the outside where they may shed splinters upon freezing. There was a series with suspensions of polystyrene spheres ($d=400\text{nm}$) in which the phase of bubbles shed from a droplet could be identified as ice; for most other measurements, it is not clear if ice multiplication took place.
- Is there a link between the Hallett-Mossop process and droplet fragmentation?
 - Fragmentations require a high pressure in a freezing droplet which is best achieved with a symmetrically growing ice shell. This makes it improbable that freezing droplets sitting on a rimer fragment, as the heat flow to the rimer necessarily leads to an asymmetric heat flow and consequently to asymmetric ice shell growth. The contact area between droplet and rimer plays an important role for this asymmetry. A small contact area might allow for the growth of an ice shell from the remaining droplet surface, which exchanges heat with the ambient air, that becomes strong enough for the build-up of high pressures necessary for fragmentation. On the other hand, there is a reported correlation between ice splinter production and protrusions, and there is a reported correlation between protrusions and bubbles. Following this line of thought, bubbles emerging from freezing droplets may be the cause of ice

multiplication in the Hallett-Mossop process, which might link the presented laboratory experiments in this thesis to the rapid increase in ice crystals in clouds occasionally observed in field studies.

These results may be of use in further research on the mechanisms of ice multiplication. The measurements on actuation signal variation in the droplet injector may be useful for investigating into the droplet size dependency of ice multiplication processes, but might prove useful for other applications (e.g., cold stage experiments) as well.

The idea of connecting bubble emergence from freezing droplets to the Hallett-Mossop process is, as of now, little more than a substantiated conjecture. A life observation of riming would be a difficult but rewarding experiment to assay the truth of this idea. Any experiments that prove this conjecture wrong are just as welcome as a confirmation would be, as that would mean that the work in the research field of ice multiplication continues. For decades, few experiments have been conducted on this subject, and it is high time the hiatus ended. Just the same has been said the conveners of the *Secondary ice multiplication Symposium* in Manchester, 3rd - 4th of November 2015 in their invitation:

“The time is now ripe to review our progress in understanding secondary ice multiplication and suggest new ways forward.”

Chapter 7

Appendix

7.1 Experimental setup list

The basic setup is listed in table [7.1](#), the aerosol system in table [7.2](#).

Instrument	Model	Producer	Comment
Cooling system	FP-50	Julabo	-40°C - +20°C temperature range
Temperature monitor	Model 218	Lakeshore	
High-speed camera	Phantom v710	Vision research	up to 150000 frames per second
CCD camera	DMK 21BF04	Imagingsource	
LED	DRAGONeye	OSRAM	$\lambda=616\text{nm}$
	OSTAR Headlamp Pro LE UW U1A3 01	OSRAM	white light, brighter than the DRAGONeye
Droplet injector	SPIP	GeSim	
Water supply	NANOpure® Infinity Base Unit	Barnstead - Thermolyne Corporation	highly pure water supply (resistance of $18\text{M}\Omega/\text{cm}$)
Power source and droplet position control program	Custom-made	Jens Nadolny	Jens Nadolny was a colleague at the IMK-AAF
Arbitrary waveform function generator	33522A	Agilent	
Air flow controller	2900	Tylan	up to $119\text{ cm}^3\text{min}^{-1}$
Droplet injector	SPIP	GeSiM	

Table 7.1: List of peripheral instruments for the basic setup (chapter 3.1.1).

Instrument	Model	Producer	Comment
Fluidized bed generator	3400A	TSI	
Atomizer	3776	TSI	
Electrostatic Classifier	3080	TSI	
Ultrafine Condensation Particle Counter	3776	TSI	

Table 7.2: List of instruments for the aerosol setup (chapter 3.2).

7.2 Fragmentation frequencies in the literature

The data of [86] and [14] are shown in table 7.3, the data of [136] and [134] in table 7.4.

Investigator	Droplet diameter [μm]	Nucleation temperature [$^{\circ}\text{C}$]	Air temperature [$^{\circ}\text{C}$]	Protuberance frequency [%]	Fragmentation frequency [%]	Average splinter number per drop	Comment
[86]	1000	0	-2	72	29	-	"Large droplets, of millimetre size, were suspended from the end of a fine, shellac-coated thermocouple [...]. Smaller droplets, of order 100 μ diameter, were hung from the underside of fine, horizontally mounted amyl-acetate fibres."
		-1	-10	91	47	54	
		-1	-10	83	44	-	
		-2	-15	57	21	-	
		-2	-20	67	39	-	
		-4	-10	40	22	27	
		-7	-10	8	6	15	
		-9	-17	0	0	4	
		-13	-15	few	0	4	
		-14	-20	small	0	4	
	-16	-25	spikes	0	6		
	300 - 400	-1	-10	90	40	-	
		-1	-12	100	27	40	
		-2	-20	70	20	-	
		-15	-20	0	6	5	
	100 - 150	-2	-15	39	15	-	
		-5	-15	27	12	14	
		-15	-15	7	1	3	
	80 - 120	0	-5	51	25	-	
		0	-6	60	35	22	
30 - 80	0	-5	57	26	-		
	0	-6	43	27	-		
	-5	-6	-	11	8		
[14]	160 - 240		-5		6		
			-10		18		
			-10		7		10 ⁻⁴ M sodium chloride solution
			-10		1		10 ⁻³ M sodium chloride solution
	100 - 180		-15		14		
			-5		9		
			-10		7		
		-15		6			

Table 7.3: Fragmentation frequencies in the literature I

Investigator	Droplet diameter [μm]	Nucleation temperature [$^{\circ}\text{C}$]	Air temperature [$^{\circ}\text{C}$]	Protuberance frequency [%]	Fragmentation frequency [%]	Splinter number per drop	Comment
[136]	75 - 175	≈ -6	-6		17		“Once distilled and deionized water drops (which were confirmed to supercool down to $-25\sim-30^{\circ}\text{C}$) were dropped in a supercooled cloud and were nucleated by collision with tiny ice crystals.”
		$\approx -15,9$	-15,9		37		
		$\approx -24,4$	-24,4		2		
	150-300	$\approx -15,4$	-15,4		22		
		$\approx -24,3$	-24,3		0		
[135]	300 - 500	-13,7	-25,0		53	2	
		-13,7	-20,5		68	3	
		-7,5	-19,7		10	0,4	
	200 - 400	-16,4	-20,1			8	
		-16,4	-18,1		39	2	
		-16,1	-24,8		48	0,8	
		-14,9	-19,7		47	8	
		-14,3	-20,1		39	2	
		-14,3	-20,3		40	4	
		-13,4	-19,9		43	0,7	
		-7,1	-25,0		8	0,1	
	50 - 150	-5,9	-19,4		9	0,7	
		-16,7	-24,7			0,8	
		-16,3	-21,2		49	0,6	
		-11,2	-15,6		27	0,7	
		-8,7	-19,7			0,2	
		-7,3	-24,5			2	
		-7,3	-14,7			0,2	

Table 7.4: Fragmentation frequencies in the literature II

Bibliography

- [1] Andrew S. Ackerman, Owen B. Toon, Jonathan P. Taylor, Doug W. Johnson, Peter V. Hobbs, and Ronald J. Ferek. Effects of Aerosols on Cloud Albedo: Evaluation of Twomeys Parameterization of Cloud Susceptibility Using Measurements of Ship Tracks. *Journal of the Atmospheric Sciences*, 57(16):2684–2695, August 2000.
- [2] John Aitken. On the number of dust particles in the atmosphere. *Nature*, 37:428–430, 1888.
- [3] Largus T Angenent, Scott T Kelley, Allison St Amand, Norman R Pace, and Mark T Hernandez. Molecular identification of potential pathogens in water and air of a hospital therapy pool. *Proceedings of the National Academy of Sciences of the United States of America*, 102(13):4860–4865, 2005.
- [4] James D. Atkinson, Benjamin J. Murray, Matthew T. Woodhouse, Thomas F. Whale, Kelly J. Baustian, Kenneth S. Carslaw, Steven Dobbie, Daniel O’Sullivan, and Tamsin L. Malkin. The importance of feldspar for ice nucleation by mineral dust in mixed-phase clouds. *Nature*, 498(7454):355–358, 2013.
- [5] S. Augustin, S. Hartmann, B. Pummer, H. Grothe, D. Niedermeier, T. Clauss, J. Voigtländer, L. Tomsche, H. Wex, and F. Stratmann. Immersion freezing of birch pollen washing water. *Atmos. Chem. Phys. Discuss.*, 12(12):32911–32943, 2012.
- [6] Tor Bergeron. On the Physics of Cloud Precipitation. 1935.
- [7] Heinz Bingemer, Holger Klein, Martin Ebert, Werner Haunold, Ulrich Bundke, Thomas Herrmann, Konrad Kandler, Dörthe Müller-Ebert, Stephan Weinbruch, and Anna Judt. Atmospheric ice nuclei in the Eyjafjallajökull volcanic ash plume. *Atmospheric Chemistry and Physics*, 12(2):857–867, 2012.

-
- [8] James C. Bird, Rielle de Ruiter, Laurent Courbin, and Howard A. Stone. Daughter bubble cascades produced by folding of ruptured thin films. *Nature*, 465(7299):759–762, 2010.
- [9] Alan M. Blyth and John Latham. Development of ice and precipitation in New Mexican summertime cumulus clouds. *Quarterly Journal of the Royal Meteorological Society*, 119(509):91–120, 1993.
- [10] Olivier Boucher and Ulrike Lohmann. The sulfate-CCN-cloud albedo effect. *Tellus Series B-Chemical and Physical Meteorology*, 47(3):281–300, 1995.
- [11] Roscoe R. Braham. What is the Role of Ice in Summer Rain-Showers? *Journal of the Atmospheric Sciences*, 21(6):640–645, November 1964.
- [12] James R. Brock. On the theory of thermal forces acting on aerosol particles. *Journal of Colloid Science*, 17(8):768–780, 1962.
- [13] Francois-Marie Bréon, Didier Tanré, and Sylvia Generoso. Aerosol Effect on Cloud Droplet Size Monitored from Satellite. *Science*, 295(5556):834–838, February 2002.
- [14] J. L. Brownscombe and Thorndike.Ns. Freezing and Shattering of Water Droplets in Free Fall. *Nature*, 220(5168):687–&, 1968.
- [15] W. Cantrell and A. Heymsfield. Production of ice in tropospheric clouds - A review. *Bulletin of the American Meteorological Society*, 86(6):795–+, June 2005.
- [16] Alvin U. Chen and Osman A. Basaran. A new method for significantly reducing drop radius without reducing nozzle radius in drop-on-demand drop production. *Physics of Fluids*, 14(1):L1–L4, 2002.
- [17] Chul Hee Cho, Surjit Singh, and G. Wilse Robinson. An Explanation of the Density Maximum in Water. *Physical Review Letters*, 76(10):1651–1654, 1996.
- [18] T. W. Choullarton, J. Latham, and B. J. Mason. Possible Mechanism of Ice Splinter Production during Riming. *Nature*, 274(5673):791–792, 1978.
- [19] Clifford Coonan. How Beijing used rockets to keep opening ceremony dry. *The Independent*, November 2008.
- [20] E. Cunningham. *On the Velocity of Steady Fall of Spherical Particles through Fluid Medium*, volume 83. March 1910.

-
- [21] C. N. Davies. Definitive equations for the fluid resistance of spheres. *Proceedings of the Physical Society*, 57(4):259, 1945.
- [22] E James Davis. A history of single aerosol particle levitation. *Aerosol Science and Technology*, 26(3):212–254, 1997.
- [23] Gerrit de Leeuw, Edgar L. Andreas, Magdalena D. Anguelova, C. W. Fairall, Ernie R. Lewis, Colin O’Dowd, Michael Schulz, and Stephen E. Schwartz. Production flux of sea spray aerosol. *Reviews of Geophysics*, 49(2):RG2001, 2011.
- [24] K. Diehl, S. Matthias-Maser, R. Jaenicke, and S. K. Mitra. The ice nucleating ability of pollen:: Part II. Laboratory studies in immersion and contact freezing modes. *Atmospheric Research*, 61(2):125–133, 2002.
- [25] Gerald A Domoto and Aron Sereny. Thermal ink jet printer with droplet ejection by bubble collapse. 1986.
- [26] Hongming Dong, Wallace W. Carr, and Jeffrey F. Morris. An experimental study of drop-on-demand drop formation. *Physics of Fluids*, 18(7):072102–16, 2006.
- [27] Ya Yi Dong and John Hallett. Droplet accretion during rime growth and the formation of secondary ice crystals. *Quarterly Journal of the Royal Meteorological Society*, 115(485):127–142, 1989.
- [28] Stillman Drake and Galileo Galilei. *Cause, Experiment and Science: a Galilean Dialogue Incorporating a New English Translation of Galileo’s Bodies that Stay Atop Water, Or Move in it*. Chicago: University of Chicago Press, 1981.
- [29] Laurent Duchemin, Stéphane Popinet, Christophe Josserand, and Stéphane Zaleski. Jet formation in bubbles bursting at a free surface. *Physics of Fluids (1994-present)*, 14(9):3000–3008, 2002.
- [30] Denis Duft and Thomas Leisner. Laboratory evidence for volume-dominated nucleation of ice in supercooled water microdroplets. *Atmospheric Chemistry and Physics*, 4(7):1997–2000, 2004.
- [31] James Eugene Dye and PV Hobbs. The influence of environmental parameters on the freezing and fragmentation of suspended water drops. *Journal of the Atmospheric Sciences*, 25(1):82–96, 1968.

- [32] J. Feichter and T. Leisner. Climate engineering: A critical review of approaches to modify the global energy balance. *The European Physical Journal Special Topics*, 176(1):81–92, September 2009.
- [33] W Findeisen. Die kolloidmeteorologischen Vorgänge bei der Niederschlagsbildung. *Meteor. Z*, 55:121–133, 1938.
- [34] C.J. G. Method and apparatus for heating dielectric materials, 1939.
- [35] H. Y. Gan, Shan Xuechuan, T. Eriksson, B. K. Lok, and Y. C. Lam. Reduction of droplet volume by controlling actuating waveforms in inkjet printing for micro-pattern formation. *Journal of Micromechanics and Microengineering*, 19(5):055010, 2009.
- [36] Michal Gavish, Ronit Popovitz-Biro, Meir Lahav, and Leslie Leiserowitz. Ice Nucleation by Alcohols Arranged in Monolayers at the Surface of Water Drops. *Science*, 250(4983):973–975, 1990.
- [37] GESIM. Nanolitre Dosage Piezoelectric Microdispensers. Product information, 2014.
- [38] Elisabeth Ghabache, Arnaud Antkowiak, Christophe Josserand, and Thomas Séon. On the physics of fizziness: How bubble bursting controls droplets ejection. *Physics of Fluids (1994-present)*, 26(12):–, 2014.
- [39] WF Giauque and JW Stout. The Entropy of Water and the Third Law of Thermodynamics. The Heat Capacity of Ice from 15 to 273° K. *Journal of the American Chemical Society*, 58(7):1144–1150, 1936.
- [40] Robert J Good. Contact angle, wetting, and adhesion: a critical review. *Journal of adhesion science and technology*, 6(12):1269–1302, 1992.
- [41] D. J. Griggs and T. W. Choularton. Freezing modes of riming droplets with application to ice splinter production. *Quarterly Journal of the Royal Meteorological Society*, 109(459):243–253, 1983.
- [42] J. Hallett. Experimental Studies of the Crystallization of Supercooled Water. *Journal of the Atmospheric Sciences*, 21(6):671–682, November 1964.
- [43] J. Hallett and S. C. Mossop. Production of Secondary Ice Particles during Riming Process. *Nature*, 249(5452):26–28, 1974.

- [44] John Hallett, Robert I Sax, Dennis Lamb, and AS Murty. Aircraft measurements of ice in Florida cumuli. *Quarterly Journal of the Royal Meteorological Society*, 104(441):631–651, 1978.
- [45] Patricia Vera Klara Handmann. *Laboruntersuchungen zur Dynamik der Sekundäreisbildung*. Diploma thesis, Karlsruhe, 2013.
- [46] D. E. Hare and C. M. Sorensen. The density of supercooled water. II. Bulk samples cooled to the homogeneous nucleation limit. *The Journal of Chemical Physics*, 87(8):4840–4845, 1987.
- [47] Raymond L. Harris-Hobbs and William A. Cooper. Field Evidence Supporting Quantitative Predictions of Secondary Ice Production Rates. *Journal of the Atmospheric Sciences*, 44(7):1071–1082, April 1987.
- [48] R. B. Head. Steroids as Ice Nucleators. *Nature*, 191(479):1058–&, 1961.
- [49] Stephen J Henderson and Robin J Speedy. Melting temperature of ice at positive and negative pressures. *Journal of Physical Chemistry*, 91(11):3069–3072, 1987.
- [50] Andrew Heymsfield and Paul Willis. Cloud Conditions Favoring Secondary Ice Particle Production in Tropical Maritime Convection. *Journal of the Atmospheric Sciences*, 71(12):4500–4526, December 2014.
- [51] W. B. Hillig and D. Turnbull. Theory of Crystal Growth in Undercooled Pure Liquids. *Journal of Chemical Physics*, 24(4):914–914, 1956.
- [52] Peter V. Hobbs and Arthur L. Rangno. Ice Particle Concentrations in Clouds. *Journal of the Atmospheric Sciences*, 42(23):2523–2549, December 1985.
- [53] N. Hoffmann, A. Kiselev, D. Rzesanke, D. Duft, and T. Leisner. Experimental quantification of contact freezing in an electrodynamic balance. *Atmos. Meas. Tech.*, 6(9):2373–2382, 2013.
- [54] C. Hoose, J. E. Kristjánsson, and S. M. Burrows. How important is biological ice nucleation in clouds on a global scale? *Environmental Research Letters*, 5(2):024009, 2010.
- [55] C. Hoose and O. Möhler. Heterogeneous ice nucleation on atmospheric aerosols: a review of results from laboratory experiments. *Atmos. Chem. Phys.*, 12(20):9817–9854, 2012.

- [56] J. A. Huffman, A. J. Prenni, P. J. DeMott, C. Pöhlker, R. H. Mason, N. H. Robinson, J. Fröhlich-Nowoisky, Y. Tobo, V. R. Després, E. Garcia, D. J. Gochis, E. Harris, I. Müller-Germann, C. Ruzene, B. Schmer, B. Sinha, D. A. Day, M. O. Andreae, J. L. Jimenez, M. Gallagher, S. M. Kreidenweis, A. K. Bertram, and U. Pöschl. High concentrations of biological aerosol particles and ice nuclei during and after rain. *Atmospheric Chemistry and Physics*, 13(13):6151–6164, July 2013.
- [57] Ipc. Summary for Policymakers. In C. B. Field, V. R. Barros, D. J. Dokken, K. J. Mach, M. D. Mastrandrea, T. E. Bilir, M. Chatterjee, K. L. Ebi, Y. O. Estrada, R. C. Genova, B. Girma, E. S. Kissel, A. N. Levy, S. MacCracken, P. R. Mastrandrea, and L. L. White, editors, *Climate Change 2014: Impacts, Adaptation, and Vulnerability. Part A: Global and Sectoral Aspects. Contribution of Working Group II to the Fifth Assessment Report of the Intergovernmental Panel on Climate Change*, pages 1–32. Cambridge University Press, Cambridge, United Kingdom, and New York, NY, USA, 2014.
- [58] J. P. Kallungal and A. J. Barduhn. Growth-Rate of an Ice Crystal in Subcooled Pure Water. *Aiche Journal*, 23(3):294–303, 1977.
- [59] Hilding Köhler. The nucleus in and the growth of hygroscopic droplets. *Transactions of the Faraday Society*, 32:1152–1161, 1936.
- [60] W D King and N H Fletcher. Pressures and stresses in freezing water drops. *Journal of Physics D: Applied Physics*, 6(18):2157, 1973.
- [61] Charles A. Knight. Spiral Air Bubbles in Ice. *Nature*, 214(5095):1324–1325, 1967.
- [62] Charles A. Knight. An exploratory study of ice-cube spikes. *Journal of Glaciology*, 51(173):191–200, 2005.
- [63] Charles A. Knight and Nancy C. Knight. Drop Freezing in Clouds. *Journal of the Atmospheric Sciences*, 31(4):1174–1176, May 1974.
- [64] Kirsten A Koehler, Paul J DeMott, Sonia M Kreidenweis, Olga B Popovicheva, Markus D Petters, Christian M Carrico, Elena D Kireeva, Tatiana D Khokhlova, and Natalia K Shonija. Cloud condensation nuclei and ice nucleation activity of hydrophobic and hydrophilic soot particles. *Physical Chemistry Chemical Physics*, 11(36):7906–7920, 2009.
- [65] S Komura, Y Hirose, and Y Nonomura. Adsorption of colloidal particles to curved interfaces. *The Journal of Chemical Physics*, 124(24):241104, 2006.

- [66] A. Korolev. Limitations of the Wegener-Bergeron-Findeisen mechanism in the evolution of mixed-phase clouds. *Journal of the Atmospheric Sciences*, 64(9):3372–3375, September 2007.
- [67] A. Korolev and G. A. Isaac. Shattering during sampling by OAPs and HVPS. Part I: Snow particles. *Journal of Atmospheric and Oceanic Technology*, 22(5):528–542, May 2005.
- [68] A. V. Korolev, G. A. Isaac, and J. Hallett. Ice particle habits in Arctic clouds. *Geophysical Research Letters*, 26(9):1299–1302, 1999.
- [69] Linhong Kou, Daniel Labrie, and Petr Chylek. Refractive Indices of Water and Ice in the 0.65- to 2.5- μm Spectral Range. *Applied Optics*, 32(19):3531–3540, 1993.
- [70] Ari Laaksonen, Pekka Korhonen, Markku Kulmala, and Robert J. Charlson. Modification of the Köhler Equation to Include Soluble Trace Gases and Slightly Soluble Substances. *Journal of the Atmospheric Sciences*, 55(5):853–862, March 1998.
- [71] L. A. Ladino, O. Stetzer, and U. Lohmann. Contact freezing: a review. *Atmos. Chem. Phys. Discuss.*, 13(3):7811–7869, 2013.
- [72] J. S. Langer and H. Mullerkrumbhaar. Stability Effects in Dendritic Crystal-Growth. *Journal of Crystal Growth*, 42(Dec):11–14, 1977.
- [73] J. S. Langer, R. F. Sekerka, and T. Fujioka. Evidence for a universal law of dendritic growth rates. *Journal of Crystal Growth*, 44(4):414–418, 1978.
- [74] Irving Langmuir. THE PRODUCTION OF RAIN BY A CHAIN REACTION IN CUMULUS CLOUDS AT TEMPERATURES ABOVE FREEZING. *Journal of Meteorology*, 5(5):175–192, October 1948.
- [75] Christophe Lécuyer. *Water on Earth*. Wiley-ISTE, 2013.
- [76] Zev Levin, Noam Halfon, and Pinhas Alpert. Reassessment of rain enhancement experiments and operations in Israel including synoptic considerations. *Atmospheric Research*, 97(4):513–525, 2010.
- [77] Zev Levin and Saul A. Yankofsky. Contact Versus Immersion Freezing of Freely Suspended Droplets by Bacterial Ice Nuclei. *Journal of Climate and Applied Meteorology*, 22(11):1964–1966, November 1983.

- [78] Henri Lhuissier and Emmanuel Villermaux. Bursting bubble aerosols. *Journal of Fluid Mechanics*, 696:5–44, 2012.
- [79] D.R. Lide and Chemical Rubber Company. *CRC Handbook of Chemistry and Physics*. CRC Press, 1998.
- [80] Gérard Liger-Belair, Clara Cilindre, Régis D Gougeon, Marianna Lucio, Istvan Gebefügi, Philippe Jeandet, and Philippe Schmitt-Kopplin. Unraveling different chemical fingerprints between a champagne wine and its aerosols. *Proceedings of the National Academy of Sciences*, 106(39):16545–16549, 2009.
- [81] ER Likhachev. Dependence of water viscosity on temperature and pressure. *Technical Physics*, 48(4):514–515, 2003.
- [82] E. Loomis. On the Freezing-points of Dilute Solutions. I. *Physical Review (Series I)*, 1(3):199–213, 1893.
- [83] Y. J. Lu, W. J. Xie, and B. B. Wei. Rapid growth of ice dendrite in acoustically levitated and highly undercooled water. *Chinese Physics Letters*, 19(10):1543–1546, October 2002.
- [84] W. C. Macklin and B. F. Ryan. Habits of Ice Grown in Supercooled Water and Aqueous Solutions. *Philosophical Magazine*, 14(130):847–&, 1966.
- [85] C. Marcolli, S. Gedamke, T. Peter, and B. Zobrist. Efficiency of immersion mode ice nucleation on surrogates of mineral dust. *Atmos. Chem. Phys.*, 7(19):5081–5091, 2007.
- [86] BJ Mason and J Maybank. The fragmentation and electrification of freezing water drops. *Quarterly Journal of the Royal Meteorological Society*, 86(368):176–185, 1960.
- [87] John P McCloskey and Jens OM Karlsson. Temporally resolved imaging of ice nucleation and growth in highly supercooled water. pages 195–196. IEEE, 2012.
- [88] O. Möhler, P. R. Field, P. Connolly, S. Benz, H. Saathoff, M. Schnaiter, R. Wagner, R. Cotton, M. Krämer, A. Mangold, and A. J. Heymsfield. Efficiency of the deposition mode ice nucleation on mineral dust particles. *Atmos. Chem. Phys.*, 6(10):3007–3021, 2006.

- [89] O. Möhler, O. Stetzer, S. Schaefer, C. Linke, M. Schnaiter, R. Tiede, H. Saathoff, M. Krämer, A. Mangold, P. Budz, P. Zink, J. Schreiner, K. Mauersberger, W. Haag, B. Kärcher, and U. Schurath. Experimental investigation of homogeneous freezing of sulphuric acid particles in the aerosol chamber AIDA. *Atmos. Chem. Phys.*, 3(1):211–223, 2003.
- [90] S. C. Mossop. Production of Secondary Ice Particles during Growth of Graupel by Riming. *Quarterly Journal of the Royal Meteorological Society*, 102(431):45–57, 1976.
- [91] S. C. Mossop. The Mechanism of Ice Splinter Production during Riming. *Geophysical Research Letters*, 7(2):167–169, 1980.
- [92] S. C. Mossop. Microphysical Properties of Supercooled Cumulus Clouds in Which an Ice Particle Multiplication Process Operated. *Quarterly Journal of the Royal Meteorological Society*, 111(467):183–198, 1985.
- [93] S. C. Mossop, A. Ono, and E. R. Wishart. Ice Particles in Maritime Clouds near Tasmania. *Quarterly Journal of the Royal Meteorological Society*, 96(409):487–&, 1970.
- [94] D. M. Murphy and T. Koop. Review of the vapour pressures of ice and supercooled water for atmospheric applications. *Quarterly Journal of the Royal Meteorological Society*, 131(608):1539–1565, 2005.
- [95] B. J. Murray, D. O’Sullivan, J. D. Atkinson, and M. E. Webb. Ice nucleation by particles immersed in supercooled cloud droplets. *Chemical Society Reviews*, 41(19):6519–6554, 2012.
- [96] Kai-Uwe Nerding. *Statistik und Dynamik der Fragmentation von Wolkentröpfchen - Statistics and dynamics of cloud droplet fragmentation*. Bachelor thesis, Karlsruher Institut für Technologie (KIT), Karlsruhe, October 2011.
- [97] Monika Niemand, Ottmar Möhler, Bernhard Vogel, Heike Vogel, Corinna Hoose, Paul Connolly, Holger Klein, Heinz Bingemer, Paul DeMott, Julian Skrotzki, and Thomas Leisner. A Particle-Surface-Area-Based Parameterization of Immersion Freezing on Desert Dust Particles. *Journal of the Atmospheric Sciences*, 69(10):3077–3092, October 2012.

- [98] Odencran.Fk, W. S. Mcewan, P. Stamand, and W. G. Finnegan. Mechanism for Multiplication of Atmospheric Ice Crystals - Apparent Charge Distribution on Laboratory Crystals. *Science*, 160(3834):1345–&, 1968.
- [99] C. D. O’Dowd and G. De Leeuw. Marine aerosol production: a review of the current knowledge. *Philosophical Transactions of the Royal Society a-Mathematical Physical and Engineering Sciences*, 365(1856):1753–1774, July 2007.
- [100] M. Oettel and S. Dietrich. Colloidal Interactions at Fluid Interfaces . *Langmuir*, 24(4):1425–1441, February 2008.
- [101] K. Ohsaka and E. H. Trinh. Apparatus for measuring the growth velocity of dendritic ice in undercooled water. *Journal of Crystal Growth*, 194(1):138–142, November 1998.
- [102] V.I. Osipov. Density of clay minerals. *Soil Mechanics and Foundation Engineering*, 48(6):231–240, January 2012.
- [103] Thomas Jan Pander. Gefrierverhalten unterkühlter Wolkentropfen. Diploma thesis, Ruprecht-Karls-Universität Heidelberg, 2011.
- [104] W. Paul and M. Raether. Das Elektrische Massenfilter. *Zeitschrift Fur Physik*, 140(3):262–273, 1955.
- [105] Stéphan Pouleur, Claude Richard, Jean-Guy Martin, and Hani Antoun. Ice Nucleation Activity in *Fusarium acuminatum* and *Fusarium avenaceum*. *Applied and Environmental Microbiology*, 58(9):2960–2964, September 1992.
- [106] A. J. Prenni, P. J. DeMott, C. Twohy, M. R. Poellot, S. M. Kreidenweis, D. C. Rogers, S. D. Brooks, M. S. Richardson, and A. J. Heymsfield. Examinations of ice formation processes in Florida cumuli using ice nuclei measurements of anvil ice crystal particle residues. *Journal of Geophysical Research-Atmospheres*, 112(D10), May 2007.
- [107] A. J. Prenni, M. D. Petters, S. M. Kreidenweis, C. L. Heald, S. T. Martin, P. Artaxo, R. M. Garland, A. G. Wollny, and U. Poschl. Relative roles of biogenic emissions and Saharan dust as ice nuclei in the Amazon basin. *Nature Geoscience*, 2(6):401–404, June 2009.
- [108] H. R. Pruppacher. A New Look at Homogeneous Ice Nucleation in Supercooled Water Drops. *Journal of the Atmospheric Sciences*, 52(11):1924–1933, June 1995.

- [109] H. R. Pruppacher and R. J. Schlamp. A wind tunnel investigation on ice multiplication by freezing of waterdrops falling at terminal velocity in air. *Journal of Geophysical Research*, 80(3):380–386, January 1975.
- [110] Hans R. Pruppacher, James D. Klett, and Pao K. Wang. Microphysics of Clouds and Precipitation. *Aerosol Science and Technology*, 28(4):381–382, January 1998.
- [111] Pruppacher, H. R. Interpretation of Experimentally Determined Growth Rates of Ice Crystals in Supercooled Water. *Journal of Chemical Physics*, 47(5):1807–8, 1967.
- [112] B. G. Pummer, L. Atanasova, H. Bauer, J. Bernardi, I. S. Druzhinina, J. Fröhlich-Nowoisky, and H. Grothe. Spores of many common airborne fungi reveal no ice nucleation activity in oil immersion freezing experiments. *Biogeosciences*, 10(12):8083–8091, 2013.
- [113] B. G. Pummer, H. Bauer, J. Bernardi, S. Bleicher, and H. Grothe. Suspendable macromolecules are responsible for ice nucleation activity of birch and conifer pollen. *Atmos. Chem. Phys.*, 12(5):2541–2550, 2012.
- [114] Arthur L. Rangno. Fragmentation of Freezing Drops in Shallow Maritime Frontal Clouds. *Journal of the Atmospheric Sciences*, 65(4):1455–1466, April 2008.
- [115] Arthur L. Rangno and Peter V. Hobbs. Ice particles in stratiform clouds in the Arctic and possible mechanisms for the production of high ice concentrations. *Journal of Geophysical Research: Atmospheres*, 106(D14):15065–15075, 2001.
- [116] FM Raoult. General law of the vapor pressure of solvents. *Comptes Rendus*, 104:1430–3, 1887.
- [117] P. Roberts and J. Hallett. A laboratory study of the ice nucleating properties of some mineral particulates. *Quarterly Journal of the Royal Meteorological Society*, 94(399):25–34, 1968.
- [118] W Roedel and T Wagner. Physik unserer Umwelt: Die Atmosphäre. SpringerLink: Bücher. 2011.
- [119] Daniel Rzesanke. *Laborexperimente zum Einfluss elektrischer Ladungen auf Wolkenprozesse*. PhD thesis, Technische Universität Ilmenau, 2012.
- [120] Abdus Salam, Ulrike Lohmann, Brian Crenna, Glen Lesins, Peter Klages, David Rogers, Rishad Irani, Andrew MacGillivray, and Matthew Coffin. Ice Nucleation

- Studies of Mineral Dust Particles with a New Continuous Flow Diffusion Chamber. *Aerosol Science and Technology*, 40(2):134–143, February 2006.
- [121] C. P. R. Saunders and A. S. Hosseini. A laboratory study of the effect of velocity on Hallett-Mossop ice crystal multiplication. *Atmospheric Research*, 59-60(0):3–14, 2001.
- [122] Vincent J. Schaefer. The Production of Ice Crystals in a Cloud of Supercooled Water Droplets. *Science*, 104(2707):457–459, November 1946.
- [123] Jianying Shang, Markus Flury, James B Harsh, and Richard L Zollars. Comparison of different methods to measure contact angles of soil colloids. *Journal of Colloid and Interface Science*, 328(2):299–307, 2008.
- [124] A. A. Shibkov, Y. I. Golovin, M. A. Zheltov, A. A. Korolev, and A. A. Leonov. Morphology diagram of nonequilibrium patterns of ice crystals growing in supercooled water. *Physica a-Statistical Mechanics and Its Applications*, 319:65–79, March 2003.
- [125] A. A. Shibkov, Y. I. Golovin, M. A. Zheltov, A. A. Korolev, and A. A. Vlasov. Kinetics and morphology of nonequilibrium growth of ice in supercooled water. *Crystallography Reports*, 46(3):496–502, May 2001.
- [126] A. A. Shibkov, M. A. Zheltov, A. A. Korolev, A. A. Kazakov, and A. A. Leonov. Effect of surface kinetics on the dendritic growth of ice in supercooled water. *Crystallography Reports*, 49(6):1056–1063, November 2004.
- [127] AA Shibkov, MA Zheltov, AA Korolev, AA Kazakov, and AA Leonov. Crossover from diffusion-limited to kinetics-limited growth of ice crystals. *Journal of Crystal Growth*, 285(1):215–227, 2005.
- [128] W. Shimada and Y. Furukawa. Pattern formation of ice crystals during free growth in supercooled water. *Journal of Physical Chemistry B*, 101(32):6171–6173, August 1997.
- [129] Pyungho Shin, Jaeyong Sung, and Myeong Ho Lee. Control of droplet formation for low viscosity fluid by double waveforms applied to a piezoelectric inkjet nozzle. *Microelectronics Reliability*, 51(4):797–804, 2011.
- [130] Glen A. Slack. Thermal conductivity of ice. *Physical Review B*, 22(6):3065–3071, 1980.

- [131] Donald E Spiel. On the births of film drops from bubbles bursting on seawater surfaces. *Journal of Geophysical Research: Oceans (1978-2012)*, 103(C11):24907–24918, 1998.
- [132] P. Squires and E. J. Smith. The Artificial Stimulation of Precipitation by Means of Dry Ice. *Australian Journal of Chemistry*, 2(2):232–245, 1949.
- [133] I. Steinke, O. Möhler, A. Kiselev, M. Niemand, H. Saathoff, M. Schnaiter, J. Skrotzki, C. Hoose, and T. Leisner. Ice nucleation properties of fine ash particles from the Eyjafjallajökull eruption in April 2010. *Atmos. Chem. Phys.*, 11(24):12945–12958, 2011.
- [134] C. Takahashi and A. Yamashita. Production of Ice Splinters by the Freezing of Water Drops in Free Fall. *Journal of the Meteorological Society of Japan. Ser. II*, 55(1):139–141, 1977.
- [135] Chuji Takahashi. Relation between the Deformation and the Crystalline Nature of Frozen Water Drops. *Journal of the Meteorological Society of Japan. Ser. II*, 54(6):448–453, 1976.
- [136] Chuji Takahashi and A. Yamashita. Shattering of frozen water drops in a supercooled cloud. *Journal of the Meteorological Society of Japan*, 1970.
- [137] Geoffrey Taylor. *The Dynamics of Thin Sheets of Fluid. III. Disintegration of Fluid Sheets*, volume 253. December 1959.
- [138] William Thomson. LX. On the equilibrium of vapour at a curved surface of liquid. *The London, Edinburgh, and Dublin Philosophical Magazine and Journal of Science*, 42(282):448–452, 1871.
- [139] E. Tombari, C. Ferrari, and G. Salvetti. Heat capacity anomaly in a large sample of supercooled water. *Chemical Physics Letters*, 300(5-6):749–751, February 1999.
- [140] TSI. Model 3080-Series Electrostatic Classifiers. Product information, 2001.
- [141] TSI. Model 3076 Constant Output Atomizer. Manual, 2005.
- [142] TSI. FLUIDIZED BED AEROSOL GENERATOR MODEL 3400a. Product information, 2014.
- [143] TSI. ULTRAFINE CONDENSATION PARTICLE COUNTER MODEL 3776. Product information, 2014.

- [144] Hiroshi Tsuji, Hiroko Satoh, Shigeki Ikeda, Yasuhito Gotoh, and Junzo Ishikawa. Contact angle lowering of polystyrene surface by silver-negative-ion implantation for improving biocompatibility and introduced atomic bond evaluation by XPS. *Nuclear Instruments and Methods in Physics Research Section B: Beam Interactions with Materials and Atoms*, 141(1-4):197–201, 1998.
- [145] S. Twomey. Pollution and the planetary albedo. *Atmospheric Environment (1967)*, 8(12):1251–1256, 1974.
- [146] S. Twomey. Influence of Pollution on Shortwave Albedo of Clouds. *Journal of the Atmospheric Sciences*, 34(7):1149–1152, 1977.
- [147] S. A. Twomey, M. Piepgrass, and T. L. Wolfe. An assessment of the impact of pollution on global cloud albedo. *Tellus Series B-Chemical and Physical Meteorology*, 36B(5):356–366, 1984.
- [148] Larry Vardiman. The Generation of Secondary Ice Particles in Clouds by Crystal-Crystal Collision. *Journal of the Atmospheric Sciences*, 35(11):2168–2180, November 1978.
- [149] N. B. Vargaftik, B. N. Volkov, and L. D. Voljak. International Tables of the Surface Tension of Water. *Journal of Physical and Chemical Reference Data*, 12(3):817–820, 1983.
- [150] G. Vidaurre and J. Hallett. Particle Impact and Breakup in Aircraft Measurement. *Journal of Atmospheric and Oceanic Technology*, 26(5):972–983, May 2009.
- [151] Emmanuel Villermaux and Benjamin Bossa. Single-drop fragmentation determines size distribution of raindrops. *Nature Physics*, 5(9):697–702, 2009.
- [152] Annele Virtanen, Jorma Joutsensaari, Thomas Koop, Jonna Kannosto, Pasi Yli-Pirila, Jani Leskinen, Jyrki M. Makela, Jarmo K. Holopainen, Ulrich Poschl, Markku Kulmala, Douglas R. Worsnop, and Ari Laaksonen. An amorphous solid state of biogenic secondary organic aerosol particles. *Nature*, 467(7317):824–827, 2010.
- [153] B. Vonnegut. The Nucleation of Ice Formation by Silver Iodide. *Journal of Applied Physics*, 18(7):593–595, 1947.
- [154] Alfred Wegener. *Thermodynamik der Atmosphäre*. JA Barth, 1911.

-
- [155] Christiane Wender. *Eiskristallwachstum aus der Gasphase auf elektrodynamisch levitierten Einzelpartikeln*. PhD thesis, Ruprecht-Karls-Universität Heidelberg, 2012.
- [156] Heike Wex, Frank Stratmann, David Topping, and Gordon McFiggans. The Kelvin versus the Raoult Term in the Köhler Equation. *Journal of the Atmospheric Sciences*, 65(12):4004–4016, December 2008.
- [157] Herman Wijshoff. The dynamics of the piezo inkjet printhead operation. *Physics Reports*, 491(4-5):77–177, 2010.
- [158] P K Wolber, C A Deininger, M W Southworth, J Vandekerckhove, M van Montagu, and G J Warren. Identification and purification of a bacterial ice-nucleation protein. *Proceedings of the National Academy of Sciences*, 83(19):7256–7260, October 1986.
- [159] Frank Zimmermann, Stephan Weinbruch, Lothar Schütz, Heiko Hofmann, Martin Ebert, Konrad Kandler, and Annette Worringer. Ice nucleation properties of the most abundant mineral dust phases. *Journal of Geophysical Research: Atmospheres*, 113(D23):D23204, 2008.

Acknowledgements

I'd like to thank professor Thomas Leisner for giving me the opportunity to write this thesis. Working under his guidance has been a great experience, as he unites a phenomenal understanding of physics, a fine instinct for experimental work problems and solutions and a quick mind with care for his PhD students. He gave me the freedom to play with amazing pieces of equipment in the direction I saw fit and was always interested in the developments of my work.

I'd like to thank all my colleagues at the IMK-AAF for all the good years. I appreciated the good atmosphere at the institute, knowing that one cannot take the feeling of a community at the workplace for granted. I'd specifically like to thank my colleagues at the Paul trap laboratory, it has been a pleasure to work alongside them and to exchange ideas and sometimes idle banter.

I'd like to thank Daniel Rzesanke, who convinced me to do my diploma thesis at the KIT, for his creative energy at all times and for showing me that critically reading papers is a scientist's duty. I'd like to thank Christiane Wender for showing me the ropes at the beginning, for letting me know what experimental work means and for the secret to good pizza baking. I'd like to thank Alexei Kiselev for being the best laboratory superintendent I ever had and could wish for, both with regard to his knowledge on experimental work and his ability to become an expert in new fields of atmospheric research and to share that knowledge. I'd like to thank Jens Nadolny for his invaluable tech support in everything around the electrodynamic balance, the good times at the game evenings and, of course, for Bud Spencer and Terence Hill movies. I'd like to thank Kai-Uwe Nerding for the time, energy and interest he invested into the work at the Paul trap laboratory. I'd like to thank Patricia Handmann for the great work we could do together, for the parties and for the horse stories. I'd like to thank Andreas Peckhaus for sharing the office with me, for the dry humor and the excursions into philosophical playgrounds. I'd like to thank Denis Duft for always having an open ear in matters of science and not-exactly-science. I'd like to thank Nadine for being a nice and open co-laboratorist and for lending a helping hand in times of experimental difficulties.

I'd like to thank Harald Saathoff and Ottmar Möhler for their advice over the years, I'd like to thank Schorsch Scheurig for his technical help in situations of need and for his humor, I'd like to thank Betty Kranz for listening and for her wisdom, I'd like to thank Frank Schwarz for the fresh air breaks we took together and I'd like to thank Susanne Bolz for being a great organisator and helping me in many situations.

I'd like to thank my brother for supporting me in the last days of my thesis. Thank you, Martin! I'd like to thank my parents, Susanne and Christoph, and my grandparents, Margarete and Heinz Schittko. Without you, I would neither be there, nor would I be where I am today. Thank you for always believing in me and supporting me!

And I thank you, Julia, my love, for the incredible support you are to me by being you.

Eidesstattliche Versicherung gemäß § 8 der Promotionsordnung für die Naturwissenschaftlich - Mathematische Gesamtfakultät der Universität Heidelberg / Sworn Affidavit according to § 8 of the doctoral degree regulations of the Combined Faculty of Natural Sciences and Mathematics

1. Bei der eingereichten Dissertation zu dem Thema / The thesis I have submitted entitled 'Laboratory ice multiplication experiments on single levitated microdroplets' handelt es sich um meine eigenständig erbrachte Leistung / is my own work.

2. Ich habe nur die angegebenen Quellen und Hilfsmittel benutzt und mich keiner unzulässigen Hilfe Dritter bedient. Insbesondere habe ich wörtlich oder sinngemäß aus anderen Werken übernommene Inhalte als solche kenntlich gemacht. / I have only used the sources indicated and have not made unauthorised use of services of a third party. Where the work of others has been quoted or reproduced, the source is always given. 3.

Die Arbeit oder Teile davon habe ich bislang nicht an einer Hochschule des In- oder Auslands als Bestandteil einer Prüfungs- oder Qualifikationsleistung vorgelegt. / I have not yet presented this thesis or parts thereof to a university as part of an examination or degree.

4. Die Richtigkeit der vorstehenden Erklärungen bestätige ich. / I confirm that the declarations made above are correct.

5. Die Bedeutung der eidesstattlichen Versicherung und die strafrechtlichen Folgen einer unrichtigen oder unvollständigen eidesstattlichen Versicherung sind mir bekannt. / I am aware of the importance of a sworn affidavit and the criminal prosecution in case of a false or incomplete affidavit Ich versichere an Eides statt, dass ich nach bestem Wissen die reine Wahrheit erkläre und nichts verschwiegen habe. / I affirm that the above is the absolute truth to the best of my knowledge and that I have not concealed anything.

(Ort, Datum/Place, date)

(Thomas Jan Pander)